BEARING WORLD

www.bearingworld.org

Journal

Volume 4_2019

Editors: G. Poll _ A. Grunau _ C. Kunze

Published by
FVA sharing drive innovation
VDMA Verlag

Imprint

Bearing World Journal
Volume 4, December 2019

Published by:
Forschungsvereinigung Antriebstechnik e.V. (FVA)
Lyoner Straße 18
60528 Frankfurt am Main
Germany
www.fva-net.de

Print-ISSN 2513-1753

Volume 4_2019

Dear reader,

Globalization increasingly requires more and more international networking between research and development engineers. In response to this, the German Research Association for Drive Technology (FVA) launched the first Bearing World conference in 2016. With that inaugural meeting, the FVA initiated a very fruitful international dialogue in which researchers and developers from universities and bearing manufacturers came together with users and experts from the industry. The Bearing World conference is held every two years; more than 280 experts from 18 countries met at the last Bearing World conference in 2018 in Kaiserslautern, Germany, to share the latest research findings in the world of bearings. The next meeting will take place in Hannover, Germany, on March 31 and April 1, 2020.

The Bearing World Journal, which is published annually, serves to foster exchange between international experts during non-conference years by featuring peer-reviewed, high-quality scientific papers on rolling element bearings as well as plain bearings. As an international expert platform for publishing cutting-edge research findings, the journal intends to contribute to technological progress in the field of bearings.

We are now starting to prepare the 2020 edition of Bearing World Journal and are looking forward to new contributions from the scientific and industrial communities. We would like to thank all authors for their fascinating contributions to Bearing World Journal No. 4.

_ **Prof. Dr.-Ing. Gerhard Poll,** Initiator, Head of international Scientific Board
_ **Dr.-Ing. Arbogast Grunau,** President of the FVA Management Board
_ **Christian Kunze,** Editor-in-chief

Please send the paper you intend to publish in the next issue of the Bearing World Journal via e-mail as Word document to FVA (**submission@bearingworld.org**). In addition please attach a PDF document.

Bearing World Scientific Board

Contents

Conductive Simmerrings help prevent electrical discharge machining in modern electrical powertrains

Thomas Klenk[1], Francois Colineau[2], Stefan Morgenstern[3]

[1] *Division Oil Seals Powertrain and Driveline, Freudenberg Sealing Technologies, thomas.klenk@fst.com*
[2] *Division Oil Seals Powertrain and Driveline, Freudenberg Sealing Technologies, francois.colineau@fst.com*
[3]*Technology & Innovation, Freudenberg Sealing Technologies, stefan.morgenstern@fst.com*

Abstract:

Electric motors used in e-mobility place completely new requirements on the radial shaft seals, Simmerrings, used in these applications. In the past, research and development work has focused on reducing friction in combustion engines and driveline systems in combination with increasingly higher performance lubricants. With electric motors and the downstream transmission, however, extremely high speeds in conjunction with a short-circuit function for bearing currents are crucial points.

The shafts with which an electric drive performs its work are electrically isolated from the housing in many operating conditions. The insulation is created by the lubricating films in the contact zones of the bearings and shaft seals, which are necessary in order for these components to function permanently [1]. Alternating currents and their electromagnetic fields change the electrical potential between the rotor and the stator and the rotor charges up. The currents can only be grounded by using the earthed housing. Grounding can only take place if the currents can pass from the shaft to the housing via an electrical connection. Such an electrical connection can be established with the help of conductive nonwovens developed by Freudenberg Sealing Technologies, which can also be applied to seals to save space. The impedance of such grounding elements can be tested for the first time in a wide range of operating conditions by using a specially developed test setup. For example, impedance of approx. 50 ohms within a frequency range of between 5 kHz and 1 MHz was measured on a nonwoven on a 32 mm shaft at 80 °C, at a speed of 15,000 rpm and with a service life of 240 hours.

Conductive nonwovens are already being mass produced today. They effectively prevent bearing damage, also thanks to their additional dirt-repellent function against dust, abrasive particles and dirty water. The products are also continuously being further developed to meet future requirements, such as shielding against electromagnetic interference (EMI).

Keywords:

EDM electrical discharge machining, conductive nonwovens, bearing damage, impedance spectroscopy, EMI electromagnetic interference

1. Introduction

The electric motors used in e-mobility place completely new requirements on the Simmerrings used in these applications.

In the past, research and development work on combustion engines has been on reducing friction in combination with increasingly higher performance lubricants. But electric motors and the downstream transmissions must cope with extremely high speeds in conjunction with a short-circuit function for bearing currents.

The shafts with which an electric drive carries out its function are electrically isolated from the housing in many operating conditions. The insulation is created by the lubricating films in the contact zones of the bearings and shaft seals that are vital to these components functioning permanently [1]. Alternating currents and their electromagnetic fields change the electrical potential between the rotor and the stator – the rotor charges. The currents can only be grounded by using the earthed housing. The discharge via grounding can only take place if the currents can pass from the shaft to the housing via an electrical connection. If no such connection has been made, the current for the transition will seek the point with the lowest resistance: the bearing. This results in an abrupt local discharge in which current is transferred from the inner ring of the bearing to the outer ring via the rolling elements and thus flows through the bearing.

Figure 1: Different degrees of bearing damages [2, 3, 4]

During the current transfer with a high current density between the rolling elements and the bearing rings, discharge flashes occur, which lead to a martensitic microstructure change in the bearing materials used, for example, and are often also made visible by a striped surface pattern, Figure 1.

These structural changes in conjunction with the existing mechanical bearing load cause such massive and permanent damage to the bearing surfaces that acoustic abnormalities can often occur. In fact, fatigue fractures can then even result in total failure of the bearing later on due to material fatigue and material eruptions on the surface [2, 3, 4].

In principle, bearing damage can be divided into five degrees with degrees 1 to 4 being surface damage and degree 0 corresponding to the original surface that would still allow normal operation.

This type of electrical damage can definitely be prevented: A permanent electrical contact between the shaft and the housing is the only thing that must be ensured. Then the electrical charge will flow continuously and neither a high electrical potential between the shaft and the housing nor an abrupt discharge via the bearings will occur. Solutions that have impedances of around 10 to 100 Ω in a wide frequency range (to reduce EDM – electrical discharge machining) have gained great acceptance. If the impedance across all operating states is even lower than 10 Ω, the solution is assumed to be able to improve EMI (electromagnetic interference) issues as well.

The combination of a shaft grounding element with Simmerrings, which are already used to seal the bearing lubricants, is a particularly ideal solution to this problem as this leads to a significant reduction in installation space. The challenge is to find current transmitters that are in permanent contact with both the housing and the shaft. Seals usually consist of electrically insulating materials and are not suited to perform this task.

2. Problem solving based on conductive nonwovens

Freudenberg Sealing Technologies (FST) has been mass producing a so-called electrically conductive nonwoven disc for several years now. The advantage is that it is firmly connected to the shaft sealing ring and requires virtually no additional installation space, Figure 2. Here, the conductivity of the nonwoven is achieved by special fibers embedded in a matrix. The system has been mass produced for electric vehicles for years and reliably prevents bearing damages. The electrical impedance of this solution is already at a very low level.

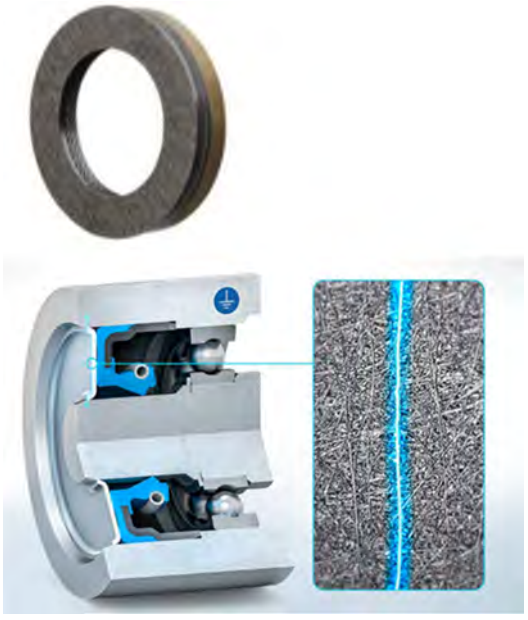

Figure 2: A Simmerring integrated conductive nonwoven disc

FST's development expertise has been focused on the further development of this solution in recent years. Here, both the composition of the basic nonwoven and the product design have been improved to optimize the grounding function and the service life of the product under the most demanding conditions (speeds, dynamic and thermal loads, minimized friction and wear) [5]. The result is a new generation of grounding products with improved mechanical properties (elasticity, relaxation), resulting in much more constant grounding performance over time and an equivalent lifetime as a radial shaft seal.

The nonwoven grounding solution can be used both as a stand-alone solution and as an integrated function of various FST sealing concepts, e.g. LFS (Low Friction Simmerrings), B2LV (conductive nonwoven flanged in a metal housing) and the gas lubricated mechanical face seal Levitex for passenger car applications or BAUM radial shaft seals for industrially used electric motors and gears, Figure 3.

With regard to the design shown in Figure 3, it is important that the nonwoven lip offer continuous, uniform electrical resistance and is not only coated on the surface. As shown, this allows for mounting in all directions and results in independence of wear.

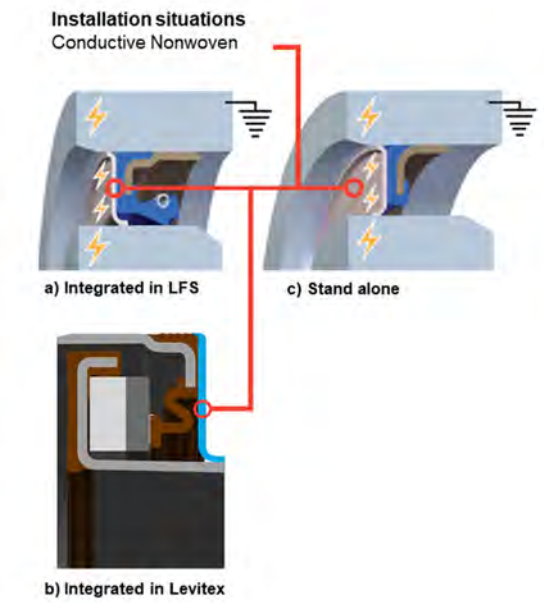

Figure 3: Electrically conductive nonwoven disc integrated into the a) LFS and b) Levitex function or as c) a "stand-alone solution."

Benefits	Simmerring® with electrically conductive nonwoven	Carbon brushes	Fiber bundles
Costs	+	-	-
Space-saving in the unit	++	--	-
Service life	+	-	-
Conductivity in dynamic operation	+	++	-
Contamination due to abrasion of the component and the oppsing surface	++	-	-
Friction	++	-	+

Figure 4: Benchmark of different EDM concepts with regard to key application parameters

Figure 4 shows a comparison of the new nonwoven-based solution for reducing EDM with previous concepts based on carbon brushes or fiber bundles.

Regarding the space-saving in the unit, the Simmerring with electically conductive nonwoven is based on a glueing solution which connects the thin conductive element with an already in place seal (additional space smaller than 1 mm). This function integration leads to cost reduction at the customer. For carbon brushes or a fiber bundle, the solutions require more space due to their stand alone design. For conductivity in dynamic operation and service life, a sufficient contact force over is required. On the carbon brush, this is realized by a metal spring, for the conductive nonwoven it is a rubber spring and the fiber bundle shows no additional spring element. Regarding the carbon brush, the spring force is often at a high value which could lead to a wear effect with contamination issues and resulting maintance work. The balanced contact force of the conductive nonwoven allows a good dynamic conductivity, but also offers low friction behavior and a long service life comparable to sealing function.

Other ways of preventing bearing currents include conductive lubricants, for example. Typical greases for electric motors consist of an oil (mineral, synthetic, esterified), a soap and an additive package. Typically, in conductive greases, the additive package consists of a)

conductive particles (e.g. graphite) or b) a conductive liquid and c) a high polarity of the oil. In all three cases, the voltage between the shaft and the housing is minimized by greatly reduced resistance in the contact zones of the bearing. However, such liquids that contain solid particles such as graphite often do not work over extended periods of time. This depends on the particle size, the electrical conductivity and the interaction between the surface and the conductive particles. In addition, it should be noted that these heavily modified lubricants may be inadequately compatible with the elastomer materials of seals.

Another possibility is to insulate the shaft with ceramic hybrid bearings. The non-conductive ceramic reliably prevents EDM currents. Nevertheless, this defective process can still be transferred to other components connected to the motor shaft. For example, in the downstream transmission, EDM currents may flow between the gears and severely damage them even up to the point of failure.

Furthermore, electrical filters cannot reliably prevent EDM currents, therefore, according to the current state of the art, shaft grounding systems such as conductive nonwovens must be used.

3. Experimental investigation and testing

FST uses a specially developed test procedure [6] to test and validate the functions of the seal with a conductive nonwoven. This measuring method makes it possible to compare and evaluate grounding elements under realistic conditions for the first time. During product development, it became clear that a static measurement of the DC resistance could not be used to make a reliable statement about the function of the grounding element during dynamic operation. Therefore, the new measuring method to be developed was designed to test the grounding elements on radial shaft seal test rigs under the influence of alternating current frequency, speed, temperature and time.

The test benches used are shown schematically in Figure 5 below. They have test pots equipped with an air-bearing which is also suited for measuring friction torques as described below.

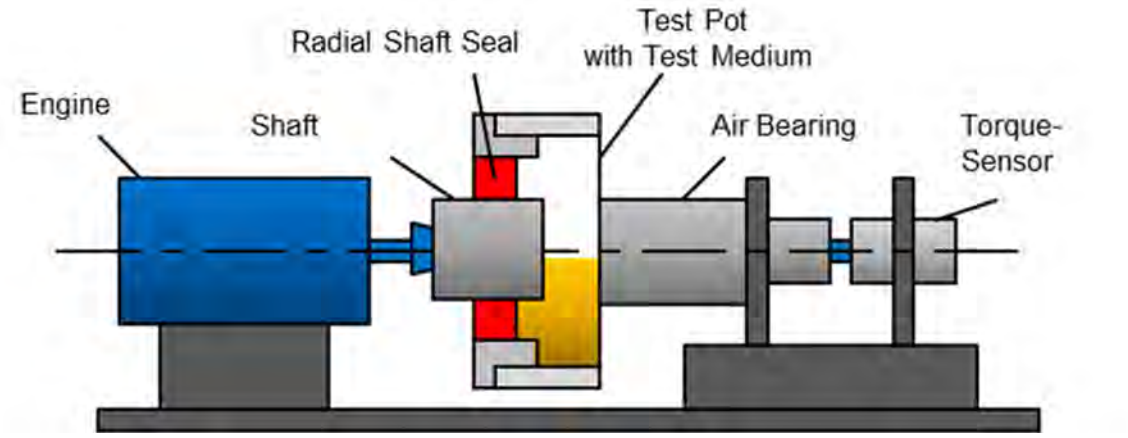

Figure 5: Schematic design of the radial shaft seal test benches

In order to measure all relevant frequency ranges for both bearing currents and EMI, the grounding elements are characterized by using impedance spectroscopy. The impedance is also called AC resistance, or frequency-dependent electrical resistance. This is due to the fact that electrical systems can contain both capacitors and inductors which change their resistance with varying frequency. The Impedance *z*, like DC resistance, is defined as the ratio of voltage to current *U/I*. The time component t, the angular frequency ω as well as the phase shift between current and voltage, defined as phase angle *φ*, are added.

$$z(t) = u(t)/i(t) \qquad \textit{(Eq. 1)}$$

$$u(t) = u_0 * sin(\omega t) \qquad \textit{(Eq. 2)}$$

$$i(t) = i_0 * \sin(\omega t + \varphi) \qquad \textit{(Eq. 3)}$$

results in the following impedance *z*

$$z = u_0 * sin(\omega t)/i_0 * \sin(\omega t + \varphi) \qquad \textit{(Eq. 4)}$$

$$z = z_0 * sin(\omega t)/\sin(\omega t + \varphi) \qquad \textit{(Eq. 5)}$$

3.1. Test setup for impedance measurement

A vector network analyzer (VNA) that is connected to the test bench setup is used as the measuring device. Two identical products are tested at once and connected in series, Figure 6, to rule out the influence of other contact elements that cannot be calibrated. Afterwards, the impedance measured has to be divided by two in order to obtain the value for one grounding element. This operation was already performed and yielded the following results.

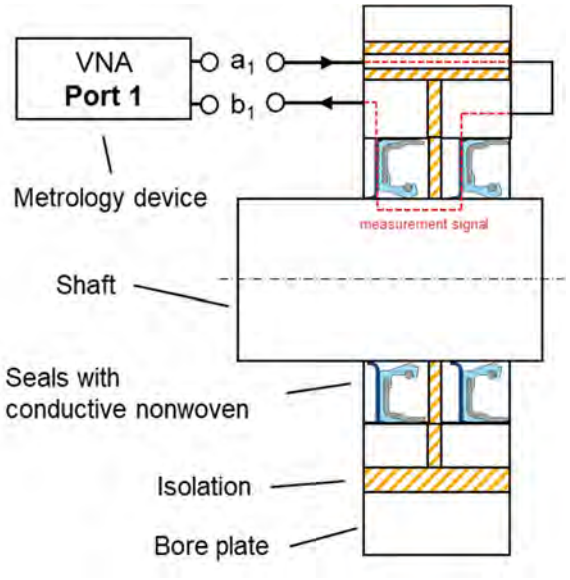

Figure 6: Schematic test bench setup for impedance spectroscopy

The bore plate can be mounted on the radial shaft seal test bench after the sealing rings have been assembled. The network analyzer is then connected to the measurement setup via a connection board. Figure 7 shows the setup on the test bench.

Figure 7: Test bench setup for impedance spectroscopy during dynamic operation

3.2. Results of impedance measurement

For the sake of clarity regarding the statement made above, that measuring the impedance, or even DV resistance, of transmission elements in a static state at 0 rpm makes no sense, Figure 8 contains measurements of two different grounding elements A and B in a Bode diagram that shows both the impedance and the phase angle across the frequency. Both elements are measured at 0 rpm and 1000 rpm. Although element A has a lower impedance in a static state than element B, the latter is much more conductive in dynamic operation (factor greater than 10).

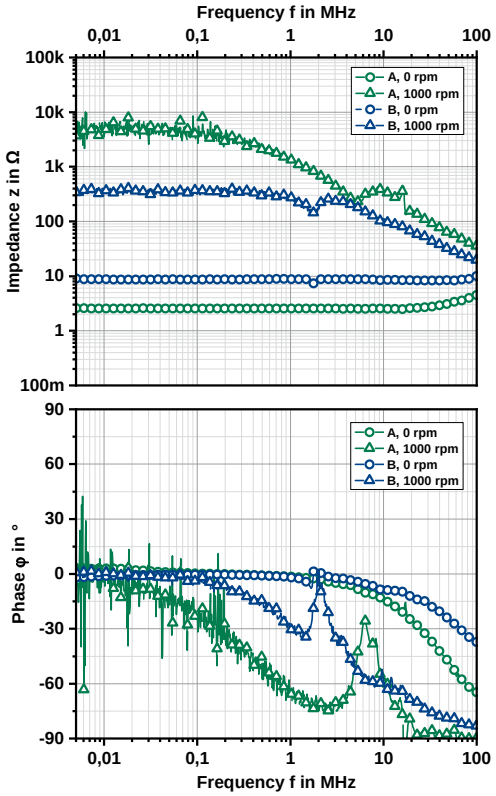

Figure 8: Impedance measurement of electrically conductive elements in a static state and dynamic operation

Measuring shaft grounding systems in a static state is therefore not a useful method for assessing their function in dynamic operation.

In order to characterize the grounding elements, they are tested using an endurance run program that includes impedance measurement at different temperature levels and a wide speed range every 24 hours.

The following measurement results are exemplary for the electrically conductive nonwoven at 120 °C. For this purpose, the impedance at different speeds before the endurance run is shown in the Bode diagram in Figure 9.

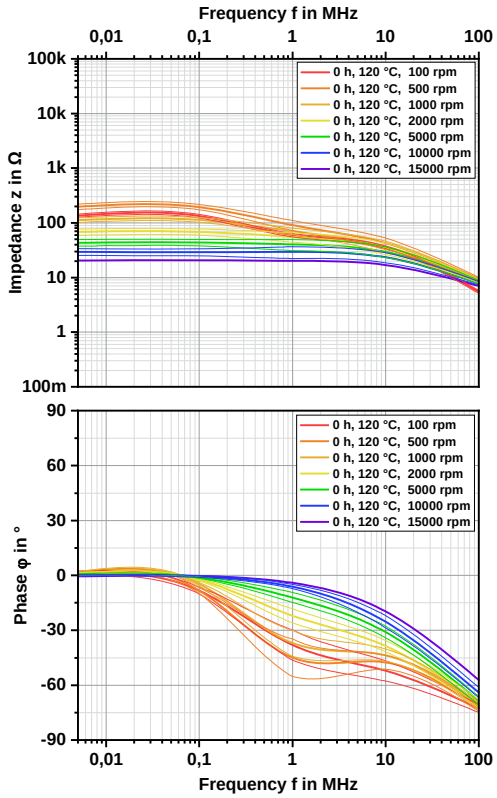

Figure 9: Impedance measurement of electrically conductive nonwoven, function-integrated on the LFS, shaft dimension 32 mm at 120 °C before the endurance run

We can see that the impedance decreases with increasing speed, from approx. 200 Ω at 100 rpm to approx. 30 Ω at 15,000 rpm. This is a reproducible behavior of conductive nonwovens. Figure 10 shows the mean value of the impedance between 5 and 6 kHz over the entire 240-hour test period, again at different speeds.

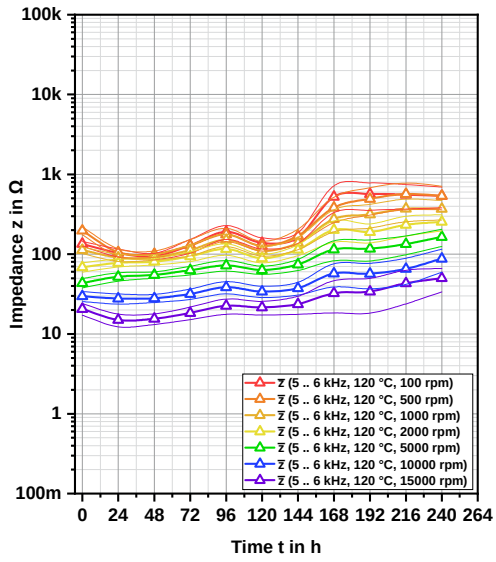

Figure 10: Impedance measurement of electrically conductive nonwoven, function-integrated on the LFS, shaft dimen-sion 32 mm at 120 °C with the average value of impedance over 240 h

We can see a slight increase in impedance over the continuous run. For a closer look, Figure 11 once again shows the Bode diagram with the measurement after the 240-hour endurance run.

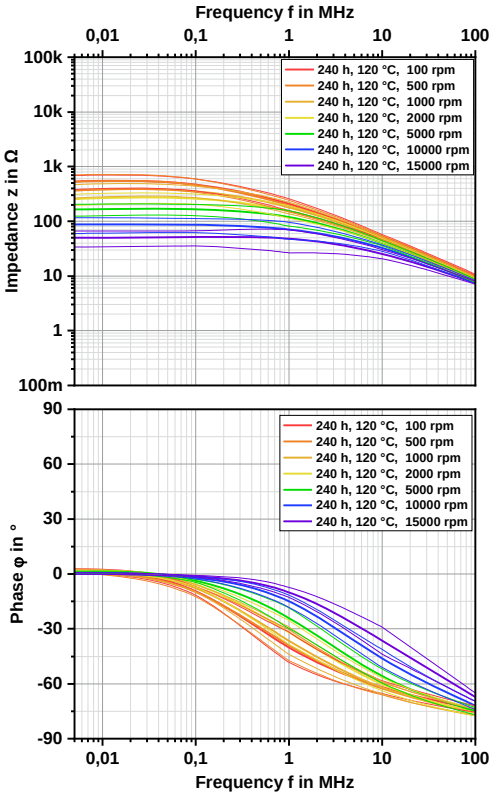

Figure 11: Impedance measurement of electrically conductive nonwoven, function-integrated on the LFS, shaft dimen-sion 32 mm at 120 °C after the endurance run

The impedance increases, especially in the lower speed range, up to approx. 600 Ω at 100 rpm. At 15,000 rpm, the impedance only increases to approx. 50 Ω.

Furthermore, the Bode diagrams clearly show that the impedance in the upper frequency range decreases and the phase angle turns negative. This behavior indicates capacities within the grounding element and its contact to the shaft, enabling shielding from electromagnetic radiation at higher frequencies. It should also be noted that, even after 240 hours, the behavior of the phase angle remains the same. In the lower frequency range, it is 0 ° and thus shows a purely resistive behavior. It has thus been proven that even after a long test period under the highest loads, there is contact between the nonwoven and the shaft and further illustrates the low wear.

The test setup used makes it possible to measure grounding elements from 30 to 150 °C and up to 30,000 rpm. It is also possible to apply a dynamic shaft runout of up to 0.2 mm. The frequency range of the measuring signal is currently between 5 kHz and 100 MHz. The further development of the measuring method also concentrates on reliably and reproducibly

measuring even higher frequencies with improved components and calibration methods, however. FST currently has several independent test cells available on which this measurement setup can be flexibly applied.

3.3. Results of friction loss measurement

Well-known and proven test methods are also used besides the impedance spectroscopy described above. The validation of the tightness and the determination of the friction loss are an integral part of the development of grounding elements at FST. The proven, highly accurate friction torque test benches were used to determine the influence of the electrically conductive nonwoven on the power loss of a sealing ring, Figure 12.

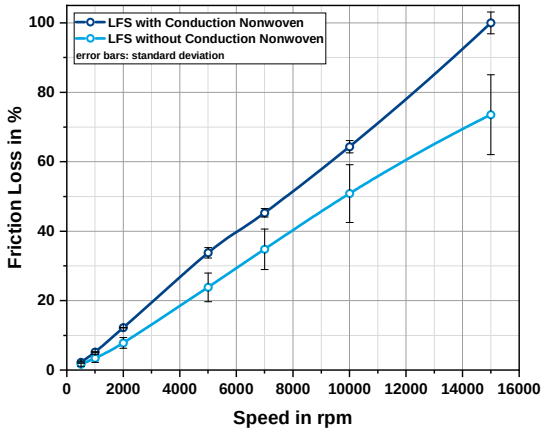

Figure 12: Measurement of power loss of a function-integrated conductive nonwoven at the Low Friction Simmerring (LFS) and the Low Friction Simmerring as a stand-alone unit

The particularly low friction of the nonwoven based solution in the range of around 20%, even at very high speeds of up to 15,000 rpm, can be seen. The air permeability of the nonwoven disc is of particular importance here, as otherwise the oil pumping capacity of the Simmerrings can lead to dangerous negative pressure formation between the grounding element and the sealing lip. Subsequent evaluation of the products therefore showed only slight material wear on all components. It should be noted that the conductive nonwoven lip fulfils an additional dirt-repellent function in addition to its main function. This enables it to keep dust, abrasive particles and dirty water away from the seal and thus from the bearing.

4. Conclusion

The results presented here impressively show how EDM damage can be prevented on the basis of the innovative nonwoven-based solution for electric motors, even under demanding and realistic operating conditions.

Table 1 shows the current developments regarding further material optimization of the conductive nonwoven (integration of even more conductive particles):

Table 1: Electromagnetic parameters of various materials [5]

Element	Conductivity (S/m)
Silver	6.21×10^7
Copper	5.80×10^7
Aluminum	3.54×10^7
Titanium	2.50×10^6
Carbon	7.25×10^4

Other possible approaches include a further optimized product design (shortening of the route) and prevention of oxidation or contamination of the contact surface. Investigations show that it is possible to even reduce the resistance values dynamically into ranges of 1-10 ohms and thus to also obtain an effective shielding product for avoiding EMI (electromagnetic interference).

Acknowledgements

We would like to thank the “Industry Research Group Bearing Currents” at the Institute for Electric Energy Conversion at the TU Darmstadt for their support. Our thanks also go to the University of Kaiserslautern and the University of York for assisting us with the test results.

References

[1] *Minimal Resistance - Conductive Seals Promote High Power Density in Electric Powertrains*, press release Freudenber Sealing Technologies, September 2019

[2] Bearing Wear Condition Identification on Converterfed Motors,
H. Tischmacher, 2018 International Symposium on Power Electronics, Electrical Drives, Automomation and Motion (SPEEDAM), Conference paper, publisher IEEE

[3] Application guide bearing currents – Technische Universität Darmstadt (Germany), Institut für elektrische Energiewandlung, 15.03. 2019 Version 1.5

[4] H. Tischmacher, “Systemanalysen zur elektrischen Belastung von Wälzlagern bei umrichtergespeisten Elektromotoren,” Dissertation, Technische Universität Hannover, Germany, 2017.

[5] Dr. Andrew Austin, modeling the electromagnetic properties of conductive nonwoven fabrics, university of York, february 2017

[6] R&S®ZNL Vector Network Analyzer - The 3-in-1 allrounder, Product Brochure | Version 01.01

Dimensional stability on Fatigue Performance of Wheel Bearing Rolling Elements: Case studies

S.Rizzo[1], C.Sammarco[1], E.Brusa[2], R.Sesana[2]

[1] *Product Development, Tsubaki Nakashima Co., Ltd, sebastiano.rizzo@europe.tsubaki-nakashima.com*
Product Development, Tsubaki Nakashima Co., Ltd, cosimo.sammarco@europe.tsubaki-nakashima.com
[2] *DIMEAS, Politecnico di Torino, eugenio.brusa@polito.it*
DIMEAS, Politecnico di Torino, raffaella.sesana@polito.it

Abstract– Rolling bearings are critical automotive and mechanical components. For high loaded bearings, the steel rolling elements are subjected to failure having a direct impact on overall bearing fatigue life performance. Fatigue phenomena involve both rolling contact fatigue and material fatigue damage processes.

Metallurgical, mechanical, geometrical, physical properties affect fatigue behavior and they can be controlled also by precise manufacturing process parameters. Despite accurate manufacturing, during the working condition, dimensional stability of some rolling elements within the bearing can be affected and distribution of stresses can strongly change with respect to design thus affecting fatigue performance. Failure can then occur for load values different and lower from design indications.

In the present research 100Cr6 and 100CrMnSi6-4 steel alloys, undergoing different thermal treatments, involving hardening, undercooling and tempering are analyzed. Rolling elements in the selected alloys are subjected to fatigue tests on automotive wheel hub bearing units and, while testing and after failure, metallurgical and dimensional parameters are measured.

The present paper reports about failure cases in rolling elements and investigates on the relation between dimensional stability and fatigue performance involving metallurgical, processing and dimensional analysis; considering the different fatigue performance as well as the different metallurgical and mechanical behavior obtained by testing rolling elements from different combinations of steel alloys and thermal treatment, it is possible to conclude how the rolling element dimensional stability can sensibly affect the bearing fatigue life, especially under severe conditions in terms of applied load, speed and temperature.

Keywords – Bearing, RCF, Rolling elements, Dimensional stability.

1. Introduction

The typical factors which influence the fatigue life of rolling elements within bearings are metallurgical, mechanical, and physical properties, considering the same application conditions; focusing on the last category,

geometrical characteristics of rolling elements can induce vibrations in running conditions; this can reduce the fatigue life due to higher surface pitting phenomena.

During running the bearing elements are subjected to a dimensional variation which results in a non-constancy of the operating conditions.

Dimensional stability of the rolling elements is the capability to maintain its dimension along the life-cycle of the components. One of the goals of this study is to correlate dimensional stability with fatigue performances of rolling elements.

One of the key factors influencing dimensional stability is the retained austenite content of the AISI 52100 steel [1]. Sub-zero heat treatment performed after quenching markedly reduces the amount of not-stable retained austenite. [2]

The second goal of this study is to correlate the influence of silicon and manganese on the fatigue performance of rolling elements directly related to dimensional stability. The presence of silicon in bearing steels improves the stability of the retained austenite [3].

2. Materials and methods

The fatigue performances of two materials have been evaluated by rig tests. Eight tests were performed for each material/heat treatment combination under identical conditions.

Rig tests are structured with an electrical motor that drives a rotating shaft on which the inner rings of two double row ball bearings are trapped. The rotary motion of the outer rings was prevented by the external fluted shell. The applied load is axial and is guaranteed by a pneumo-hydraulic pistons system. The temperature of the outer ring, the vibration of the system, and the applied load were controlled for the duration of the test using all the necessary transducers. Within each tested, first-generation wheel bearing, only one row was filled with balls due to the unidirectionality of the axial load. Lubrication was performed using mineral grease. To evaluate the performance of the balls, tests were focused on only one of the two bearings trapped on the shaft, on which the contact pressures were designed to be much higher (3.8 GPa maximum Hertzian pressure on surface, on ball-IR contact).

Tests are designed by testing blocks; races, grease and cages are changed at the end of each of them. At the same moment dimensional parameters of rolling elements are measured and surfaces are inspected.

Fatigue tests were performed on samples described in table 1.

Table 1 - Sample description

Sample id.	Test A	Test B	Test C
Steel alloy	100Cr6	100Cr6	100CrMnSi6-4
Quench	850°C, Oil	850°C, Oil	860°C, Oil
Subcooling	-	-70°C	-
Tempering	150°C	220°C	240°C
Resultant HRC (AVG)	62.1	61.0	60.1

3. Results

Concerning the rolling elements behavior in terms of dimensional stability, it is noteworthy how retained austenite of Sample "A" started transforming into martensite phase in the early testing moments, causing a general volume increase; in the second part of test life, the surface wear phenomena cause a dimensional reduction comparable with the austenite transformation effect.

Sample "B" showed quite absent retained austenite before starting tests, which caused a lower transformation rate respect to Sample "A": such behavior caused the inappreciability of the volume increase effect respect to the reduction one related to surface wear.

Sample "C" showed a retained austenite amount higher than Sample "A" one before test starting, but the different chemical composition caused a higher metallurgical stability which implied a behavior similar to the one occurred to Sample "B".

The above described results are showed by the figure 1, representing the dimensional measurements performed at the end of each testing block (triangles represent ball failures, dots represent measurements at testing block end).

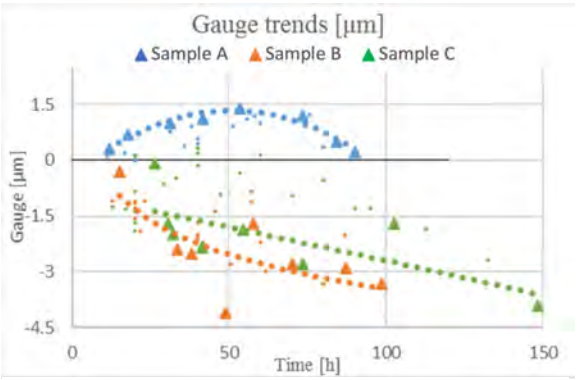

Figure 1 - Gauge trends

Figure 2 and figure 3 show the retained austenite levels measured before and after testing by XRD equipment with ±0.7% accuracy, considering the longest life test for each sample.

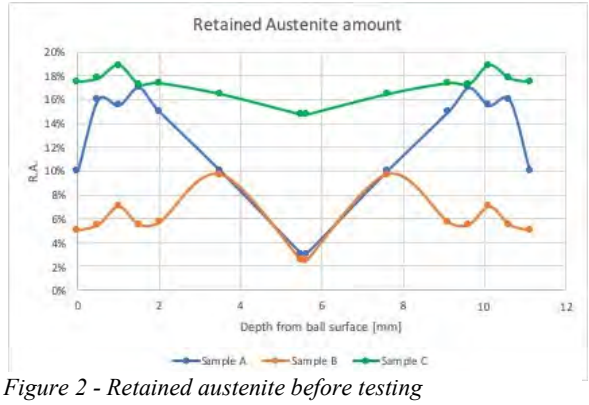

Figure 2 - Retained austenite before testing

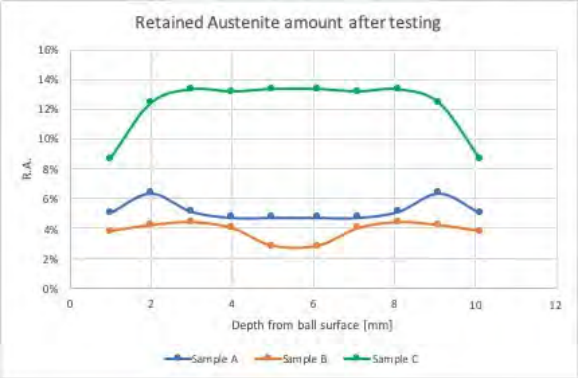

Figure 3 - Retained austenite after testing

The rolling elements failure mode were also inspected: figure 4, figure 5 and figure 6 show an example of fracture surface from sample "A", sample "B" and sample "C": the pictures are considered as representative of the whole samples, since no NMI issue was highlighted neither by the steel inspection, nor by the fracture surfaces. As shown by the below figures, sample "A" and sample "C" reached failure with similar mechanic behavior: subsurface spalling induced by the high RCF stress applied. Contrarywise, sample "B" showed a brittle failure behavior: the absence of retained austenite phase facilitated the crack propagation, causing a faster and more dangerous breakage [4].

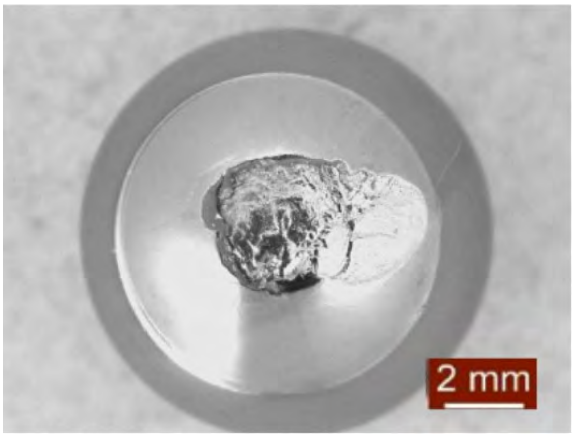

Figure 4 - Sample A failure mode

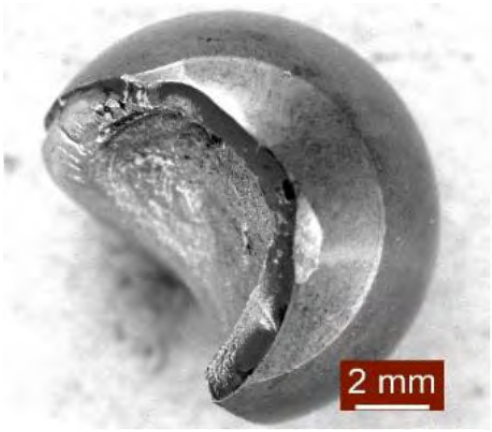

Figure 5 - Sample B failure mode

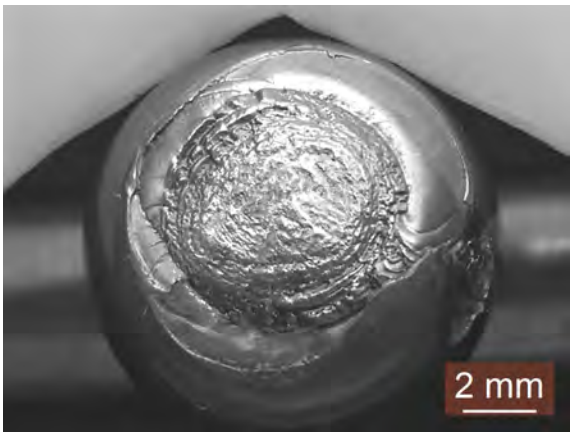

Figure 6 - Sample C failure mode

Moreover, the fracture location respect to ball poles and equator occurred randomly.

4. Conclusions

The goal of this study was to deepen the correlation between rolling contact fatigue performances and bearing rolling elements dimensional stability. To do so, three different rolling elements samples were manufactured following different processes: sample "A" by standard process setup, 100Cr6 steel quenched and tempered at 150°C; sample "B" by adding a sub-cooling at -70°C between quenching and 220°C tempering; sample "C" by applying a different steel composition using 100CrMnSi6-4, quenched and tempered at 240°C. The results obtained by testing such rolling elements showed different behaviors in terms of dimensional stability: sample "A" showed a dimension increase during the first testing phase, which was overcome during the second phase by the wear phenomena; sample "B" and sample "C" showed similar behavior: the dimensional increase related to retained austenite transformation occurred at lower rate respect to fatigue wear phenomena. The dimensional lower increasing rate obtained by samples "B" and "C" is related to the retained austenite stability: the sample "B" showed quite absent Gamma phase due to the subcooling heat treatment suffered, while sample "C" showed higher level of Gamma phase, which was kept stable by the higher Silicon and Manganese content respect to samples "A" and "B".

The below reported figure 7 shows the Weibull Distribution of the three samples: the larger scattering of sample "C" is related to the higher survived specimen's population obtained by fatigue testing. The specimen's quantity considered for the statistical analysis is the same for each sample.

The main difference highlighted by "B" and "C" samples is related to fracture mode: while sample "B" showed a brittle fracture rolling element breakage, sample "C" showed a ductile behavior with the typical subsurface spalling. Considering also that fatigue performances obtained by samples "B" and "C" showed L_{10} increase of 38% and 48% respectively if compared to sample "A", it is possible to conclude how the higher dimensional stability can lead to higher fatigue performance of the whole bearing.

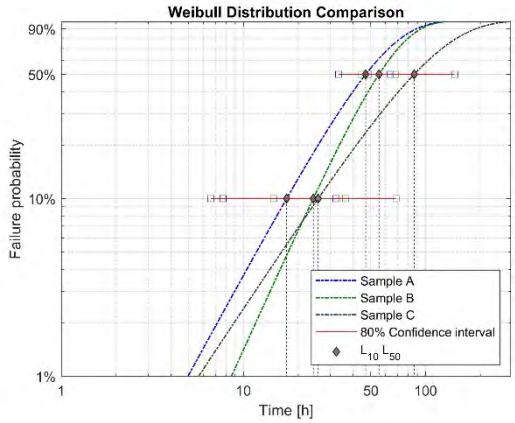

Figure 7 – Weibull distribution

5. References

[1] Rizzo, S. and Pagliassotto, S.: "Fatigue Performance Improvements of Wheel Bearing Rolling Elements", SAE Int. J. Passeng.Cars - Mech. Syst. 10(3): 2017, doi:10.4271/2017-01-2524.

[2] Sri Siva R., Arockia Jaswin M. and Mohan Lal D., "Enhancing the wear resistance of 100Cr6 bearing steel using cryogenic treatment", Tribology transactions (2012).

[3] Efremenko V.G., Shimizu K., Noguchi T., Efremenko A.V. et al., "Impact-abrasive-corrosion-wear of Fe-based alloys: Influence of microstructure and chemical composition upon wear resistance", Elsevier - Wear (2013).

[4] Baldissera, P. and Delprete, C.: "Fatigue focused optimization of treatment parameters - A case study about Deep Cryogenic Treatment". In: Advances in Fracture and Damage Mechanics X / Tonković Z, Aliabadi MH. Trans Tech Publications, Uetikon, 498-501 (2012).

The influence of oscillation sequences on rolling bearing wear

Matthias Stammler[1], Gerhard Poll[2], Andreas Reuter[1]

[1] *Fraunhofer IWES, matthias.stammler@iwes.fraunhofer.de*

[2] *Institute for Machine Design and Tribology, Leibniz University Hannover, poll@imkt.uni-hannover.de*

Abstract– Oscillating applications for rolling bearings include construction machinery like cranes and excavators and wind turbine pitch and yaw bearings. Due to the widespread use and the specific challenges of wind energy, oscillating applications have gained increased attention by the scientific community in the last years. In wind turbines, the amplitudes, their mean values and external loads of oscillations vary. In this paper, the authors examine the effect of different sequences of oscillations on rolling bearing wear by the means of tests with 7220 type bearings. Loads and kinematic parameters are downscaled from wind turbine applications; the lubricant is a fully formulated grease.

To compare different sequences of oscillations, a reference test with 40.000 cycles of 3.95° double amplitude and 2.5 GPa contact pressure was varied. Constant, small amplitudes produced clearly visible damage patches on the bearing rings. The bearing rings had no visible surface damage if larger movements of 79° each 10 cycles interrupted the small-amplitude movements. We named such large movements protection runs. Protection runs are effective, even if their movement is interrupted by pauses or small reverse movements. These results show that the sequence of varying oscillations has a significant influence on wear risk.

Keywords – wear, oscillation, rolling bearings, pitch bearings

1. Introduction

Rolling bearings rotate constantly in most industrial applications. Doing so, they are able to build up a lubricant film that separates the rolling elements from the raceways. If properly mounted, lubricated and maintained, damages of rolling bearing in rotating applications limit mostly to rolling contact fatigue. This damage mode was subject of various scientific and engineering research projects during the last decades. [1]

In some applications, the bearings do not execute full rotations. Such applications include slewing bearings for cranes and building machinery, headsets of bicycles and wind turbine bearings, namely pitch and yaw bearings. With a high number of oscillations, the large dimensions and the varying dynamic loads, wind turbine pitch bearings (see Figure 1) face the most challenging conditions [2, 3].

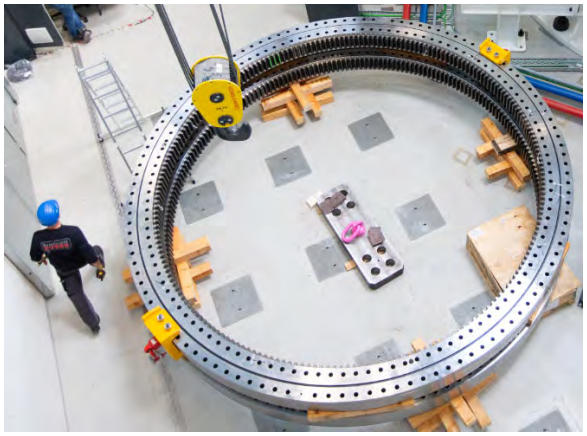

Figure 1: IMO type 12480 pitch bearings with 5m diameter

Applied research on oscillating bearings is mostly limited in two ways: The dimensions of the bearings and the variance in operating parameters. For economic reasons, bearings with less than 100 mm outer diameter are in widespread use. For similar reasons, most test rigs for oscillating applications use constantly rotating drives and eccentric rods to convert the rotation into oscillations with constant amplitudes. This is valid for scientific works [4–6] and standardized tests like NFT and ASTM [7, 8]

First works range back to the year 1937, when ALMEN reported on wear phenomena in ostensibly motionless car hub bearings during ship transport [9]. PITROFF [10] and later BREWARD [11] focussed on similar applications.

THIEDE [12] and BOSSE [13] published test results on oscillating bearings with grease lubrication. The varied operating parameters included temperature, amplitude and frequency.

The universities of Hanover [14, 15], Magdeburg [6] and Mannheim [16, 17] (in alphabetical order) contributed to the science of oscillating bearings in the recent years. For their research they used grease-lubricated bearings. The test rigs were able to vary load, amplitudes and frequencies. In none of the publications, the amplitude varied within individual tests.

GODFREY [18], ERRICHELLO [19] and SCHWACK [14] took on the task of establishing a clear differentiation between the main damage modes False Brinelling and Fretting Corrosion.

Several works sponsored by the Forschungsvereinigung Antriebstechnik underline the influence of tribolayers on the formation and growth of wear damage. A tribolayer is a thin layer of reactive products that forms on the raceway. This layer is less prone to adhesive wear in rolling contacts and thus protects the raceway. Formation of tribolayers depends on three conditions: Presence of reactive components (among them, oxygen and additives of the lubricant), energy supply and the right time windows for the reaction. The energy supply is a rolling body passing a certain

area of the raceway under load. The time depends on how soon the next rolling body passes the same area. [20–23]

The current state of science on oscillating applications does not take into account the formation of tribolayers. This makes perfect sense, as most applications, the causes for False Brinelling and Fretting Corrosion (like standstill marks) come at constant amplitudes. Tribolayer formation relies on larger movements that uncover and cover certain areas of the raceway to allow chemical reactions. Only recently, advanced load control mechanisms of wind turbines changed this picture, as they introduced a substantial variance in amplitudes and loads at a very high number of cycles [24].

A fierce competition in the wind turbine market and the drastically falling prices for turbines make load control mechanisms a must-have for current and future wind turbines. While most issues about the application are solved, the pitch bearings, which connect rotor hub and rotor blades and allow the turning of the blades to control aerodynamic loads, still call for further investigation.

In particular, a better understanding of the influence of varying amplitudes on wear phenomena motivates the present work. Unlike previous works, the tests we describe comprised different sequences of amplitudes.

2. Methodology

2.1. Bearings

We used type 7220 angular contact ball bearings for this work. Table 1 lists their main properties. The bearings have a plastic cage and no integrated sealings. The bearings are grease-lubricated, the grease is a fully formulated grease typically used in wind-turbine pitch bearings. The grease contains solid lubricants and extreme pressure additives, the soap is lithium-based and the base oil viscosity is 50 mm²/s at 40°C.

Table 1: Type 7220 bearing properties

Property	Unit	Value
Outer diameter	mm	180
Inner diameter	mm	100
Ball diameter	mm	25.4
Contact angle	°	40
Number of balls	-	15

With an outer axial load of 90 kN, the contact pressure P equals 2470 MPa (calculations according to [1]), and the width of the contact patch $2b$ is 0.8882 mm.

Figure 2:7220 bearing on IMO type 12480 pitch bearing

2.2. Test rig

The test rig combines static axial load application with a servo drive that can realize any movement from very small oscillation to full rotations. Figure 3 and Figure 4 give overviews of the design. A manual hydraulic pump applies pressure to the rigging cylinder (lime colour in Figure 3) which translates the pressure into axial force. The load application suffers from two par-asitical load paths, one being the internal friction of the cylinder and the other one a load transfer from the outer ring of the cylinder-side bearing to the housing of the mechanical assembly. For the test purpose of un-derstanding the influence of movement patterns, it is not mandatory to determine the absolute value of the load, the certainty to apply loads at a magnitude that causes surface wear suffices.

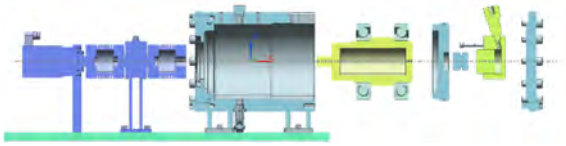

Figure 3: Test rig section view

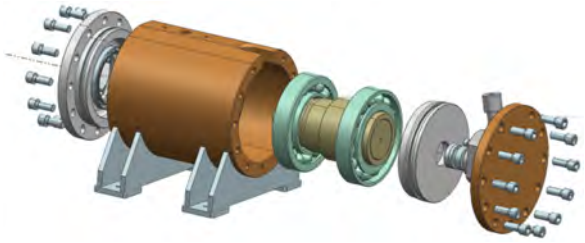

Figure 4: Mechanical assembly of test rig

The test rig has a torque and position measurement, the maximum torque is 50 Nm.

2.3. Test plan

In previous publications, the authors stated the importance of the relation between the ball travel distance x and the contact width $2b$ when describing oscillating movements of bearings. The ratio $x/2b$ is independent of bearing sizes and allows scaling of oscillatory movements. [2, 3, 25]

Based on previous experiences in pitch bearings tests, we defined a reference travel distance of 3.95° which corresponds to an $x/2b$ of 4.7. In pitch bearings, this ratio results in pitch angles between 0.4 and 1° (depending on the diameter), which are typical angles during operation. With this reference travel distance, we defined a reference test with 40.000 cycles, an axial load of 90 kN, and a speed of 4°/s (Test ID 1, see Figure 5).

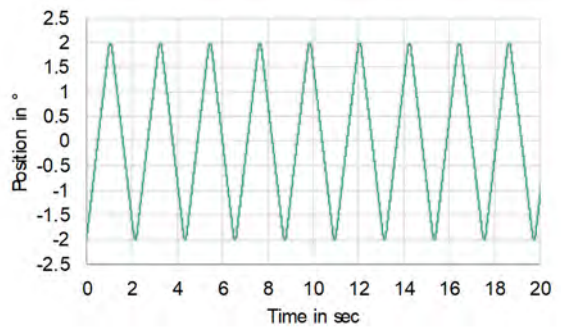

Figure 5: Motion pattern in reference test

Table 2 lists all tests. The first column contains an ID, which identifies the individual test. All tests stem from the reference test and vary the amplitude or add additional longer movements (protection runs). Test ID 4 for instance contains the same 40.000 cycles of 3.95° double amplitude, but adds an additional oscillation with 19.75° travel each 40 cycles. Table 2 lists all tests. Test ID 2 has an increased double amplitude of 8.74° (corresponding to an $x/2b$ of 12) to evaluate a possible upper limit of wear creation.

Test ID 3 attempts to vary test ID 1 and 2 in a way that is more representative for pitch bearings. Pitch bearings seldom operate with constant amplitudes, as variations in the incoming wind flow of the turbine call for different pitch angles. Thus, this test has random double amplitudes. All of these share the upper turning position, as this behaviour reflects certain types of wind turbine controllers.

Test IDs 4 to 8 include different variants of protection runs. ID 4 has a double amplitude of 19.75°. This amplitude is 5 times higher than that of the reference oscillations. To the knowledge of the authors, there are no values for effective protection runs available, as such this value was chosen arbitrarily. This test resulted in damaged raceways, and in consequence, the amplitude of the protection runs was set to a significantly higher value (79°) for test IDs 5 to 8. In addition to these tests, one test with full rotations at a speed of 4°/s and the same load ensured that the test conditions do not cause wear if the bearing does not oscillate.

Table 2: Test plan

Test ID	Description	Visualization
1	Constant oscillations 3.95° *Bearing IDs 0005, 0006*	
2	Constant oscillations 8.74° *Bearing IDs 0019, 0020*	
3	Random double amplitudes between 3.5 and 17.4° *Bearing IDs 0025, 0026*	
4	Protection runs (19.75°) each 40 cycles *Bearing IDs 0007, 0008*	
5	Protection runs (79°) each 30 cycles *Bearing IDs 0009, 0010*	
6	Protection runs (79°) each 10 cycles *Bearing IDs 00021, 0022*	
7	Protection runs (79°) each 100 cycles *Bearing IDs 00023, 0024*	
8	Interrupted protection runs (79°) each 30 cycles *Bearing IDs 0017, 0018*	

2.4. Inspection of bearings after test

The objective of this work is to understand if protection runs can prevent wear damage on the raceways and rolling bodies of the bearings. A visual inspection of the raceways after test provides all necessary results. An optical microscope is used for this inspection, as it allows measuring the size of damage patches and gives a good visual impression. In case of visible damages, each damage patch on the inner ring of the bearing is inspected.

3. Results and discussion

Each test ran with two bearings. The two bearings that ran with continuous rotations did not display any wear on the raceways. The following tables contain three representative results for each test. Note that the surface of the bearings shows a reflection of the microscope lens on all pictures.

Table 3 shows damage patches for tests without protection runs. These are the tests with the ID 1, 2, and 3.

Each bearing shows a clearly visible damage patch for each rolling contact. The patches contain corrosion products and have an increased surface roughness. Test ID 2 has more than twice the travel compared to

test ID 1; the severely damaged area does not increase accordingly. Test ID 3 displays the most severe damage on the raceways, with a damage concentration on the turning point (left in all pictures) shared by all cycles.

Table 3: Test results (tests without protection runs)

Test ID	Raceway condition
1	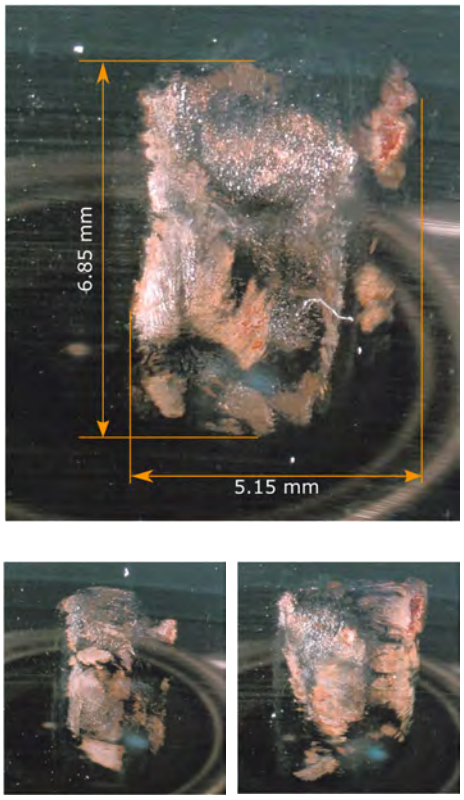
2	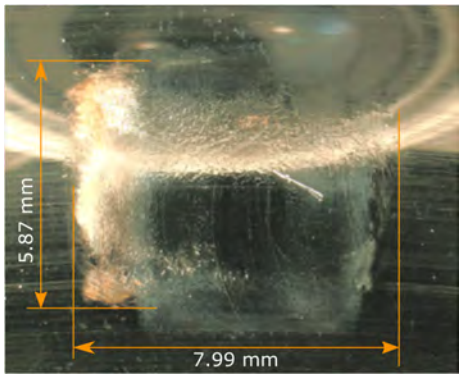 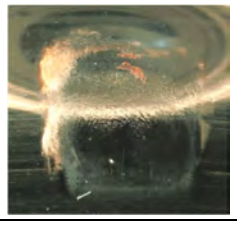 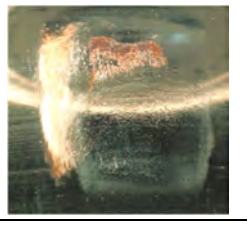
3	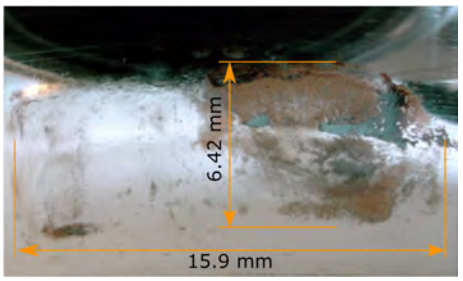 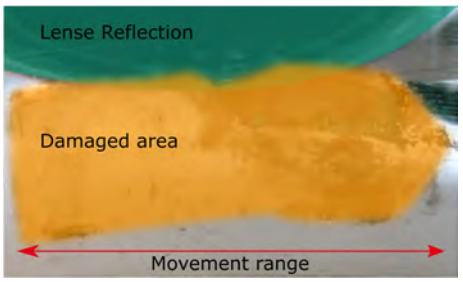  

Table 4 shows damage patches for tests with protection runs. These are the tests with the ID 4 to 8.

Test ID 4 resulted in clearly visible damage areas with corrosion products. In some of the areas, flakes broke out of the raceway surface.

Test ID 5 displays no corrosion products. The visible change on the raceway is limited to a grey area. The shape is the outline of half an ellipse and the perpendicular lines that fade out in rolling direction. The manufactured surface structure seems unchanged.

Test ID 6 does not show any changes to the raceway, similar to bearings with full rotations.

Test ID 7 shows similar results as Test ID 5. In two cases, small patches with increased roughness are visible.

Test ID 8 does not display corrosion products. The grey areas have a similar shape to Test ID 5.

Table 4: Test results (tests with protection runs)

Test ID	Raceway condition
4	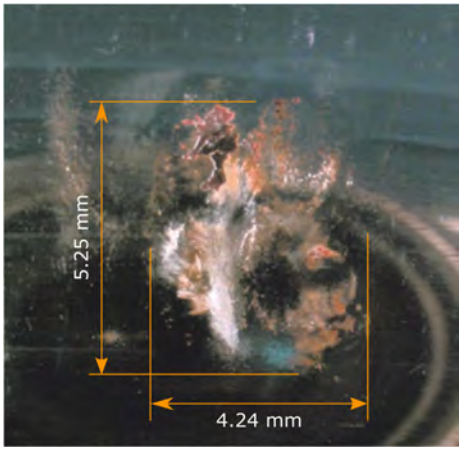 
5	 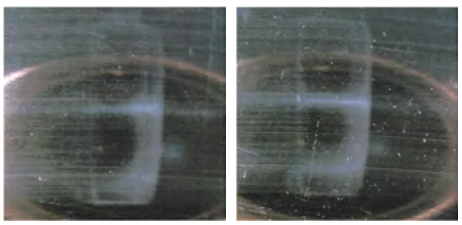
6	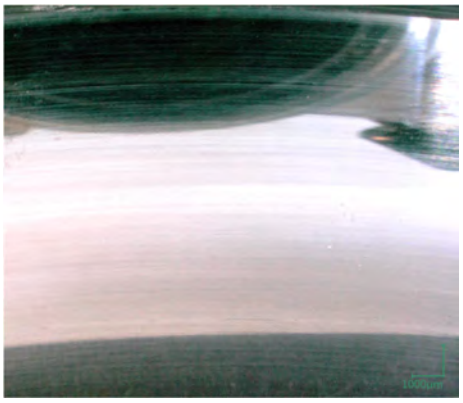 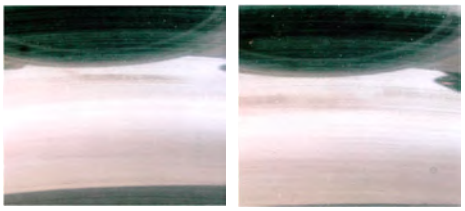
7	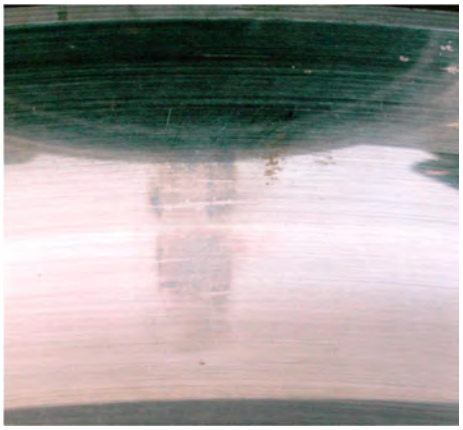 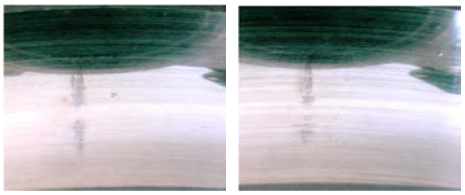

Test ID	Raceway condition
8	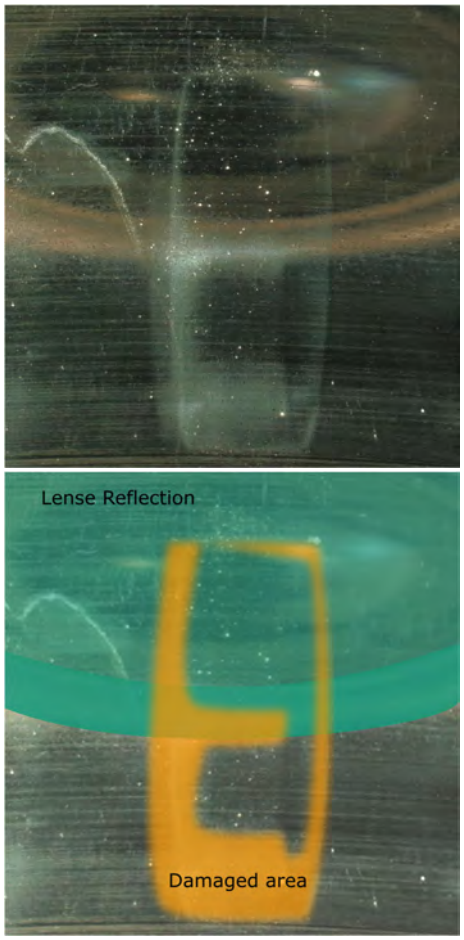

All tests without protection runs resulted in clearly visible damage marks after 40000 cycles. These damage marks contain corrosion products (hematite); the damage mode is fretting corrosion. According to [14] and [19], unlubricated conditions cause fretting corrosions. In relation to the travel of the ball on the raceway, test ID 2 displays a less severe damage than test ID 1. The authors conclude that at some point during the movement with $x/2b$ of 12, lubricant enters the contact and prevents further fretting. The existence of fretting under these conditions indicates that any x/2b equal or smaller than 12 does not suffice for a protection run.

Among the tests with protection runs, only the last four were able to prevent fretting corrosion. This most likely related to the travel of the protection run, which was shortest in test ID 4. The number of cycles in between protection runs seems less relevant for damage formation, as test IDs 5,6, and 7 demonstrate.

Test ID 4 showed, in addition to the fretting corrosion, broken flakes on the raceway. For any practical application, this test result is the most critical, as the flakes can cause more damage rapidly if they get into contact areas.

Test ID 8 showed similar results to 5. The protection run is effective, even if the movement contains interruptions. The interruptions were done at travels similar to the 3.95° of the 40.000 reference cycles. This indicates that it is not necessary to build up a lubricant film to provide the protective capacity of a larger movement. Lubricant films build up with constant, long movements. In the absence of a lubricant film, it is likely that tribolayers provide the protective effect.

4. Conclusions

This work attempts to confirm the concept of protection runs for bearings in oscillatory operation. Protection runs are large movements, which are embedded in small oscillations, and protect the raceway from wear. Protection runs are particularly relevant for pitch bearings of wind turbines that operate with varying oscillation amplitudes.

To the knowledge of the authors, no publicly available test results have previously confirmed the validity of this concept. Most available research is limited to tests with constant amplitudes.

To confirm the concept, a new test rig for 7220 type angular ball contact bearings executed tests with different oscillation sequences. The test rig has a servo drive that allows execution of any desired movement. The load on the bearings was an axial load of 90 kN.

With the results of eight different tests, each of which was carried out with two bearings, we could confirm the effectiveness of protection runs. In reference tests with constant amplitudes, the raceway displayed fretting corrosion. Tests with effective protection runs completely eliminated this Fretting Corrosion. The results indicate that a minimum travel to achieve a protective effect. Runs with shorter travel are not effective, but might even add damage to the raceway. The number of cycles in between protection runs has a minor influence on the results, with more frequent protection runs resulting in less prominent grey areas on the raceway.

Protection runs do not need to be continuous; the movement may contain interruptions.

Future work in this field will cover further variation of the travel of protection runs, the frequency, and the number of cycles in between in order to further understand the influence of these parameters. We will transfer selected test sequences to tests with 800 mm and 5 m diameter slewing bearings.

Acknowledgments

The present work was carried out with the project “HAPT – Highly Accelerated Pitch Bearing Tests”. We kindly acknowledge the project funding by the

German Federal Ministry for Economic Affairs and Energy.

The author would like to thank Fabian Schwack of the Leibniz University Hannover for his outstanding contributions to the peculiar subject of oscillating bearings, always riveting conversations and his particular talent in finding historical references on wear phenomena.

References

[1] Harris T A and Kotzalas M N 2007 *Rolling bearing analysis* (Boca Raton: CRC, Taylor & Francis)

[2] Stammler M, Reuter A and Poll G 2018 Cycle counting of roller bearing oscillations – case study of wind turbine individual pitching system *Renewable Energy Focus* **25** 40–7

[3] Stammler M and Poll G 2014 *Schadensmechanismen in Rotorblattlagern (GfT- Reibung, Schmierung und Verschleiss)* (Göttingen)

[4] Grebe M 2012 False Brinelling - Standstill marks at roller bearings *Dissertation* Faculty of Material Science, Slovak University of Technology

[5] Schwack F, Prigge F and Poll G 2018 Finite element simulation and experimental analysis of false brinelling and fretting corrosion *Tribology International* **126** 352–62

[6] FVA 2010 *False Brinelling: Stillstehende fettgeschmierte Wälzlager unter dynamischer Belastung* Forschungsvorhaben 540/I (Frankfurt)

[7] NF 1995 Aptitude à résister au faux effet Brinell *(*NFT 60-199*)*

[8] ASTM 2013 *ASTM Volume 05.02 Petroleum Products and Lubricants (II): D3711 - D6122*

[9] Almen J O 1937 Lubricants and False Brinelling of Ball and Roller Bearing *Journal of Mechanical Engineering* 415–22

[10] Pitroff H and Mundt R 1963 Riffelbildung bei Wälzlagern als Folge von Stillstandserschütterungen *VDI-Zeitschrift* **105** 1219–30

[11] Breward M J 1973 Lagerlebensdauer bei Schwingungsbeanspruchung *SKF Kugellager-Zeitschrift*

[12] FVA 1999 *Oszillierende Bewegungen: Wirkung von Schmierstoffen bei langsamen oszillierenden Gleit- und Wälzbewegungen* Forschungsvorhaben 315 (Frankfurt)

[13] FVA 2003 *Oszillierende Bewegungen: Schmierungsverhalten bei oszillierenden Gleit- und Wälzbewegungen* Forschungsvorhaben 315 II (Frankfurt)

[14] Schwack F, Byckov A, Bader N and Poll G 2017 *Time-dependent analyses of wear in oscillating bearing applications (2017 STLE Annual Meeting)* (Atlanta)

[15] Schwack F, Prigge F and Poll G 2017 *Frictional Work in Oscillating Bearings – Simulation of an Angular Contact Ball Bearing under Dry Conditions and Small Amplitudes (6th World Tribology Conference)* (Beijing, China)

[16] Grebe M, Feinle P and Blaškovitš P 2014 Failure of Roller Bearings without Macroscopic Motion - Influence of the Pivoting Angle on the Contact Mechanics and the Wear Mechanisms in the Contact between Roller and Raceway *Tribology - industrial and automotive lubrication* ed W J Bartz (Ostfildern: Techn. Akad. Esslingen)

[17] Grebe M, Feinle P and Hunsicker W 2008 Möglichkeiten zur Reduzierung von False Brinelling Schäden *Reibung, Schmierung und Verschleiss Tribologie-Fachtagung (Göttingen) (Reibung, Schmierung und Verschleiß* vol 49*)* (Aachen: GfT)

[18] Godfrey D 2003 Fretting Corrosion or False Brinelling? *Tribology & Lubrication Technology* 28–9

[19] Errichello R 2004 Another Perspective: False Brinelling and Fretting Corrosion *Tribology & Lubrication Technology* **60** 34–6

[20] FVA 1988 *Reaktionsschichtbildung: Verschleiß- und Reibungsminderung durch Reaktionsschichtbildung bei langsamlaufenden Wälzlagern und Zahnrädern* 126 I (Frankfurt)

[21] FVA 1991 *Reaktionsschichtbildung: Verschleiß - und Reibungsminderung durch Reaktionsschichtbildung bei langsamlaufenden Wälzlagern und Zahnrädern* Forschungsvorhaben 126/II (Frankfurt)

[22] FVA 2000 *Triboschutzschichtcharakterisierung: Untersuchung zur Bildung, Charakterisierung und Wirkungsweise von Triboschutzschichten* Forschungsvorhaben 289 I + II (Frankfurt)

[23] FVA 2004 *Triboschutzschichten II: Zusammenhänge zwischen Zahnrad- und Wälzlagerschäden und tribologischen Veränderungen des oberflächennahen Werkstoffbereichs* Forschungsvorhaben 289 Ib + IIb (Frankfurt)

[24] Bossanyi E A 2003 Individual Blade Pitch Control for Load Reduction *Wind Energy* **6** 119–28

[25] Schwack F, Stammler M, Poll G and Reuter A 2016 Comparison of Life Calculations for Oscillating Bearings Considering Individual Pitch Control in Wind Turbines *J. Phys.: Conf. Ser.* **753**

Numerical solution and FFT-based prediction of the hydrodynamic pressure generation of parallel rough surfaces

W. Ma[a], N. Biboulet[b], A.A. Lubrecht[b1]

[a] Jiangsu Normal University, School of Mechatronic Engineering, Xuzhou, 221116, PRC

[b] Université de Lyon, INSA-Lyon, LaMCoS, CNRS UMR 5259, Villeurbanne F69621, France

Abstract - In general, the component macro-geometry (radius of curvature) determines the pressure generation and the roughness alters it somewhat. However, for parallel surfaces, the surface micro-geometry completely determines the hydrodynamic lubrication. This paper extends earlier work to numerically solve the hydrodynamic pressure generation and load carrying capacity (LCC) of surfaces with more complicated roughness features.

An FFT-based method is described to obtain the pressure distribution rapidly. The method is applicable to both measured surface topographies and artificially generated rough surfaces. Results show that it enables one to predict the hydrodynamic pressure, when cavitation is negligible. The relative error of the LCC over the central domain is smaller than 8% while a 500× time saving, compared to the numerical method, is obtained.

Keywords - hydrodynamic lubrication, parallel surfaces, load carrying capacity, FFT techniques

Notation

Amp	height amplitude of a sinusoidal surface
cl	correlation length of surface
dpm	pressure amplitude of sinusoidal surface
dpm_x	pressure amplitude of isotropic sinusoidal surface
h	film thickness
H	dimensionless film thickness, $H = h/h_0$
h_0	nominal film thickness (flying height)
h_s	roughness of the surface measured from the mean-height plane
L_x	domain length in x direction
L_y	domain length in y direction
N_x	number of grid points in x direction
N_y	number of grid points in y direction
p	pressure
P	dimensionless pressure, $P = p/(12\eta u_m L_x/{h_0}^2)$
p_a	ambient pressure
p_c	cavitation pressure
p_0	boundary pressure, the difference between p_a and p_c and the cavitation pressure, $p_0 = 3 \times 10^4$ [Pa]
rms_h	RMS roughness of surface
t	time
u_m	mean surface velocity, $u_m = 0.5$ [m/s]
x	coordinate in the direction of sliding
X	dimensionless coordinate, $X = x/L_x$
y	coordinate perpendicular to the direction of sliding
Y	dimensionless coordinate, $Y = y/L_x$
ϵ	perturbation parameter
η	oil viscosity, $\eta = 0.01$ [Pa·s]
θ	cavitation fraction
λ_x	wavelength in x direction
λ_y	wavelength in y direction
φ_x	phase in x direction
φ_y	phase in y direction
DFT	discrete Fourier transform
FFT	fast Fourier transform
IFFT	inverse fast Fourier transform
LCC	load carrying capacity [Pa]
OCR	oil control ring
PRCL	piston ring - cylinder liner
PSD	power spectral density
RMS	root mean square

[1] ton.lubrecht@insa-lyon.fr

1. Introduction

Surface roughness influences the tribological performance of lubricated contacts, especially for cases of parallel surfaces, in terms of LCC, etc..

In 1966, Hamilton et al. [1] found that micro irregularities on the surfaces of rotary-shaft seals led to hydrodynamic pressure build-up. They observed local cavitation at the divergent part of the asperities by using a transparent rotor and proposed that it was the mechanism responsible for the observed load support. Different from the classical case where a single cavitation boundary occurs at the contact outlet, this kind of cavitation occurs inside the contact zone and is normally called inter-asperity cavitation [2, 3]. This inter-asperity cavitation has also been experimentally observed by Stakenborg [4], Qiu et al. [5] and Zhang et al. [6].

However, later studies have concluded that inter-asperity cavitation is not the sole source of load support [7, 8]. As stated in the review paper [9]: only in certain cases does it lead to additional load support, i.e. in fully textured contacts. Furthermore, in some cases, the load support may even be negative, depending on the shape of the asymmetric pressure distribution. For partially textured surfaces and certain cavitation pressure conditions, significant pressure can build up, leading to an important load support.

Accurate pressure distribution predictions require a mass-conservation treatment of cavitation, otherwise the cavitation area is underestimated [10, 11]. Interest in incorporating a mass-conserving cavitation algorithm into the numerical solution of hydrodynamic pressure of parallel surfaces, especially textured surfaces, has been substantial over the last two decades [9]. Examples can be found in [12, 13, 14, 15, 16] for parallel bearings, in [17, 18, 19, 20] for rotatory-shaft seals and in [21, 22, 23, 24] for piston ring-cylinder liner (PRCL) contacts.

As for the surface micro-asperities, surface roughness is generally considered random and in contrast, surface texturing describes well-defined features (discrete dimples, grooves) [9]. One of the first successful commercial applications of surface texturing is that of cylinder liners of internal combustion engines [25].

More recently, studies on the tribological performance of cylinder liners have been conducted by Tomanik et al. [26] for real surface topographies, by Yin et al. [27] for laser-textured surfaces and by Noutary et al. [28] for artificially-textured surfaces. Tomanik et al. [26] investigated the effect of waviness and roughness of the cylinder liner on the hydrodynamic and asperity pressures by using the measured topographies from two mirror-like coated bores. The simulation results reveal that most of the fluid pressure is generated by the honing grooves rather than by the localized pores on the coated surfaces. The two coated bore surfaces generate significantly higher hydrodynamic pressure and lower asperity contacts, compared with regular topographies. It is worth noting that these conclusions were obtained based on the same operating conditions of h_0/rms_h, not h_0 (see Notation section). A more in-depth discussion on the effect of dimples on lubrication can be found in [23, 28, 29]. Noutary et al. [28] found that partial texturing with micro dimples can induce positive pressure when the textured zone is located in the inlet.

Woloszynski et al. [30] developed an efficient algorithm, called Fischer-Burmeister-Newton-Schur (FBNS), for the joint solution of the Reynolds equation with mass-conserving cavitation and the Fischer-Burmeister equation for complementarity. They benchmarked the efficiency of the FBNS code which roughly yields two orders of magnitude reduction in computing time when compared against other algorithms, such as the augmented iterative Elrod-Adams $p-\theta$ [31], the exact linear complementarity based on pivoting [32] and the modified switch function $\varphi - g$ [33]. Biboulet et al. [34] developed an efficient global grid refinement solver which originates from the work of Woloszynski et al. [30], using the same mass-conserving cavitation algorithm as [28].

The solver by Biboulet et al. has shown a fast and stable convergence for parallel surfaces with sinusoidal roughness or regular dimple texturing. As an extension of [34], the current paper studies the hydrodynamic pressure of parallel surfaces with more complicated surface micro-structures. The authors used the cylinder bore surface topography, named "MLJ" in [26]. It is form-removed and then waviness-filtered.

Additionally, an FFT-based method is proposed to rapidly obtain the pressure distribution. The method is based on an approximate solution of sinusoidal roughness with standard perturbation techniques. Solutions of the perturbed Reynolds equation can be found in the work of Choy et al. [35] and Kim et al. [36]. The method is suitable to non-cavitation cases where the hydrodynamic lubrication problem remains approximately linear.

2. Theory

The main assumptions are those of a laminar flow regime under isothermal conditions. The dimensionless Reynolds equation with cavitation (mass-conserving) and the dimensionless Fischer-Burmeister equation are solved simultaneously:

$$\frac{\partial}{\partial X}\left(H^3\frac{\partial P}{\partial X}\right)+\frac{\partial}{\partial Y}\left(H^3\frac{\partial P}{\partial Y}\right)=\frac{\partial((1-\theta)H)}{\partial X} \qquad (1)$$

$$P+\theta-\sqrt{P^2+\theta^2}=0 \qquad (2)$$

where H is the dimensionless gap; P is the dimensionless pressure; X is the dimensionless sliding direction; Y is perpendicular to X; θ is the cavitation fraction. Eq.(2) indicates the complementarity: $\theta = 0$ and $P > 0$; $0 < \theta < 1$ and $P = 0$.

Using finite difference techniques, these equations are discretized and a local Jacobian linearisation is used. A grid refinement strategy is used to quickly converge the cavitation boundaries. The implementation details and the validation of the numerical solver are presented in [34].

For evaluating the relative central mean pressure, we define

$$LCC/(0.25L_x\, L_y) = \sum_{N_x/2} \sum_{N_y/2} p(x,y)/ (0.25N_x\, N_y) - p_0 \quad (3)$$

using the LCC over the central domain. p_0, the boundary pressure, is the difference between the ambient pressure and the cavitation pressure; L_x (L_y) is the length of the domain in the x (y) direction; N_x (N_y) is the number of the discrete points in the x (y) direction.

3. Numerical results

As an example, we solved the hydrodynamic pressure of a cylinder liner - oil control ring (OCR) using the numerical method. The moving ring surface is considered to be smooth.

The stationary surface is measured from a coated cylinder bore surface, called "MLJ" in [26]. The surface size is $L_x \times L_y$ =0.8 × 0.8 mm^2 and the RMS roughness is 0.073 μm. The operating conditions are listed in Table 1. We solved two cases with h_0=2 μm and h_0=1 μm.

The number of points on the finest grid is $N_x \times N_y$= 1024 × 1024. The hydrodynamic pressure results are shown in Figure 1. For the first case (Figure 1(b)), no cavitation occurs.

Table 1: Operating conditions.

Parameter	Value
Oil viscosity, η	0.01 [Pa·s]
Mean surface velocity, u_m	0.5 [m/s]
Sliding direction,	$+x$
Boundary pressure, p_0	3×10^4 [Pa]

With the smooth OCR surface moving forwards ($+x$ direction), the grooves of the rough cylinder liner suck in oil, which leads to a low pressure zone inside the grooves and slightly to its left. Cavitation occurs if the pressure drops below the cavitation pressure. In Figure 1(c), the pressure variation becomes larger due to the relatively larger variation of the geometry $h_0 = 1$ μm. Behind the grooves, high pressure is built up, which is clearly visible for the biggest groove. This is in accordance with the description by Tomanik et al. [26]: most of the hydrodynamic pressure was generated by the honing grooves rather than by the localized pores. The hydrodynamic pressure rise tends to occur at the convergent portion of the honing grooves and extends onto the smooth plateau region behind the grooves.

As in [28], we know that the pressure build-up is dependent on the length of the plateau: the larger the length, the higher the pressure.

By comparing the pressurized (full-film) zone behind the biggest groove, one finds that the local pressure in the second case with $h_0 = 1$ μm is much higher than for $h_0 = 2$ μm. As explained by Harp and Salant [3], the pressure elevation is a result of the near-by inter-asperity cavitation.

But this does not mean that the LCC in the second case (with cavitation) is higher. The calculation results of the average pressure $LCC/(0.25L_x\, L_y)$ are -9.8 × 10^3 Pa for $h_0 = 1$ μm and 5.43 × 10^3 Pa for $h_0 = 2$ μm.

Therefore, as concluded by Gropper et al. [9] through a review of many papers on the hydrodynamic lubrication of textured surfaces, cavitation cannot and should not be named as the responsible load support mechanism and the influence of cavitation highly depends on the operating conditions.

The hydrodynamic-lubrication performance (pressure build-up, cavitation, LCC, etc.) of parallel surfaces is influenced not only by the surface structure, the flying height but also by the difference of the ambient pressure and the cavitation pressure.

The parameter h_0/rms_h shows the relative importance of roughness effects [37]. From the work by Harp et al. [2], one also knows that h_0/rms_h and p_0 are the key indicators for cavitation. With other operating conditions being constant, as both h_0/rms_h and p_0 decrease, the extent of cavitation is expected to increase. In this paper, $p_0 = 3 \times 10^4$ Pa is used for all calculations. For the pressure distribution without cavitation (Figure 1(b)), h_0/rms_h= 27.4 is used, while for the pressure distribution with cavitation (Figure 1(c)), h_0/rms_h= 13.7 is used. Please note that the pressure scale of Figure 1(c) is exactly twice the scale of Figure 1(b)! When h_0 is much larger than the rms_h, the surface roughness has a weak effect and grooves play a less dominant role. Consequently, cavitation disappears.

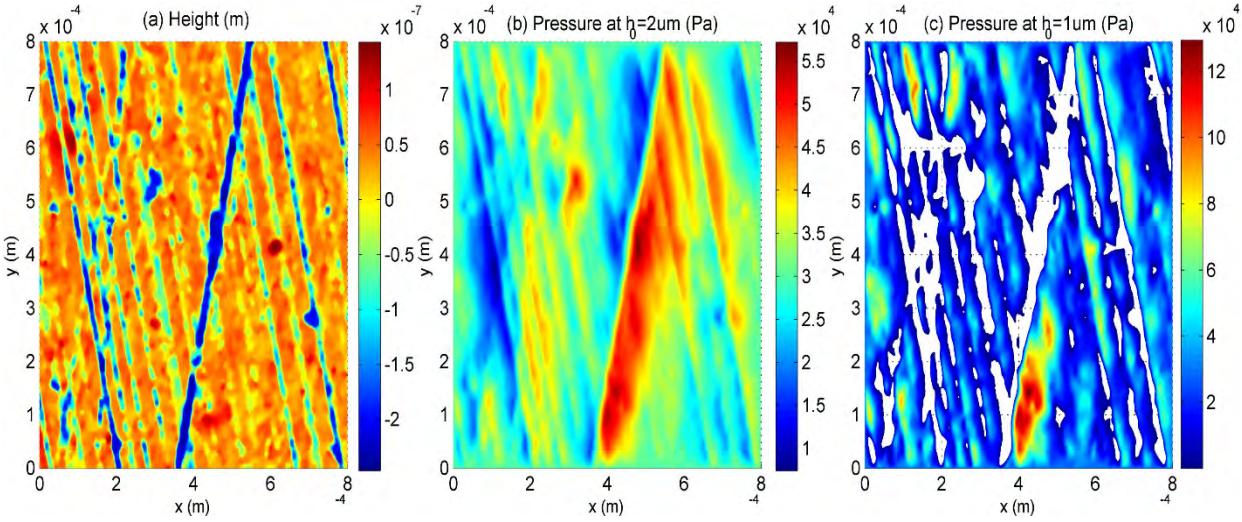

Figure 1: Cylinder liner surface: (a) height distribution, (b) pressure at $h_0 = 2\ \mu m$ and (c) pressure at $h_0 = 1\ \mu m$. Note: cavitation is represented by the white areas.

The computing times are respectively 194 s and 243 s with a very small residual error up to 1×10^{-10}. As a grid refinement strategy is used, the calculation for cavitating cases only needs slightly more time to converge [34]. In order to analyse the numerical accuracy, we solved the first case ($h_0 = 2\ \mu$m) on two other grids as. The LCC results are shown in Table 2.

Table 2: Numerical calculation results on different grids

Grid: $N_x \times N_y$	$LCC/(0.25 L_x\ L_y)$ [Pa]	Computing time [s]
512 × 512	5.57×10^3	43
1024× 1024	5.43×10^3	184
2048× 2048	5.32×10^3	1291

The difference between the solutions on the coarser grids is 3%. That for the finer grids is 2%. The computing time on grid 1024 × 1024 is roughly 4 times that on grid 512 × 512. But the time consumption increase for grid 2048 × 2048 is considerable. To pursue fast calculation, we propose an efficient pressure-prediction method based on perturbation techniques and FFT. It is precise for cases where cavitation plays a minor role.

4. Pressure prediction

4.1. Approximate solution using perturbation techniques

The film thickness is given by $h(x,y) = h_0 - h_s(x,y)$, where h_s is the surface roughness function. When the surface amplitude is small, h_s can be seen Solutions of p_1 take the form of $\cos(2\pi\, x/\lambda_x + \varphi_x)\sin(2\pi\, y/\lambda_y + \varphi_y)$, illustrated by Figure 2. As the original waviness uses sine functions, the solution is written, with a phase shift of $\pi/2$ in the x direction, as:

as a perturbation term. The function h in the left-hand side of the Reynolds equation (Eq.(1) in dimensional form) can be approximated by h_0. Then for non-cavitation cases where $\theta = 0$, one gets

$$\frac{\partial}{\partial x}\left({h_0}^3 \frac{\partial p}{\partial x}\right) + \frac{\partial}{\partial y}\left({h_0}^3 \frac{\partial p}{\partial y}\right) = 12\,\eta\, u_m \frac{\partial h}{\partial x} \qquad (4)$$

A first-order pressure approximation can be written as $p = p_0 + \epsilon\, p_1$. The solution p_0 is easily obtained because for smooth parallel surfaces, the pressure is constant everywhere and equal to the boundary pressure. Introduction of the perturbed film thickness and pressure into Eq.(4) results in:

$$\epsilon\left(\frac{\partial^2 p_1}{\partial x^2} + \frac{\partial^2 p_1}{\partial y^2}\right) = \frac{-12\,\eta\, u_m}{{h_0}^3}\frac{\partial h_s}{\partial x} \qquad (5)$$

We analyse the effect of a sinusoidal surface roughness, described as:

$$h_s(x,y) = Amp\ sin\left(\frac{2\pi}{\lambda_x}x + \varphi_x\right)sin\left(\frac{2\pi}{\lambda_y}y + \varphi_y\right) \qquad (6)$$

where Amp is the roughness amplitude; λ_x (λ_y) is the wavelength; φ_x (φ_y) is the phase.

One defines the perturbation parameter $\epsilon = Amp/h_0$. Eq.(5) is then transformed into

$$\frac{\partial^2 p_1}{\partial x^2} + \frac{\partial^2 p_1}{\partial y^2} = \frac{-24\pi\,\eta\, u_m}{\lambda_x h_0^2}\ cos\left(\frac{2\pi}{\lambda_x}x + \varphi_x\right)sin\left(\frac{2\pi}{\lambda_y}y + \varphi_y\right) \qquad (7)$$

$$p_1 = \frac{6}{\pi}\frac{\lambda_x}{1 + (\lambda_x/\lambda_y)^2}\frac{\eta\, u_m}{{h_0}^2} sin\left(\frac{2\pi}{\lambda_x}x + \varphi_x + \frac{\pi}{2}\right) sin\left(\frac{2\pi}{\lambda_y}y + \varphi_y\right) \qquad (8)$$

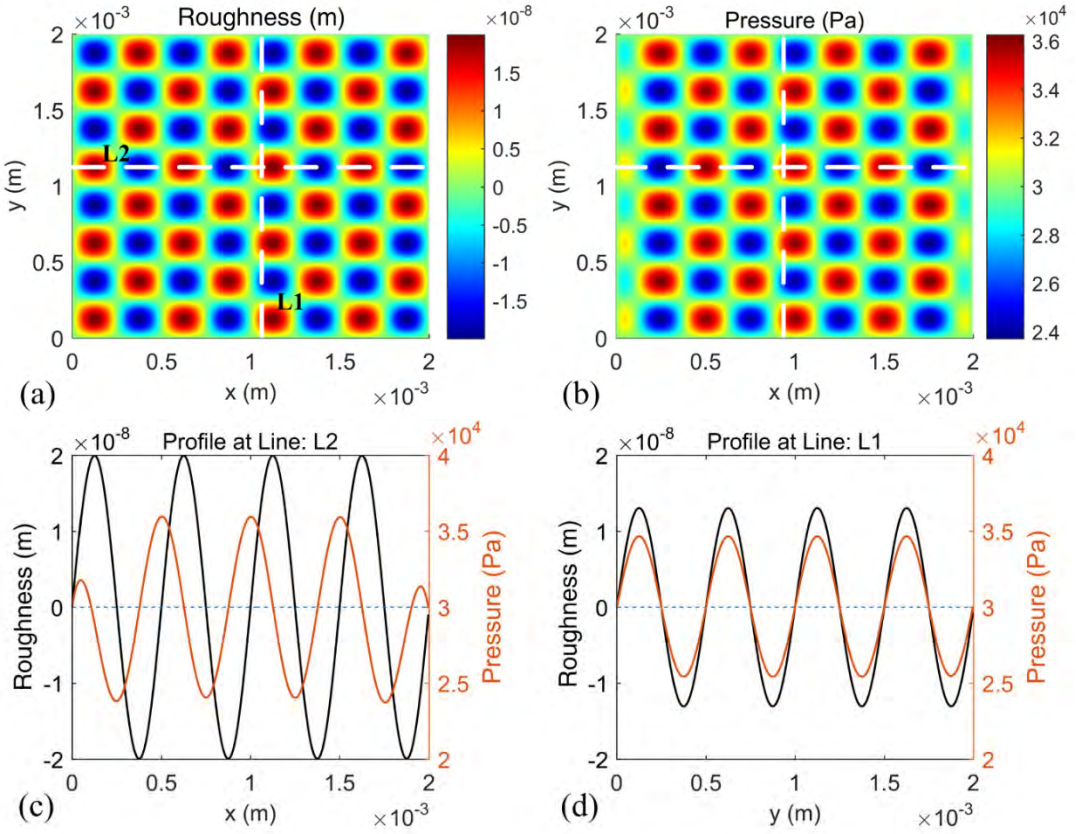

Figure 2: (a) A sinusoidal surface roughness, (b) numerical pressure solution, (c) p(x, y=1.1× 10^{-3} m) and (d) p(x = 1.1 × 10^{-3} m, y), surface in black and pressure in red.

So, the approximate pressure solution, $p = p_0 + \epsilon\, p_1$, *is*

$$p = dpm\, sin(\frac{2\pi}{\lambda_x}x + \varphi_x + \frac{\pi}{2})sin(\frac{2\pi}{\lambda_y}y + \varphi_y) + p_0 \qquad (9)$$

with the pressure amplitude being

$$dpm = \frac{6}{\pi}\frac{\lambda_x}{1+(\lambda_x/\lambda_y)^2}\frac{\eta\, u_m Amp}{{h_0}^3} \qquad (10)$$

Eq.(9) also indicates that the predicted LCC of a sinusoidal surface is 0. Eq.(10) reveals that whether cavitation occurs is dependent not only on h_0 and rms_h (=Amp/2 for a sinusoidal surface) but also on the surface wavelength and the operating conditions (the lubricant viscosity and mean surface velocity). If $dpm < p_0$, there is no cavitation.

4.2. Verification of the approximate solution

For an isotropic sinusoidal roughness ($\lambda_y = \lambda_x$), the pressure amplitude is

$$dpm_x = \frac{3}{\pi}\frac{\eta\, u_m\, \lambda_x\, Amp}{{h_0}^3} \qquad (11)$$

We numerically solved the pressure of isotropic sinusoidal surfaces under the conditions of $1.5 \le h_0 \le 2.5$ [μm], $0.01 \le Amp \le 0.1$ [μm], $2 \le L_x/\lambda_x \le 30$. The operating conditions are the same as in Table 1. The surface size is $L_x \times L_y$=2 mm × 2 mm. The calculations were performed on a grid with 1024 ×1024 points. Figure 3 shows that the pressure amplitude is indeed linear in the term $\lambda_x\, Amp/{h_0}^3$ and Eq.(11) gives a good fit with an R-square of 0.998.

Figure 3: Pressure amplitude as a function of Amp, λ_x and h_0.

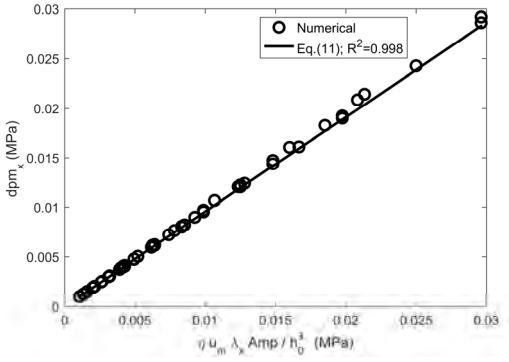

With Eqs.(10,11), one gets

$$dpm/dpm_x = \frac{2}{1+(\lambda_x/\lambda_y)^2} \qquad (12)$$

Numerical calculations were performed for $5 \le L_x/\lambda_x \le 20$, $0.1 \le \lambda_x/\lambda_y \le 10$, $20 \le h_0/Amp \le 40$.

Figure 4 shows a decreasing trend of dpm/dpm_x with λ_x/λ_y and the relationship is very well fitted by Eq.(12).

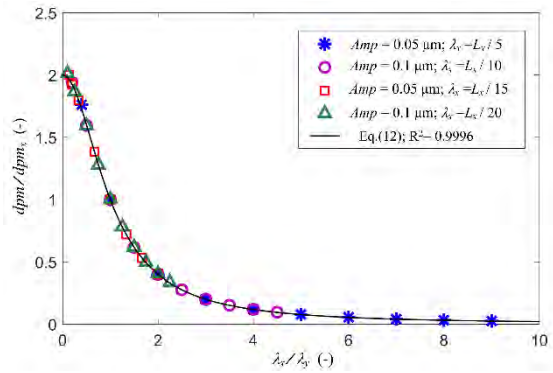

Figure 4: dpm/dpm_x as a function of λ_x/λ_y.

4.3. Pressure prediction with FFT techniques

According to Fourier analysis, a general surface can be represented by the sum of simple sine waves. Since the perturbed Reynolds equation (5) is linear, the solution consists of a sum of sinusoidal pressure components.

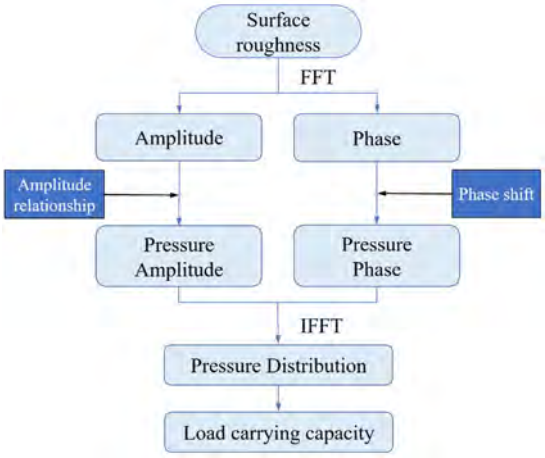

Figure 5: Flow chart of the FFT-based pressure prediction.

We use FFT techniques to predict the hydrodynamic pressure of measured or artificially generated surfaces. The flow chart of this method is shown in Figure 5.

Please note that 'Amplitude relationship' refers to Eq.(10). A phase shift of $\pi/2$ in the x direction is used for 'Phase shift'. This procedure can be easily implemented using MATLAB software [38]. The details are given in the Appendix.

4.4. Results

We use random surfaces to study the pressure and LCC for hydrodynamic lubrication of parallel surfaces, which can represent seals, parallel bearings or PRCL contacts.

These surfaces were generated with a Gaussian height distribution and an exponential autocorrelation function according to the algorithm outlined by Patir [39]. Here, all the generated surfaces have the same correlation length cl=0.2 mm (decaying to 10%) in both the x and y directions and are periodical with a period of [0, L_x] in the x direction and [0, L_y] in the y direction.

Figure 6 shows such a surface roughness and its power spectral density (PSD).

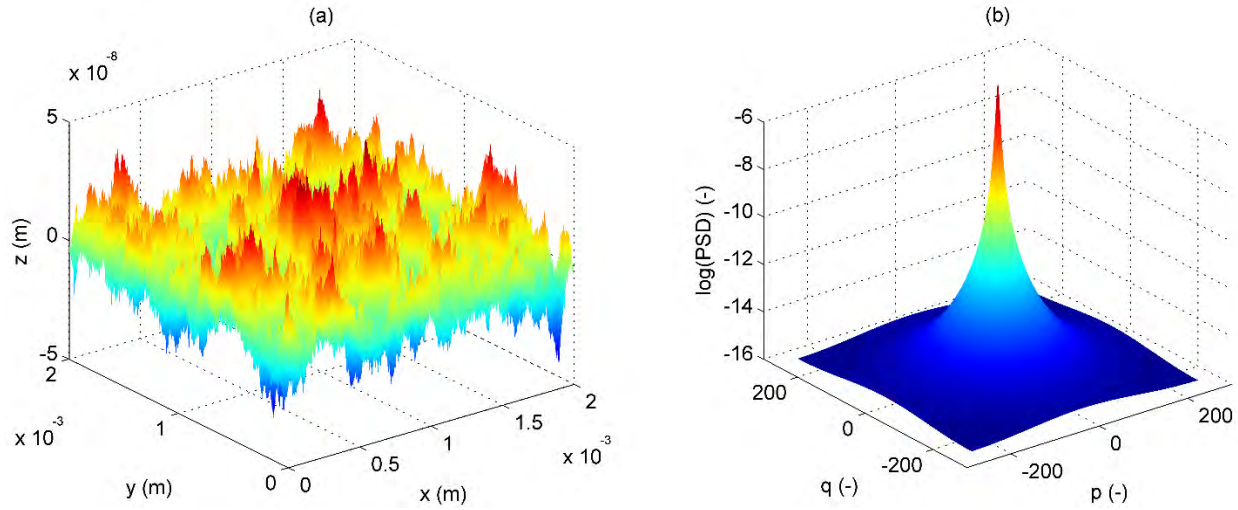

Figure 6: (a)Artificially generated random rough surface and (b) power spectral density

The 2-dimensional (2-D) PSD is defined according to [40] as:

$$PSD(p,q) = |c_{p,q}|^2 (N_x N_y)^2 / (L_x L_y) \qquad (13)$$

The domain $L_x \times L_y$ is 2 mm × 2 mm. The RMS roughness rms_h is 0.01 μm. h_0 is equal to 2 μm and the values of η, u_m and p_0 are listed in Table 1. These parameters ensure that no cavitation occurs.

The wavelengths of the sinusoidal components from the Fourier decomposition are most likely to be smaller than the correlation length of the surface. Using the parameter values λ_x=cl=0.2 mm, Amp=0.05 μm and h_0=2 μm in Eq.(11), the calculation result is dpm_x=6250 Pa, much smaller than p_0 (=30000 Pa).

We both predicted and numerically solved the pressure with the same finest discretization of $N_x \times N_y = 1024 \times 1024$ points. The pressure results are shown in Figure 7.

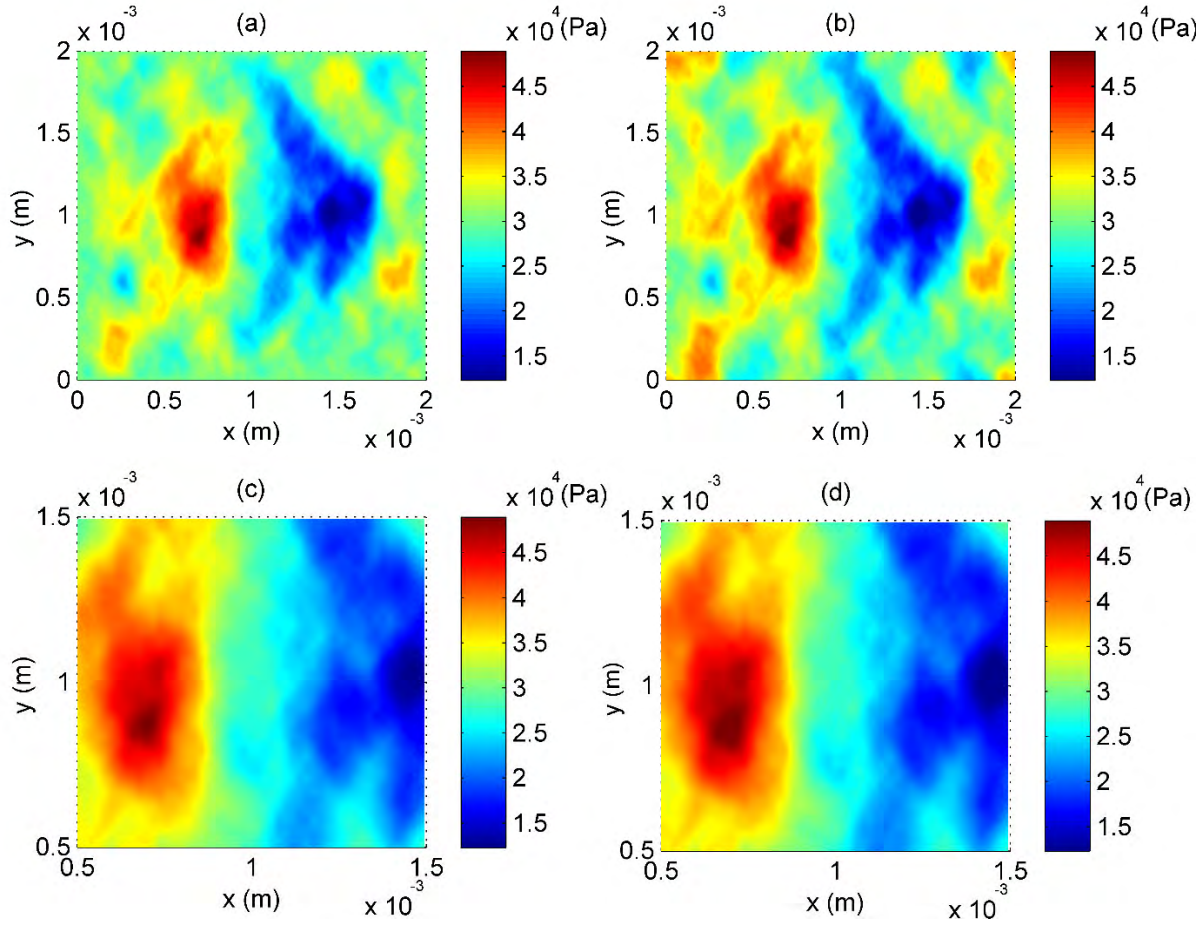

Figure 7: Top-view of the pressure distribution of the generated rough surface: (a) numerical, (b) FFT-prediction, (c) numerical result in the central domain and (d) FFT prediction in the central domain

.

Once again, it is found that the predicted pressure distribution near the boundaries differs substantially from the numerical result, but the central pressure distribution results are very close. The numerical average pressure is $LCC\ /(0.25L_x\ L_y)$ = -578 Pa. The relative error of the LCC over the central domain is about 5%. This shows that the FFT method cannot predict the LCC over the total domain but can predict the LCC over the central area accurately. The time consumption of the numerical calculation and the FFT-based prediction are respectively 346 s and 0.7 s. So, we obtained a time saving of roughly 500× with the FFT method.

Additionally, we conducted a comparison of the numerical solution and FFT-based prediction for 10 generated random surfaces under the same parameter conditions.

The results are presented in Figure 8. It shows that for all the calculations, the relative error of the LCC over the central domain is smaller than 8%. Furthermore, the LCC is randomly positive or negative. Generally, for parallel surfaces, no cavitation leads to no load carrying capacity [28], which means that theoretically, the LCC should be 0.

The average LCC over the central domain of 10 random surfaces is -990 Pa. Those of 40 surfaces and 90 surfaces are respectively -520 Pa and -360 Pa. According to the "Law of large numbers", the average LCC ratio of 40 to 10 surfaces should be 1/2 and that of 90 to 10 surfaces 1/3. It can be seen that the numerical ratios are close. This shows that the average LCC of a large sample tends to 0, which is in accordance with observations from [28]. It should be noted that the FFT mean pressure prediction over the total domain is zero by definition (Eq.(9)).

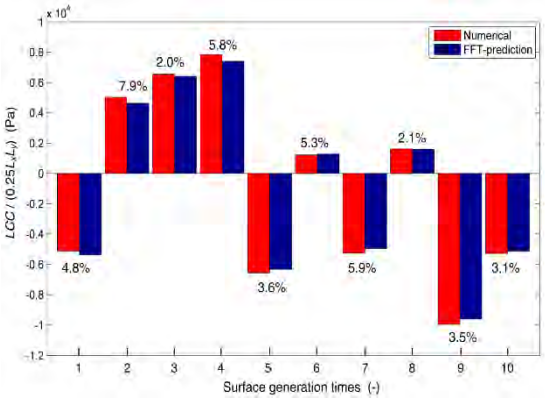

Figure 8: Comparison of numerical and FFT-predicted mean pressure over the central domain for 10 generated random surfaces with rms_h=0.01 μm , cl=0.2 mm and $L_x \times L_y$=2 mm×2 mm.

5. Discussion

5.1. Influence of the cavitation pressure

Figure 9 shows the calculated pressure distributions of the measured surface "MLJ" (Figure 1(a)) for different cavitation pressures p_c. The boundary pressure p_0 is the difference between the ambient pressure (p_a) and the cavitation pressures (p_c). One assumes p_a is 100 kPa. So from (a) to (f), p_0 takes the values of 0, 5, 10, 15, 20, 30 [kPa].

As a result, the cavitation area covers 49.0%, 13.5%, 4.6%, 1.0%, 0.07%, 0.0% and the mean pressure $LCC\ /(0.25L_x\ L_y)$ is 0.9, -1.7, 0.2, 3.5, 5.3, 5.4 [kPa].

One finds that the cavitation area decreases with the decrease of the cavitation pressure. When cavitation is severe, the LCC is very small and even negative. As p_c gets smaller than 85 kPa, no cavitation occurs and the LCC is constant.

5.2. Application to non-Gaussian roughness

The prediction method is not limited to Gaussian roughness or periodic surfaces.

Figure 10 shows the comparison between the predicted pressure and the numerical result (the same as Figure 1(b)). The "MLJ" surface is measured and neither Gaussian nor periodic

It can be seen that the pressure difference near the boundaries is relatively large, as the Dirichlet condition $p = p_0$ makes the problem non-periodic. Neglecting the pressure near the boundaries, it is found that the predicted pressure distribution is similar to the numerical one. The relative error of the LCC over the central area is 8.0% and a time saving of 500× is obtained with the FFT-based method.

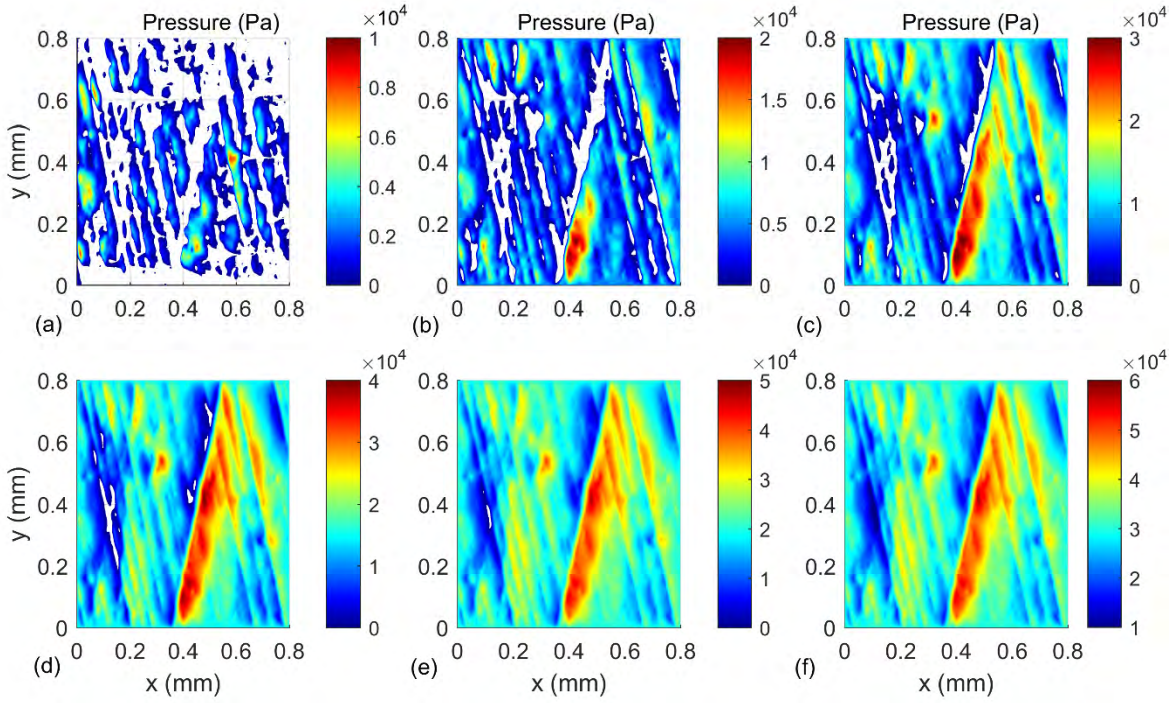

Figure 9: Top view of the pressure distribution of the "MLJ" surface for different cavitation pressure p_c: 100, 95, 90, 85, 80, 70 [kPa] from (a) to (f). h_0=2 µm other conditions as in Table 1. please note the different color bars for top and bottom rows.

.

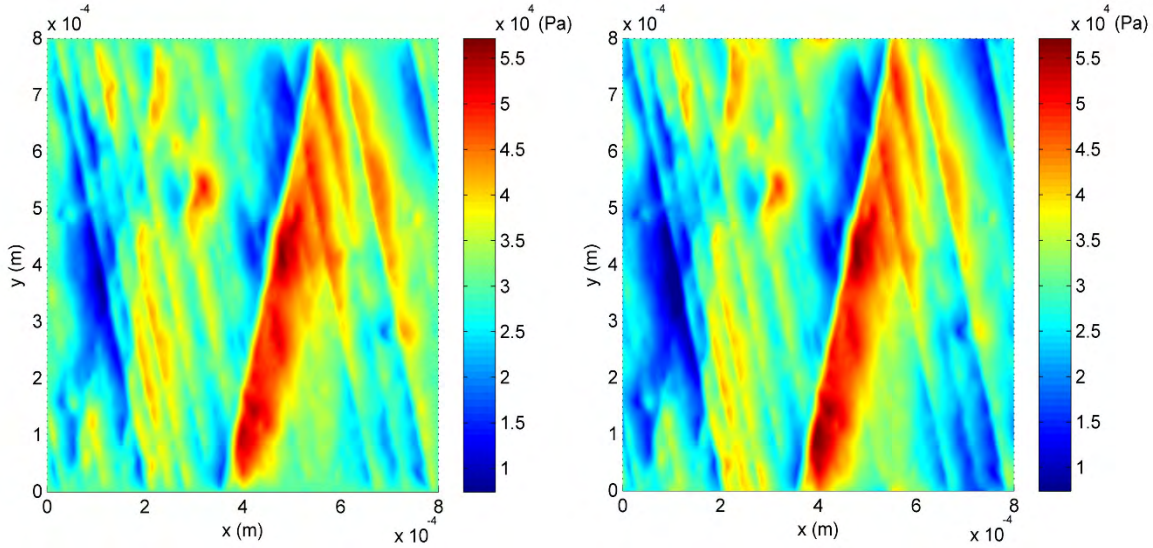

Figure 10: Top-view of the pressure distribution of the measured "MLJ" topography: numerical (left) and FFT-prediction (right).

5.3. Accuracy of the prediction method

The prediction method is based on two assumptions: $rms\_h/h_0 \ll 1$ and no cavitation. Figure 11 shows the variation of the prediction accuracy with the ratio rms_h/h_0. The LCC error refers to the error of the mean pressure LCC /($0.25L_x\ L_y$). The pressure error is defined as the ratio RMS((pressure difference))/Mean(pressure) over the central domain. We used the same random roughness to obtain the surfaces by only changing the rms_h value. One finds that the pressure error increases with the ratio rms_h/h_0. The error is 2.3% at rms_h/h_0=0.01. The LCC error shows a more complicated trend but it remains smaller than 8% for

$rms\_h/h_0 \leq 0.01$. When the ratio is larger than 0.01, cavitation occurs and both the pressure and LCC errors rise rapidly. However, the critical value of rms_h/h_0 depends on other operating conditions, i.e. the cavitation pressure.

According to the analysis in Section 5.1, one knows that a larger p_c is more likely to result in cavitation which makes the prediction method less accurate. Consequently, the critical value of rms_h/h_0 may be smaller than 0.01.

The numerical results show that in non-cavitation cases, the LCC is almost constant in p_c (p_0). The predicted LCC depends on other operating conditions and the surface feature. So, the cavitation pressure, p_c, does not influence the accuracy when there is no cavitation.

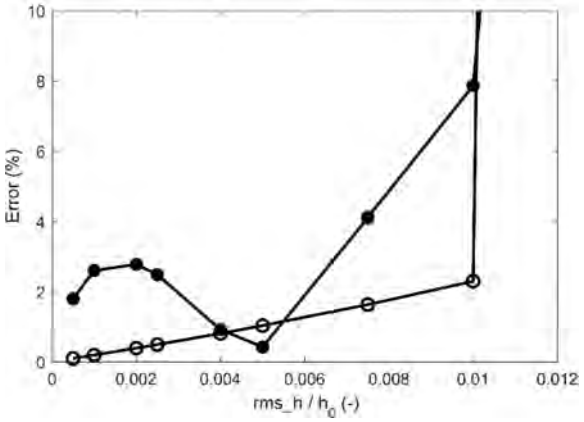

Figure 11: Error between predicted and numerical results as a function of rms_h/h_0: LCC in closed dots and pressure in open dots. h_0=2 μm other conditions as in Table 1.

6. Conclusions

The current paper studies the hydrodynamic pressure and LCC of parallel surfaces, which can be piston ring-cylinder liner contacts, rotatory-shaft seals or parallel bearings. Reference solutions are generated using an existing solver.

For non-cavitating cases where the problem becomes approximately linear, an efficient pressure-prediction method is proposed, using FFT techniques.

This prediction is based on a perturbation solution of the non-cavitation hydrodynamic lubrication of stationary sinusoidal surfaces with a moving smooth surface. Neglecting the pressure near the boundaries, the pressure distribution is sinusoidal as well. A linear relationship is found between the pressure amplitude of isotropic sinusoidal surfaces and the term $Amp\ \lambda_x/{h_0}^3$. Subsequently, the hydrodynamic pressure in the centre of anisotropic sinusoidal surfaces can be predicted using the obtained relationship between the pressure amplitude ratio (dpm/dpm_x) and the wavelength ratio (λ_x/λ_y).

Good agreement is found between the numerical solution and the FFT-based prediction of the central hydrodynamic pressure and central LCC for the measured surface topography and artificial surfaces with random roughness. The FFT prediction method results in a 500× time saving.

The LCC of an artificially generated random surface can be positive or negative, depending on the precise roughness features. The average LCC of a large sample of random surfaces is 0.

The ratio of h_0 and rms_h determines the level of cavitation, when the waviness feature of the surface and the operating conditions (the lubricant viscosity and mean surface velocity) are constant. When the ratio is large, no cavitation occurs. A significant increase in the local pressure (built up behind the valleys) is found for a cavitating case, compared to a non-cavitation case.

So far, the FFT-based method could not successfully predict the hydrodynamic pressure with cavitation. Future work will study the prediction of the pressure distribution with severe cavitation.

6.1. Acknowledgements

This paper is sponsored by the National Natural Science Foundation of China (Grant No.51805232 & 51605209), the Natural Science Foundation of the Jiangsu Higher Education Institutions of China (Grant No.18KJB460011) and the Natural Science Foundation of Jiangsu Normal University (Grant No.16XLR019).

The authors would like to thank Dr. Tomanik for kindly providing the measured "MLJ" surface topography.

7. References

[1] **Hamilton DB, Walowit JA, Allen CM.** A theory of lubrication by micro- irregularities. J Fluids Eng 1966; 88: 177-185.

[2] **Harp SR, Salant RF.** An average flow model of rough surface lubrication with inter-asperity cavitation. J Tribol 2001; 123: 134-143.

[3] **Harp SR, Salant RF.** Inter-asperity cavitation and global cavitation in seals: an average flow analysis.Tribol Int 2002; 35: 113-121.

[4] **Stakenborg MJL.** On the sealing mechanism of partial lip seals. Tribol Int 1988; 21: 335-340.

[5] **Qiu Y, Khonsari MM.** Experimental investigation of tribological performance of laser textured stainless steel rings. Tribol Int 2011; 44: 635-644.

[6] **Zhang J, Meng Y.** Direct observation of cavitation phenomenon and hydro-dynamic lubrication analysis of textured surfaces. Tribol Lett 2012; 46: 147-158.

[7] **Lebeck AO.** Parallel sliding load support in the mixed friction regime: Part II-Evaluation of the mechanisms. J Tribol 1987; 109: 196-205.

[8] **Shi F, Salant RF.** Numerical study of a rotary lip seal with a quasi-random sealing surfaces. J Tribo 2001; 123(3): 517-524.

[9] **Gropper D, Wang L, Harvey TJ.** Hydrodynamic lubrication of textured surfaces: A review of modeling techniques and key findings. Tribol Int 2016; 94: 509-529.

[10] **Ausas RF, Ragot P, Leiva J, Jai M, Bayada G, Buscaglia GC.** The impact of the cavitation model in the analysis of microtextured lubricated journal bearings. J Tribol 2007; 129: 868-75.

[11] **Qiu Y, Khonsari MM.** On the prediction of cavitation in dimples using a mass-conservative algorithm. J Tribol 2009; 131(11): 041702.

[12] **Gherca AR, Maspeyrot P, Hajjam M, Fatu A.** Influence of texture geometry on the hydrodynamic performances of parallel bearings. Tribol Trans 2013; 56(3): 321-332.

[13] **Sharma SC, Yadav SK.** Performance analysis of a fully textured hybrid circular thrust pad bearing system operating with non-Newtonian lubricant. Tribol Int 2014; 77: 50-64.

[14] **Kumar V, Sharma SC.** Influence of dimple geometry and micro-roughness orientation on performance of textured hybrid thrust pad bearing. Meccanica 2018; 53(14): 3579-3606.

[15] **Han Y, Fu Y.** Investigation of surface texture influence on hydrodynamic performance of parallel slider bearing under transient condition. Meccanica 2018; 53(8): 2053-2066.

[16] **Feng HH, Peng LP.** Numerical analysis of water-lubricated thrust bearing with groove texture considering turbulence and cavitation. Ind Lubr Tribol 2018; 70(6): 1127-1136.

[17] **Adjemout M, Brunetiere N, Bouyer J.** Numerical analysis of the texture effect on the hydrodynamic performance of a mechanical seal. Surf Topogr -Metrol Prop 2016; 4(1): 014002.

[18] **Xue B, Wei C, Hu JB.** Study of separation characteristics of micro-groove rotary seal considering different cavitation boundary conditions. Tribol Lett 2017; 65(4): 119.

[19] **Xue B, Wei C, Hu JB, Zhao YM.** Research on effects of groove shape optimization on cavitation and lubricating characteristics for microgroove rotary seal. Tribol Trans 2018; 61(3): 569-584.

[20] **Hao MM, Wang YL, Li ZT, Sun XH.** Effects of surface topography on hydrodynamic performance of liquid film seals considering cavitation. Ind Lubr Tribol 2018; 70(6): 984-992.

[21] **Tomanik E, Profito F, Zachariadis D.** Modelling the hydrodynamic support of cylinder bore and piston rings with laser textured surfaces. Tribol Int 2013; 59: 90-6.

[22] **Ausas RF, Jai M, Ciuperca I, Buscaglia GC.** Conservative one-dimensional finite volume discretization of a new cavitation model for piston–ring lubrication. Tribol Int 2013; 57: 54-66.

[23] **Profito F, Vladescu S, Reddyhoff T, Dini D.** Transient experimental and modelling studies of laser-textured microgrooved surfaces with a focus on piston-ring cylinder liner contacts. Tribol Int 2017; 113: 125-36.

[24] **Yin BF, Sun S, Wang BW, Qian YQ.** Numerical research on tribological performance of textured liner surface under different combustion modes. J Eng Gas Turbines Power 2017. 139(1): 011504.

[25] **Willis E.** Surface finish in relation to cylinder liners. Wear 1986; 109: 351-66.

[26] **Tomanik E, Mansori ME, Souza R, Profito F.** Effect of waviness and roughness on cylinder liner friction. Tribol Int 2018; 120: 547-555.

[27] **Yin BF, Xu B, Jia HK, Zhou HQ, Fu YH, Hua XJ.** Effects of the array modes of laser-textured micro-dimples on the tribological performance of cylinder liner-piston ring. Proc Inst Mech Eng Part J -J Eng Tribol 2018; 232(7): 871-881.

[28] **Noutary M-P, Biboulet N, Lubrecht AA.** Dimple influence on load carrying capacity of parallel surfaces. Tribol Int 2018; Doi: 10.1016/j.triboint.2018.10.033.

[29] **Vladescu SC, Ciniero A, Tufail K, Gangopadhyay A, Reddyhoff T.** Looking into a laser textured piston ring-liner contact. Tribol Int 2017; 115: 140-53.

[30] **Woloszynski T, Podsiadlo P, Stachowiak GW.** Efficient solution to the cavitation problem in hydrodynamic lubrication. Tribol Lett 2015; 58: 18.

[31] **Ausas RF, Jai M, Buscaglia GC.** A mass-conserving algorithm for dynamical lubrication problems with cavitation. J Tribol 2009; 131(3): 031702.

[32] **Bertocchi L, Dini D, Giacopini M, Fowell MT, Baldini A.** Fluid film lubrication in the presence of cavitation: a mass-conserving two-dimensional formulation for compressible, piezoviscous and non-Newtonian fluids. Tribol Int 2013; 67: 61-71.

[33] **Fesanghary M, Khonsari MM.** A modification of the switch function in the Elrod cavitation algorithm. J Tribol 2011; 133(2): 024501.

[34] **Biboulet N, Lubrecht AA.** Efficient solver implementation for Reynolds equation with mass-conserving cavitation. Tribol Int 2018; 118: 295-300.

[35] **Choy FK, Braun MJ, Hu Y.** Nonlinear effects in a plain journal bearing: Part 1 analytical study. J Tribol 1991; 113(3): 555-61.

[36] **Kim H, Jang G, Ha H.** A generalized Reynolds equation and its perturbation equations for fluid dynamic bearings with curved surfaces. Tribol Int 2012; 50: 6-12.

[37] **Patir N, Cheng HS.** Application of average flow model to lubrication between rough sliding surface. Journal of Lubrication Technology 1979; 101: 220-229.

[38] **Matlab R2013b (version 8.2).** The MathWorks Inc, Natick, MA, United States, 2013.

[39] **Patir N.** A numerical procedure for random generation of rough surfaces. Wear 1977; 47: 263-277.

[40] **Jacobs T, Junge T, Pastewka L.** Quantitative characterization of surface topography using spectral analysis. Surf Topogr: Metrol Prop 2017; 5: 013001.

8. Appendix

Implementation of the pressure prediction method in MATLAB software using the commands 'fft', 'ifft', 'angle' and 'abs':

$$c_{p,q} = fft(h_s(x,y))/(N_x\, N_y)$$

$$abs(c_{p,q}) = \begin{cases} Amp_{0,0} & p = 0, q = 0 \\ 0.5Amp_{p^+,q^+} & p = 0, q \neq 0 or p \neq 0, q = 0 \\ 0.25Amp_{p^+,q^+} & p \neq 0, q \neq 0 \end{cases}$$

$$angle(c_{p,q}) = sgn(p)(\varphi_{xp^+} - 0.5\pi) + sgn(q)(\varphi_{yq^+} - 0.5\pi)$$

where sgn(x) is the sign function.

$$\text{abs}(dpm_{p,q}) = \text{Fun}(q^+/p^+)\text{abs}(c_{p,q})\eta u_m L_x /(p^+ h_0^3), \qquad \lambda_x = L_x/p^+$$

$\text{angle}(dpm_{p,q}) = \text{angle}(c_{p,q})$ (with replacing φ_{xp^+} by $\varphi_{xp^+} + 0.5\pi$)

$$p(x,y) = ifft(dpm_{p,q})N_x\, N_y + p_0$$

Novel analytical and numerical calculations in truncated point contact: Single crown profile and no misalignment

L. Houpert

Bearing & Tribology Consultant, luc.houpert@orange.fr

Abstract - Novel relationships are given for calculating the contact load, tilting moment and pressure distribution along the roller as a function of the contact deformation and tilting angle for non-truncated or truncated point contacts described using single crown profiles. The analytical results have been calibrated versus some numerical results obtained using a cylinder on cylinder case and an advanced model and tool that account for pressure spikes. The final model is then successfully tested using two additional bearing types. When severe truncation occurs, the results tends asymptotically towards a newly line contact relationship, close to the Palmgren's one.

The same model is used in another described approach for calculating the load and pressure distribution, edge pressure, and tilting moment using any profile desired.

Key words - Hertzian point contact, truncated point contact, contact pressure, pressure spikes

List of symbols

a	half ellipse contact length (mm)
A_{geom}	geometrical half ellipse contact length (mm)
a^*	factor function of the elliptical integral E; see appendix
b	half ellipse contact width (mm)
b^*	factor function of the elliptical integral E; see appendix
CA	factor, curve fitted as a function of k and used for calculating a
CB	factor, curve fitted as a function of k and used for calculating b
CD	factor, curve fitted as a function of k and used for calculating δ
$Coef$	novel load correction factor curve fitted as a function of T
CP	factor, curve fitted as a function of k and used for calculating P_{max}
D	dimensionless deformation $=\frac{R_{x\_eq}.\delta}{L^2}$
D_0	dimensionless deformation at roller-race center $=\frac{R_{x\_eq}.\delta_0}{L^2}$
D_{max}	maximum dimensionless deformation when misalignment occurs $= D_0 + \frac{k.\theta^2.R_{x\_eq}^2}{2.L^2}$
E	elliptical integral; see appendix
E_1, E_2	Young's modulus of surface 1 and 2
E_{eq}	equivalent Young's modulus (MPa): $\frac{1}{E_{eq}} = \frac{1}{2}.\left(\frac{1-\upsilon_1^2}{E_1} + \frac{1-\upsilon_2^2}{E_2}\right)$
f_1, f_2 and f_3	miscellaneous factors curve fitted as a function of k only
F	elliptical integral; see appendix
k	ratio of equivalent radii = R_{y_eq}/R_{x_eq}
L	effective roller length (mm)
M	roller tilting moment around race center (N.mm)
P_{max}	maximum contact pressure (MPa)
Q	contact load (N)
r	ratio $A_{geom}/a = \frac{2.\sqrt{2}}{f_2}.\sqrt{k}$
x	rolling direction axis
y	axis tangent to the contact; abscissa of a slice, nil at race center (mm)
T	dimensionless truncation parameter $= \frac{2.a_{NT}}{L} = f_2.\sqrt{D}$
W	dimensionless load $= \frac{Q}{E_{eq}.R_{x\_eq}^2}$ used in point contact calculation

Greek symbols

κ	ratio a/b
δ	contact deformation at ellipse center or in a slice (mm)
δ^*	factor function of the elliptical integrals E and F; see appendix
δ_T	deformation corresponding to the transition point-to-line contact (mm)
δ_0	contact deformation at ellipse center (mm)
Δ	geometrical interference in a slice (mm)
Δ_0	geometrical interference at race center (at $y = 0$) (mm)
θ	relative roller-race tilt angle (rad)

Main index

NT	non-truncated
0	at race center when $y = 0$
pc	point contact
pc_trunc	truncated point contac

1. Objectives

A comprehensive survey of miscellaneous elastic calculations suggested by Houpert in concentrated contact has been presented but not really published in Ref. [1]. It can be seen in the "Proceedings of the 2018 Bearing World Conference" (PowerPoint presentation and three-page abstract Word document).

Among the models presented, a useful analytical relationship has been given for calculating (in a single crown truncated point contact) the contact load as a function of the roller-race deformation and misalignment. Analytical results have been tested and successfully validated against a few numerical results obtained using an advanced contact tool called *CST*, described by M. Hoeprich in Ref. [2].

At large loads, when truncation occurred, the analytical results were between 5% and 10% smaller than the numerical results; this accuracy was considered acceptable at the time for an engineering approach.

Since retiring in April 2018, the author has pursued this study and can now explain the slightly smaller loads observed when severe truncation occurs.

A correction factor can be introduced for matching numerical results precisely. These numerical results can be obtained using *CST* or any other advanced tool described by S. Cretu in Ref. [3].

Truncated point contact results obtained without misalignment will be presented using a few bearing type contact cases (cylindrical, spherical and tapered roller bearing).

A novel dimensionless analytical model will also be derived.

The objective of this paper is to publish the models and results presented in Ref. [1] and all these further enhancements which should help better modeling any gear or rolling element race contact.

2. Non-truncated Hertzian point contact calculations

Hertzian models are described in Ref. [4] (Harris and Kotzalas), Ref. [5] (Tripp) and in the appendix.

Point contacts between two surfaces are described by four curvatures ρ (inverse of radius). The contact dimensions (*a* and *b*), deformation δ and maximum pressure P_{max} can then be calculated as a function of the load *Q* and two elliptical integrals (*E* and *F*) functions of $\kappa = a/b$ (see the appendix). The ratio *k* can then be calculated as a function of κ and *F/E*. *k* is the equivalent radii ratio $(k = R_{y\_eq}/R_{x\_eq})$, where *x* is the rolling direction axis and *y* is the axis tangent to the contact ellipse. Iterations on κ are therefore required when imposing a fixed *k* ratio (considered by the designers as an input while *a/b* is an output).

These elliptical integrals must be calculated numerically and have been tabulated as a function of $F(\rho)$ defined in the appendix as a function of *k*. But they remain difficult to curve-fit as a function of $F(\rho)$.

Houpert demonstrated in Ref. [6] that it is easier to use *k* for directly calculating the contact parameters *a, b,* δ and P_{max} as a function of the dimensionless load *W,* R_{x_eq}, E_{eq} and some coefficients (*CA, CB, CD* and *CP*) only functions of *k* and easy to curve-fit:

$$W = \frac{Q}{E_{eq}.R_{x_eq}^2} \qquad \frac{a}{R_{x_eq}} = CA.W^{\frac{1}{3}}$$

$$\frac{b}{R_{x_eq}} = CB.W^{\frac{1}{3}} \qquad \frac{\delta}{R_{x_eq}} = CD.W^{\frac{2}{3}}$$

$$\frac{P_{max}}{E_{eq}^{\frac{1}{3}}} = CP.W^{\frac{1}{3}} \qquad (1)$$

These coefficients were initially curve-fitted in Ref. [6] using the tabulated results published by Dalmaz in Ref. [7] (found later to be identical to the ones published in Ref. [4]) and miscellaneous ranges of *k* (corresponding to ball bearings, spherical roller bearings and tapered roller bearings). The maximum value of *k* was limited to 13,576. Simple relationships with a constant factor *Cte1* and exponent *Cte2* defined for each parameter have been derived in Table 1 and each range — using, for example:

$$CA = Cte1 * k^{Cte2} \qquad (2)$$

	Rib contact		Ball race		Ball, SRB race		SRB, TRB race	
	k < 1		1 < k < 8.74		8.74 < k < 122.44		122.44 < k < 13576	
	Cte1	Cte2	Cte1	Cte2	Cte1	Cte2	Cte1	Cte2
a/R_{x_eq}	1.1521	0.52564	1.1552	0.4676	1.3085	0.4091	1.5528	0.3737
b/R_{x_eq}	1.2742	-0.0704	1.1502	-0.1876	1.1687	-0.1974	1.1063	-0.1866
δ/R_{x_eq}	1.4329	-0.086	1.3201	-0.1946	1.4586	-0.2414	1.7138	-0.2743
P_{max}/E_eq	0.3252	-0.4553	0.3593	-0.2799	0.3122	-0.2117	0.2779	-0.1871
$Q/(\pi abP_{max}/1.5)$	0.9999	-0.0001	0.9999	0.0001	0.9999	0.0000	0.9999	0.0000

Table 1: Initial curve fitted Hertzian results

It has been observed that minor discontinuities sometimes occur when transitioning from one range to the next range. To avoid such discontinuities, a more accurate curve-fitting to use in the full range of k (again limited to13,576) has been suggested by Houpert in Ref. [8]:

$$CA \approx 1.14471 * k^{5.0092E\text{-}01-\ 1.6389E\text{-}02*ln(k)+9.2220E\text{-}05*(ln(k))^2+1.3564E\text{-}04*(ln(k))^3\text{-}7.9909E\text{-}06*(ln(k))^4}$$
$$CB \approx 1.14471 * k^{-0.1663-0.015427*ln(k)+0.0031928*(ln(k))^2-0.00028026*(ln(k))^3+0.0000092392*(ln(k))^4}$$
$$CD \approx 1.310371 * k^{-0.16624-0.015265*ln(k)+0.00094795*(ln(k))^2-0.000024801*(ln(k))^3}$$
$$CP \approx 0.364371 * k^{-3.3456E\text{-}01+3.1754E\text{-}02*ln(k)-3.2652E\text{-}03*(ln(k))^2+1.4202E\text{-}04*(ln(k))^3-1.1314E\text{-}06*(ln(k))^4} \quad (3)$$

In this study, appropriate iterations and elliptical integral calculations (numerical or analytical when using Tripp's model) have been conducted for recalculating these coefficients (*CA, CB, CD and CP)* and three additional factors (f_1, f_2 and f_3, described later) in a wider range of k (k_{max} = 1.E7), see Table 2, Fig. 1 and the appendix. Maximum values of k found in cylindrical or needle roller bearings are generally around 15,000 but larger k values have been tested for confirming the f_1 drop at very large k values, as discussed later.

The elliptical integrals E and F especially have been calculated in the appendix using two steps: from $\psi = 0$ to 1.55 with 10,001 points, and from $\psi = 1.55$ to $\pi/2$, again with 10,001 points. Tripp's analytical solution can be recommended when k ≥ 3,000. The accuracy on all numerically calculated parameters (*CA, CB, CD, CP,* f_1, f_2 and f_3) obtained is then ≤ 1.10^{-9}.

Three useful factors f_1, f_2 and f_3 (explained next) have also been introduced:

$$f_1 = \frac{3}{4}.\frac{1}{CD.CA} \quad f_2 = \frac{2.CA}{\sqrt{CD}} \quad f_3 = \frac{1}{CD^{1.5}} \quad (4)$$

FINAL Proposal using two steps integration and Tripp's results when k > 3000

k	CA	CB	CP	CD	f1	f2	f3
1.00E+00	1.14471424	1.14471424	0.36437386	1.31037070	0.50000000	2.00000000	0.66666667
5.00E+00	2.46053706	0.85134358	0.22793269	0.96781720	0.31494739	5.00222517	1.05029184
1.00E+01	3.33986185	0.74228269	0.19259435	0.83322566	0.26950705	7.31774349	1.31478896
1.50E+01	3.97089212	0.68467792	0.17561717	0.75999140	0.24852180	9.10990283	1.50933965
2.00E+01	4.47978509	0.64655670	0.16484569	0.71072964	0.23555897	10.62759414	1.66895012
2.50E+01	4.91342257	0.61851121	0.15711212	0.67411249	0.22643564	11.96872603	1.80676406
5.00E+01	6.51084808	0.53937279	0.13596114	0.56937293	0.20231444	17.25715303	2.32758086
7.50E+01	7.65098079	0.49822729	0.12525549	0.51436526	0.19057789	21.33591598	2.71076928
1.00E+02	8.56832945	0.47112118	0.11828035	0.47805893	0.18309803	24.78480088	3.02536546
1.50E+02	10.03544718	0.43562375	0.10921772	0.43058469	0.17356652	30.58703869	3.53925718
2.00E+02	11.21529527	0.41221732	0.10327720	0.39941868	0.16742572	35.49167710	3.96147977
2.50E+02	12.21896450	0.39500829	0.09892380	0.37662196	0.16297509	39.82094651	4.32654813
3.00E+02	13.10133968	0.38152865	0.09552093	0.35885723	0.15952320	43.74061196	4.65176168
4.00E+02	14.61741123	0.36126617	0.09041565	0.33234251	0.15438493	50.71162320	5.21940687
5.00E+02	15.90668494	0.34635345	0.08666469	0.31300298	0.15063750	56.86374232	5.71054147
7.50E+02	18.53194145	0.32093108	0.08028024	0.28045362	0.14430431	69.98748602	6.73299723
1.00E+03	20.64104761	0.30411515	0.07606268	0.25926943	0.14014519	81.07483456	7.57483225
1.25E+03	22.43391678	0.29172286	0.07295681	0.24386336	0.13709121	90.85771703	8.30386271
1.50E+03	24.00922260	0.28199847	0.07052069	0.23190916	0.13469928	99.71239398	8.95412491
1.75E+03	25.42388151	0.27404636	0.06852917	0.22222892	0.13274520	107.86276927	9.54551016
2.00E+03	26.71409639	0.26735087	0.06685275	0.21414898	0.13110063	115.45492918	10.09080897
2.50E+03	29.01273490	0.25654714	0.06414836	0.20125597	0.12844695	129.34340063	11.07584397
3.00E+03	31.03197496	0.24806372	0.06202528	0.19126505	0.12636192	141.91281072	11.95491713
4.00E+03	34.49819571	0.23527614	0.05882570	0.17644312	0.12321403	164.25704841	13.49251507
5.00E+03	37.44302076	0.225837215	0.056464436	0.165699204	0.120884317	183.9673121	14.82584193
7.50E+03	43.43223094	0.209691781	0.052426135	0.147742567	0.116880883	225.9900473	17.60927753
1.00E+04	48.23784308	0.198974222	0.049745831	0.136139846	0.114205792	261.4720362	19.90774728
1.50E+04	55.90271418	0.184832185	0.04620946	0.121251917	0.110647029	321.0839401	23.684656
5.00E+04	86.38684272	0.148687643	0.037172255	0.085680874	0.101328071	590.2495361	39.8725647
1.00E+05	110.8118104	0.131282444	0.032820764	0.070013827	0.096669929	837.5758337	53.97893067
5.00E+05	196.8368809	0.098502499	0.024625648	0.043596129	0.08739908	1885.439089	109.8570946
1.00E+06	251.7627473	0.087097332	0.021774343	0.035485213	0.083950324	2672.992597	149.5990631
5.00E+06	444.6916228	0.065534682	0.016383672	0.021922461	0.07693306	6006.815447	308.0817944
1.00E+07	567.6039966	0.058006673	0.014501669	0.017791102	0.074269923	8510.871175	421.4011625

Table 2: Results obtained using the two-step integration process and Tripp's models when k > 3000

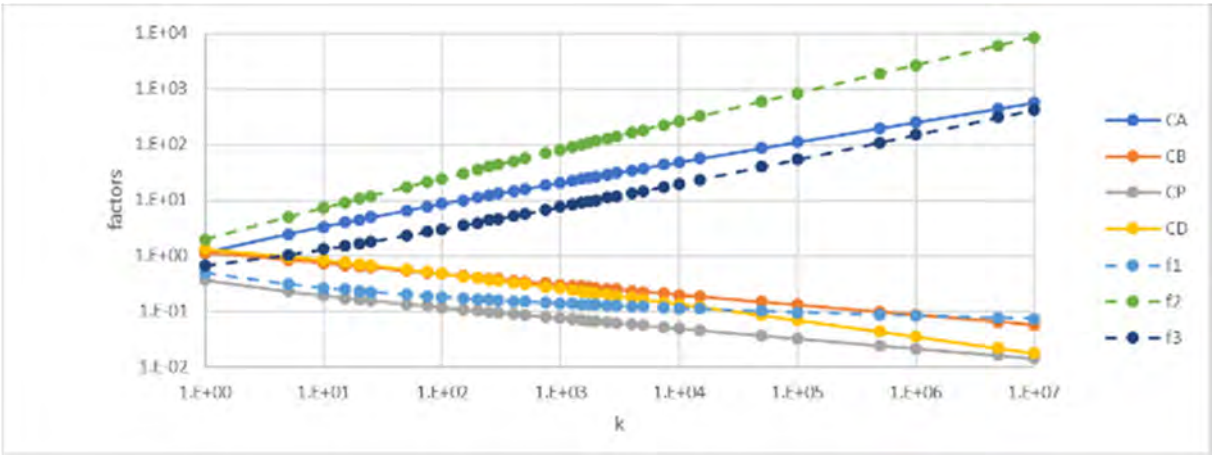

Fig. 1: Results obtained using the two-step integration process and Tripp's models when k > 3000

Note that the decrease of f_1 versus k at very large k ratios is confirmed and will be used later for defining the product $f_1.f_2^{0.18}$ and Q_{lc_CST} (also defined later) at very large k ratios.

Last, but not least, appropriate curved-fitted relationships must be suggested for calculating all Hertzian factors *CA, CB, CP, CD, f_1, f_2* and f_3 (called V next) as a function of k using the following curve fitting model:

$$V = V_{k=1} * k^{Y}$$

$$Y = \frac{ln(\frac{V}{V_{k=1}})}{ln(k)}$$

$$X = ln(k)$$

$$Y_{cf} = a0 + a_1.X + a_2.X^2 + a_3.X^3 + a_4.X^4 + a_5.X^5 + a_6.X^6$$

$$V_{cf} = V_{k=1} * k^{a_0+a_1.X+a_2.X^2+a_3.X^3+a_4.X^4+a_5.X^5+a_6.X^6} \quad (5)$$

The exponent Y can be defined for any k ratio and curve fitted as a function of X using a polynomial regression of Degree 6.

The results obtained and accuracy obtained are shown in Table 3:

$X = \ln(k)$

$V_{cf} = V_{k=1} * k^{a_6.X^6+a_5.X^5+a_4.X^4+a_3.X^3+a_2.X^2+a_1.X+a_0}$

FINAL Proposal using two steps integration and Tripp's models when k > 3000

kmax = 1.00E+07

	V_k=1	a6	a5	a4	a3	a2	a1	a0	ABS(error)_max
CA	1.1447E+00	-1.7054E-08	9.2012E-07	-1.8076E-05	1.2668E-04	6.6073E-04	-1.8774E-02	5.0359E-01	8.76E-04
CB	1.1447E+00	2.1284E-08	-1.3952E-06	3.7742E-05	-5.4190E-04	4.3627E-03	-1.7831E-02	-1.6456E-01	4.41E-04
CP	3.6437E-01	-4.2305E-09	4.7513E-07	-1.9666E-05	4.1523E-04	-5.0234E-03	3.6605E-02	-3.3903E-01	4.34E-04
CD	1.3104E+00	-5.4492E-09	2.7437E-07	-4.3875E-06	-2.3270E-06	9.8797E-04	-1.5832E-02	-1.6530E-01	3.07E-04
f1	5.0000E-01	2.2503E-08	-1.1945E-06	2.2464E-05	-1.2435E-04	-1.6487E-03	3.4605E-02	-3.3829E-01	1.18E-03
f2	2.0000E+00	-1.4329E-08	7.8294E-07	-1.5882E-05	1.2784E-04	1.6675E-04	-1.0858E-02	5.8625E-01	7.22E-04
f3	6.6667E-01	8.1738E-09	-4.1156E-07	6.5813E-06	3.4905E-06	-1.4820E-03	2.3747E-02	2.4796E-01	4.61E-04

Table 3: Curve-fitted results obtained using the very large k range (k_{max} = 1.E7).

Using the numerical results as reference, the relative error of the curve-fitted results can be defined as $ABS(V_{cf} - V_{Num})/V_{Num}$ and is smaller than 1.182E-3

The accuracy of the curve-fitted results can be improved (relative error < 6.49E-5) when limiting the maximum value of k to 15,000 found when studying real bearing cases, cylindrical or needle roller bearing for example.

$X = \ln(k)$

$V_{cf} = V_{k=1} * k^{a_6.X^6 + a_5.X^5 + a_4.X^4 + a_3.X^3 + a_2.X^2 + a_1.X + a_0}$

FINAL Proposal using two steps integration and Tripp's models when k > 3000

kmax = 1.50E+04

	V_k=1	a6	a5	a4	a3	a2	a1	a0	ABS(error)_max
CA	1.1447E+00	-1.4367E-07	5.6673E-06	-8.8850E-05	6.5751E-04	-1.4211E-03	-1.4797E-02	5.0075E-01	4.07E-05
CB	1.1447E+00	3.3911E-11	-7.4826E-07	3.0316E-05	-5.0229E-04	4.2662E-03	-1.7748E-02	-1.6456E-01	2.41E-05
CP	3.6437E-01	1.4364E-07	-4.9190E-06	5.8534E-05	-1.5523E-04	-2.8451E-03	3.2545E-02	-3.3619E-01	6.49E-05
CD	1.3104E+00	-4.9945E-08	1.9428E-06	-2.9265E-05	1.8428E-04	2.5604E-04	-1.4433E-02	-1.6630E-01	1.45E-05
f1	5.0000E-01	1.9362E-07	-7.6101E-06	1.1812E-04	-8.4180E-04	1.1651E-03	2.9230E-02	-3.3445E-01	5.53E-05
f2	2.0000E+00	-1.1870E-07	4.6959E-06	-7.4218E-05	5.6537E-04	-1.5492E-03	-7.5801E-03	5.8391E-01	3.35E-05
f3	6.6667E-01	7.4918E-08	-2.9143E-06	4.3898E-05	-2.7642E-04	-3.8406E-04	2.1650E-02	2.4946E-01	2.17E-05

Table 4: Curve-fitted results obtained when limiting k to 15,000.

Finally, in a non-truncated point contact (index *NT*), the point contact load and contact ellipse half-length dimensions can be defined as a function of the maximum deformation δ_{max} using the factor f_3 and f_2:

$$Q_{pc} = Q_{NT} = \frac{E_{eq}.\sqrt{R_{x\_eq}}}{CD^{1.5}}.\delta_{\max}^{1.5} = f_3.E_{eq}.\sqrt{R_x}.\delta_{\max}^{1.5} = K_{PC}.\delta_{\max}^{1.5} \quad (6)$$

$$a_{NT} = CA.R_{x\_eq}.\left(\frac{Q_{NT}}{E_{eq}.R_{x\_eq}^2}\right)^{\frac{1}{3}} = \frac{CA}{\sqrt{CD}}.\sqrt{R_{x\_eq}.\delta_{\max}} = \frac{f_2}{2}.\sqrt{R_{x\_eq}.\delta_{\max}}$$

$$b_{NT} = CB.R_{x\_eq}.\left(\frac{Q_{NT}}{E_{eq}.R_{x\_eq}^2}\right)^{\frac{1}{3}} = \frac{CB}{\sqrt{CD}}.\sqrt{R_{x\_eq}.\delta_{\max}}$$

where δ_{max} is the deformation at the contact ellipse center and the coefficients f_2 and f_3 have been curve-fitted as a function of k.

3. Truncated point contact

Before studying truncated contact, let's remind that when no truncation occurs, the load dQ in the slice (of width dy) located at the contact center (where P_{max} and the maximum deformation δ_{max} are found) can be calculated by extending the logic described in Ref. [9]. The y axis is tangent to the contact, going from left to right and the factor f_1 is used for calculating dQ as a function of δ_{max}:

(7)

$$P_{\max} = \frac{CP}{\sqrt{CD}}.E_{eq}.\sqrt{\frac{\delta_{\max}}{R_{x\_eq}}} \qquad b = \frac{CB}{\sqrt{CD}}.\sqrt{R_{x\_eq}.\delta_{\max}}$$

$$dQ_{\max} = \frac{\pi}{4}.P_{\max}.2.b.dy = \frac{\pi}{2}.E_{eq}.\frac{CP.CB}{CD}.\delta_{\max}.dy = E_{eq}.f_1.\delta_{\max}.dy \quad with \quad f_1 = \frac{\pi}{2}.\frac{CP.CB}{CD}$$

When using a single crown profile (i.e., a roller having an equivalent crown radius R_{y_eq} on a flat plane) and when no misalignment occurs, the maximum elastic deformation δ_{max} or δ_0 at the contact ellipse center (at $y = 0$) is equal to the maximum geometrical interference Δ_0 at the contact center.

The geometrical interference Δ along the roller-race contact can be calculated as a function of Δ_0 and θ, where θ is the relative roller-race misalignment. For example, at the roller-IR contact:

$$\Delta = \Delta_0 - \theta.y - \frac{y^2}{2.R_{y\_eq}} \quad (8)$$

A positive value of θ corresponds to an anti-clockwise rotation (tilt) of the roller.

When no misalignment occurs, the geometrical interference is nil at abscissa A_{geom}, always slightly larger than a_{NT}. A ratio r can be introduced for capturing the ratio A_{geom}/a_{NT}.

$$A_{geom} = \sqrt{2.R_{y_{eq}}.\Delta_0}$$

$$r = \frac{A_{geom}}{a_{NT}} = \frac{\sqrt{2.CD.k}}{CA} = \frac{2.\sqrt{2}}{f_2}.\sqrt{k} \quad (9)$$

For ensuring zero deformation at abscissa $y = a_{NT}$ (and not A_{geom}), the deformation δ at any abscissa y can be estimated using the product $(r.y)$ instead of y:

$$\delta = \Delta_0 - \theta.(r.y) - \frac{(r.y)^2}{2.R_{y\_eq}} \quad (10)$$

At $y = 0$: $\delta = \Delta_0 = \delta_0$; at $y = a_{NT}$: $\delta = 0$.

In a first or initial step, it is assumed that the load in any slice can be calculated using:

$$dQ = E_{eq}.f_1.\delta.dy \quad (11)$$

The latter load will be corrected later by a correction factor called *Coef*.

When using a roller of contact length L, one can define the left- and right-side abscissa of the contact using:

$$y_{1end} = max\left[\frac{R_y.\left(-\theta - \sqrt{\theta^2 + 2.\frac{\Delta_0}{R_{y\_eq}}}\right)}{r}; -\frac{L}{2}\right]$$

$$y_{2end} = min\left[\frac{R_y.\left(-\theta + \sqrt{\theta^2 + 2.\frac{\Delta_0}{R_{y\_eq}}}\right)}{r}; \frac{L}{2}\right] \quad (12)$$

Truncation occurs when $\pm L/2$ defines the contact boundaries.

Since the load dQ versus δ relationship is linear, and because δ versus y is a polynomial degree 2 relationship (when single crown profile is used), it is easy to analytically integrate dQ along the y axis for obtaining the load corresponding to truncated or non-truncated contact:

$$Q_{pc\_trunc} = \underbrace{E_{eq}.f_1.k^{-0.1}}_{\approx 0.282 * E_{eq}\ in\ \text{Ref. [9]}} \cdot \left[\Delta_0(y_{2end} - y_{1end}) - \frac{r^2}{6.R_{y\_eq}}(y_{2end}^3 - y_{1end}^3) - \frac{\theta.r}{2}(y_{2end}^2 - y_{1end}^2)\right] \quad (13)$$

Note that r was fixed to 1 in Ref. [9] and that θ instead of $\theta.r$ was used in Ref. [1].

Note also that the non-truncated load can be defined as $\frac{2}{3}.P_{max}$, leading to the following relationships:

$$Q_{NT} = \frac{2}{3}.P_{\max}.\pi.a.b = \frac{2}{3}.\pi.E_{eq}.CP.R_{x\_eq}CA.R_{x\_eq}CB.\left(\frac{Q_{NT}}{E_{eq}R_{x\_eq}^2}\right)$$

$$\frac{2}{3}.\pi.CP.CA.CB = 1 \qquad \frac{\pi}{2}.\frac{CP.CB}{CD} = \frac{3}{4}.\frac{1}{CD.CA} = f_1 \tag{14}$$

It has been demonstrated in Ref. [1] that when the misalignment is nil and no truncation occurs, Q_{pc_trunc} (obtained by integrating dQ along the y axis) is analytically exactly equal to the non-truncated point contact load Q_{pc} or Q_{NT}, explaining why the same integration logic and corresponding Q_{pc_trunc} relationship has also been suggested for studying truncated point contact.

In the context of this study, when no misalignment occurs, a novel dimensionless approach can be suggested for calculating the dimensionless load $Q_{pc\_trunc}.R_{x\_eq}/\left(E_{eq}.L^3\right)$ as a function of the dimensionless deformation D. The dimensionless parameter T represents the truncation level ($T = 2.a_{NT}/L$), its lowest value being limited to 1 when no truncation occurs. So, for a truncated or non-truncated contact, one can initially suggest the following relationship (which will be corrected later using a correction factor called *Coef*):

$$f_1 = \frac{3}{4}.\frac{1}{CD.CA} = \frac{\pi}{2}.\frac{CP.CB}{CD} \qquad f_2 = \frac{2.CA}{\sqrt{CD}}$$

$$D = \frac{\delta_0.R_{x\_eq}}{L^2} = \frac{\Delta_0.R_{x\_eq}}{L^2} \qquad T = f_2.\sqrt{D}$$

$$\frac{Q_{pc\_trunc}}{\frac{Eeq.L^3}{R_{x\_eq}}} = f_1.D.Min(1,T).\left[1 - \frac{1}{3}.\left(\frac{Min(1,T)}{T}\right)^2\right] \tag{15}$$

4. Test without misalignment:

It is now easy to map k and D for calculating the dimensionless load, see Figure 2, obtained when studying a cylinder-on-cylinder case or equivalent cylinder on one plane.

The corresponding maximum contact pressure in a non-truncated point contact can be calculated using:

$$P_{\max} = E_{eq}.CP.\frac{L}{R_{x\_eq}}.\sqrt{\frac{D}{CD}} \tag{16}$$

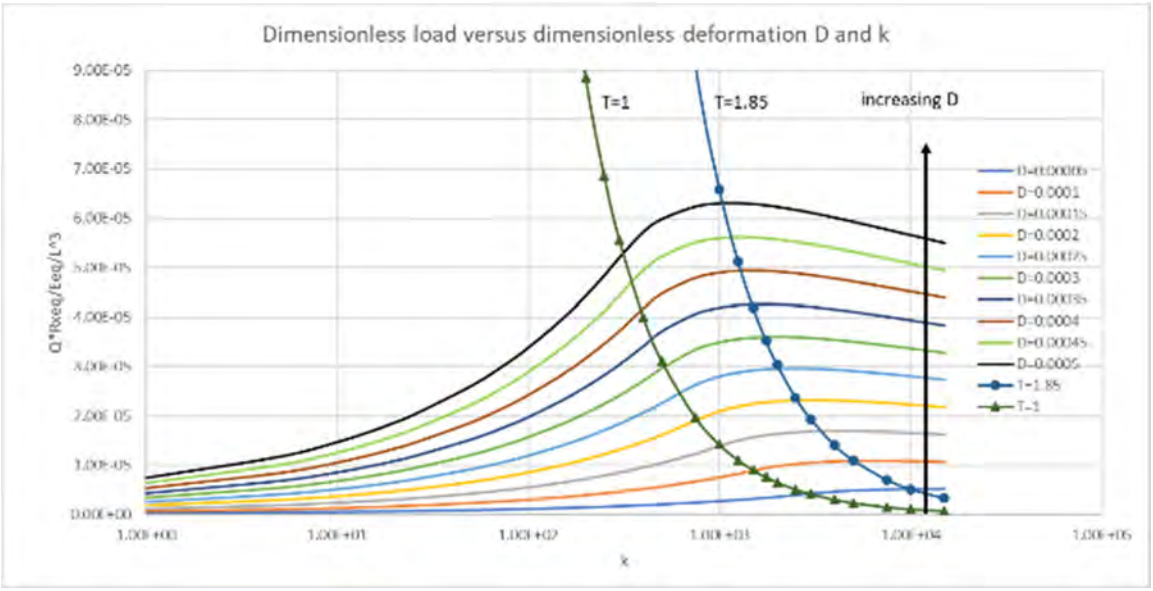

Fig. 2: Initial results obtained when scanning D and k

Non-truncated point contact occurs at low k and D values when $T < 1$, while truncated point contact can be observed at large k and large D values when $T > 1$.

In this study, the author noticed a suspicious abnormal behavior occurring at very large k and large D values when severe truncation occurs and $T > 1.85$

As shown in Figure 2, when fixing the deformation and increasing k, the load increases until it reaches a maximum value, then decreases slightly as k increases. It can be demonstrated that the latter maximum value is reached at any D levels when $T = 2.a_{NT}/L \approx 1.85$ or $k \approx 0.618*D^{-0.978}$.

The same trend has been observed when using the *Modified Teutsch* approach described later.

This behavior (load decrease when increasing k) seems suspicious since it is expected that a line contact (simulated using a very large k ratio) should be stiffer than a truncated point contact (simulated using a smaller k ratio).

The numerical explanation for such abnormal behavior is that f_1 is continuously decreasing when k increases (a point confirmed by using very large k ratio), while the bracket term used in Eq. (15) increases with k but reaches an asymptotic value of 1 when k is very large.

The physical explanation for such abnormal behavior is that, although moderate, coupling effects between slices cannot be ignored when calculating pressure and loads in truncated contacts. When analytically integrating the loads dQ (a function of the deformation δ in one slice only), these coupling effects are not considered.

5. Introduction of a correction factor called *Coef*

Beside the novel dimensionless approach and contact parameters curve-fitted in a wide k range, the primary novelty of this study lies in the introduction of a correction factor called *Coef*, used for matching the analytical truncated point contact results to the "exact" numerical results obtained using the tool *CST* (explained in Ref. [2]). The CST case studied corresponds to a cylinder on cylinder case having an equivalent radius R_{x_eq} equal to 10 mm, equivalent Young's modulus E_{eq} equal to $2.26*10^5$ N/mm^2 and roller length L equal to 30 mm. The deformation δ was fixed to 0.045 mm for obtaining a dimensionless deformation D equal to 5.E-4. Several values of R_{y_eq} were simulated for modifying the k ratio.

Note that pressure spikes are included when calculating Q_{CST}.

Coef has been defined as the ratio Q_{CST}/Q_{pc_trunc} and was indeed slightly larger than 1 as soon as truncation occurred but was equal to 1 when no truncation occurred (confirming the excellent match between Q_{CST} and Q_{NT} in non-truncated point contact cases).

This correction factor was then curve-fitted as a function of the dimensionless previously described parameter T for suggesting:

$$Coef \approx Max(1, T^{0.18}) \quad with \quad T = f_2.\sqrt{D} \qquad (17)$$

When no misalignment occurs, the novel and final suggested truncated or non-truncated dimensionless point contact load then reads:

$$\frac{Q_{pc\_trunc\_new}}{\frac{E_{eq}.L^3}{R_{x\_eq}}} = Coef.f_1.D.Min(1,T).\left[1-\frac{1}{3}.\left(\frac{Min(1,T)}{T}\right)^2\right] \quad with \qquad (18)$$

$$D = \frac{\delta_0.R_{x\_eq}}{L^2}$$

$$T = f_2.\sqrt{D}Coef \approx Max(1, T^{0.18})$$

$$f_1 = \frac{3}{4}.\frac{1}{CD.CA} = \frac{\pi}{2}.\frac{CP.CB}{CD} \qquad f_2 = \frac{2.CA}{\sqrt{CD}}$$

Note the compactness of the latter relationship. The match with *CST* results is now very good (see Figure 3, calculated with D = 0.0005 or δ = 0.045 mm in the cylinder-on-cylinder case).

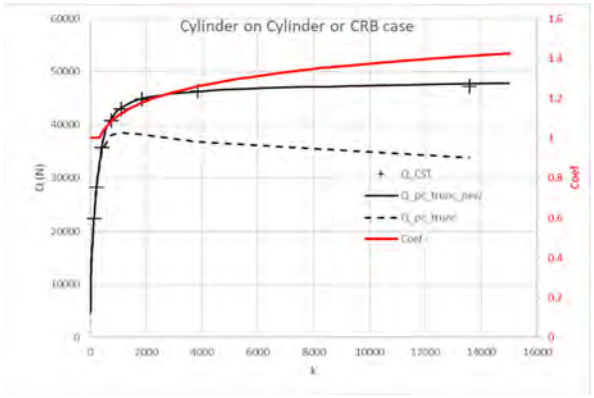

Fig. 3: New results obtained using Coef and scanning on k only, with D fixed to 0.0005

The correction factor varies between 1 and 1.4 in this case.

When using *Coef* and scanning on k and D, one obtains the following two Figures

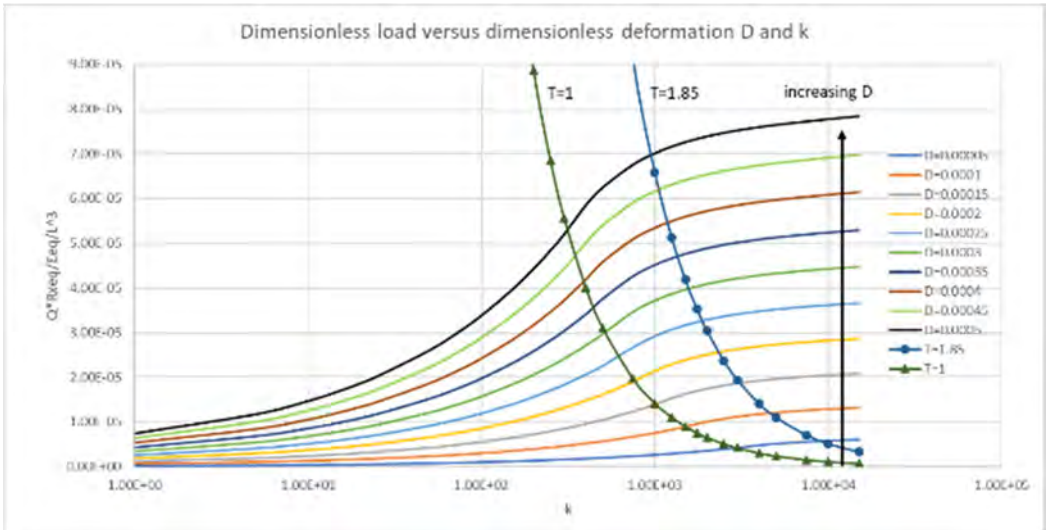

Fig. 4: The new dimensionless load (using Coef) obtained when scanning on k and D

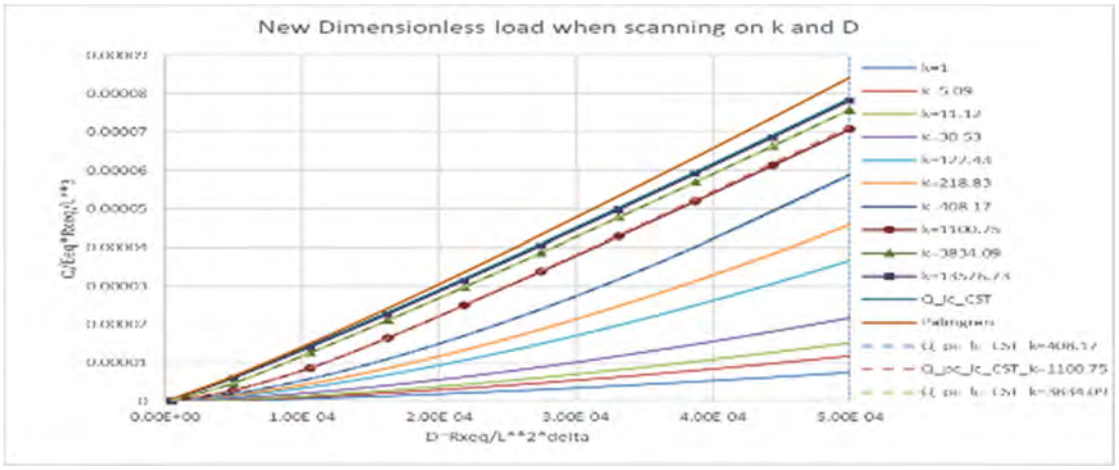

Fig. 5: The new dimensionless load (using Coef) obtained when scanning on k and D

The Palmgren load (upper curve), as well as the load corresponding to another model (*pc_lc_CST*, dotted line curves) accounting for a smooth transition from point to line contact, are also shown in Figure 5. These two load models are described later. The latter perfectly matches the new truncated point contact load.

Since the previously described dimensionless load is a function of D and T and since T is a function of D and f_2 (hence k), it is also possible to define another dimensionless load only function of T, see Eq. (19).

The latter relationship is simple to use and is certainly the most compact one for calculating the point contact load in non-truncated and truncated case. A single master curve can then be plotted next for replacing the set of master curves shown in Figure 4 and 5.

Engineers may however prefer to use D and k (hence T also) as inputs when calculating the load, so that the next developments are conducted using D and k.

$$Q_{Dimensionless} = \frac{f_2^2}{f_1}.\frac{Q_{pc\_trunc\_new}}{\frac{Eeq.L^3}{Rx\_eq}} =$$

$$Max(1,T^{0.18}).T^2.Min(1,T).\left[1-\frac{1}{3}.\left(\frac{Min(1,T)}{T}\right)^2\right]$$

$$= T^3.\left[\frac{2}{3}\right] \qquad if T \le 1$$

$$= T^{2.18}.\left[1-\frac{1}{3}.\left(\frac{1}{T}\right)^2\right] \qquad if T > 1$$

$$with \qquad (19)$$

$$T = f_2.\sqrt{\frac{\delta_0.R_{x\_eq}}{L^2}} \qquad \frac{f_2^2}{f_1} = \frac{16}{3}.CA$$

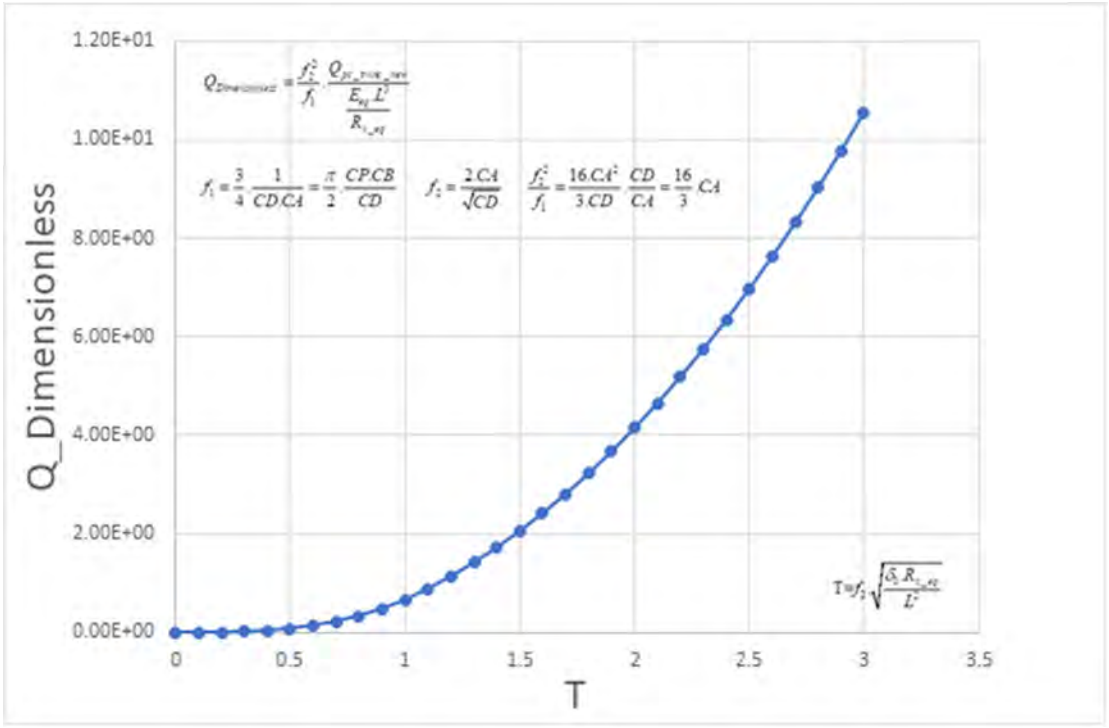

Fig. 6: Single master curve proposal: $Q_{Dimensionless}$ versus T

6. Pressure calculation:

The load dQ in each slice is also calculated using the same factor *Coef*:

$$dQ = Coef.f_1.E_{eq}.\delta.dy$$
$$= Coef.f_1.E_{eq}.\left(\Delta_0 - \theta.(r.y) - \frac{(r.y)^2}{2.R_{y\_eq}}\right).dy \quad (20)$$

Once the load dQ is known, the maximum pressure in any slice can be calculated using a point contact (recommended) or line contact relationship and the same correction factor *Coef*:

$$P_{pc} = \frac{\sqrt{Coef}.CP}{\sqrt{CD}}.E_{eq}.\sqrt{\frac{\delta}{R_{x\_eq}}}$$
$$= \sqrt{Coef}.\frac{E_{eq}.L}{R_{x\_eq}}.\frac{CP}{\sqrt{CD}}.\sqrt{D} \quad or \quad (21)$$
$$P_{lc} = E_{eq}.\sqrt{\frac{dQ}{2.\pi.E_{eq}.R_{x\_eq}.dy}} =$$
$$\sqrt{Coef}.\frac{E_{eq}.L}{R_{x\_eq}}.\sqrt{\frac{CP.CB}{4.CD}}.\sqrt{D}$$

knowing that $P_{pc} \approx P_{lc}$ at large k ratios, because:

$$\frac{P_{pc}}{P_{lc}} = \frac{2.CP}{\sqrt{CP.CB}} = 2.\sqrt{\frac{CP}{CB}} \approx 1 \quad (22)$$

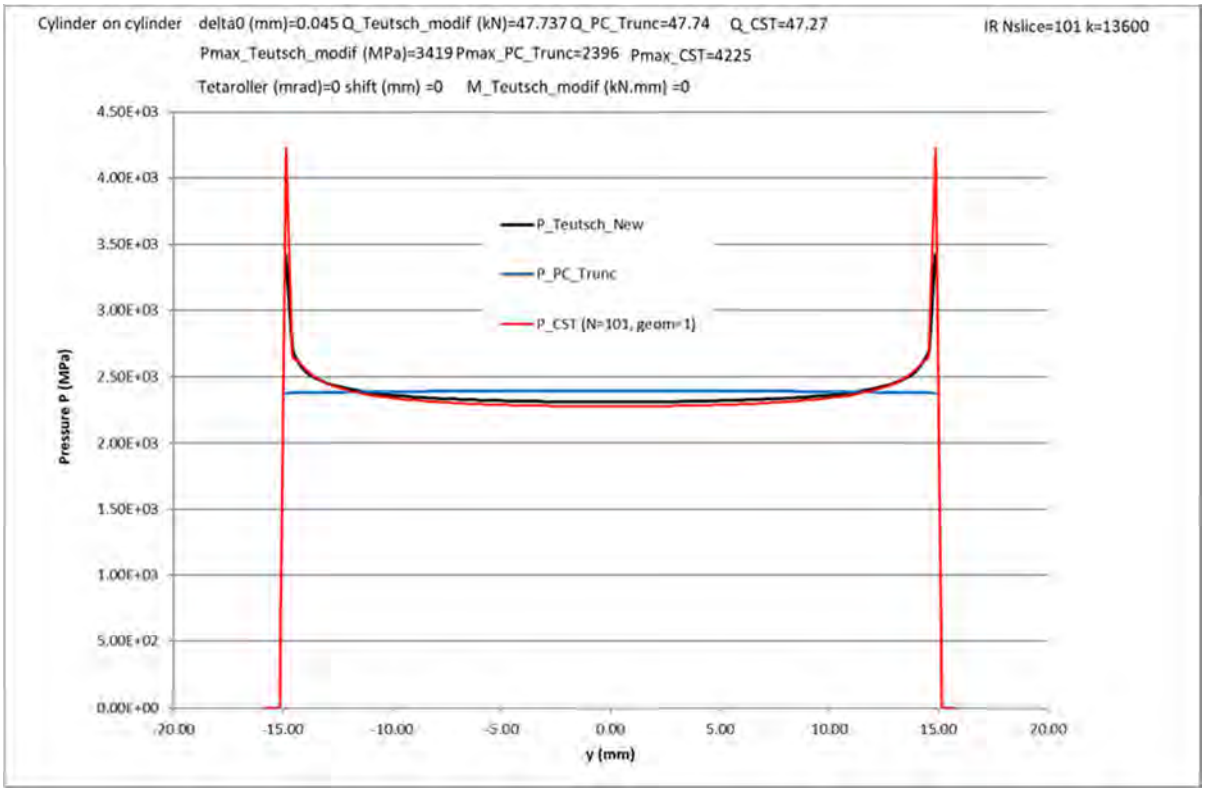

*Fig. 7: Pressure distribution along the cylinder-on-cylinder contact, δ = 0.045 mm and k = 13.6*10³*

Figure 7 shows one example of calculated contact pressure distribution corresponding to the cylinder-on-cylinder case with a deformation of 0.045 mm and k ratio of 13.6*10³. At the contact center, the newly suggested truncated point contact pressure is close to both *CST* and the *Teutsch_New* pressure (model described later). At the edge, pressure spikes occur but cannot be predicted without considering coupling effects between the slices (as accounted for in *CST* and the *Modified Teutsch* approach).

Other examples of pressure distributions in spherical roller bearings (SRBs) have been given in Ref. [1] (without using the factor *Coef*, but by imposing the same contact load instead of the deformation herein, so that the contact deformation varies slightly as a function of the model used). Assuming the loads are also similar when using miscellaneous models with a constant deformation and the factor *Coef*, the pressure distribution should be close to what has been shown in Ref. [1], see the next two examples (Figures 8 and 9) extracted from Ref. [1], at low load (non-truncated point contact) and large load (truncated point contact). The axis along the contact length in those two examples is called x (instead of y, as in our current work).

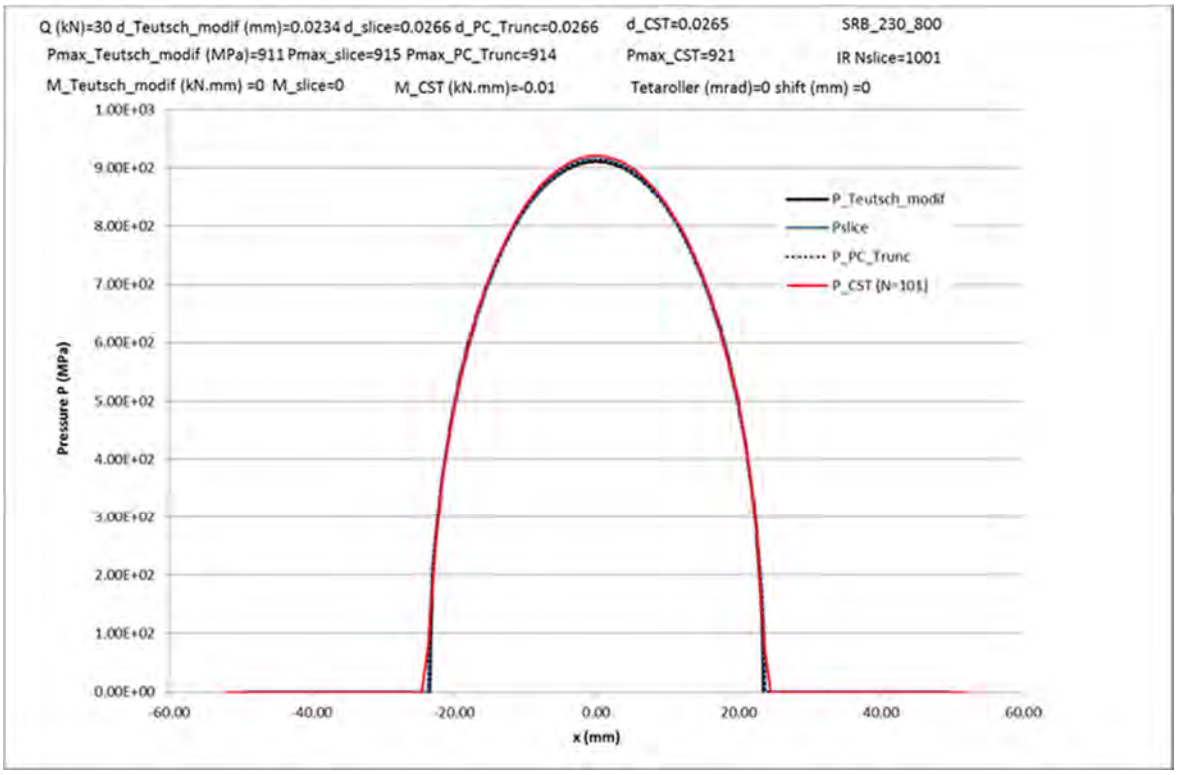

Fig. 8: SRB example at low load as presented in Ref. [1] (constant load imposed)

Note how the *Modified Teutsch* model (initially developed by Teutsch and Sauer for line contact only) is now also appropriate for describing point contact.

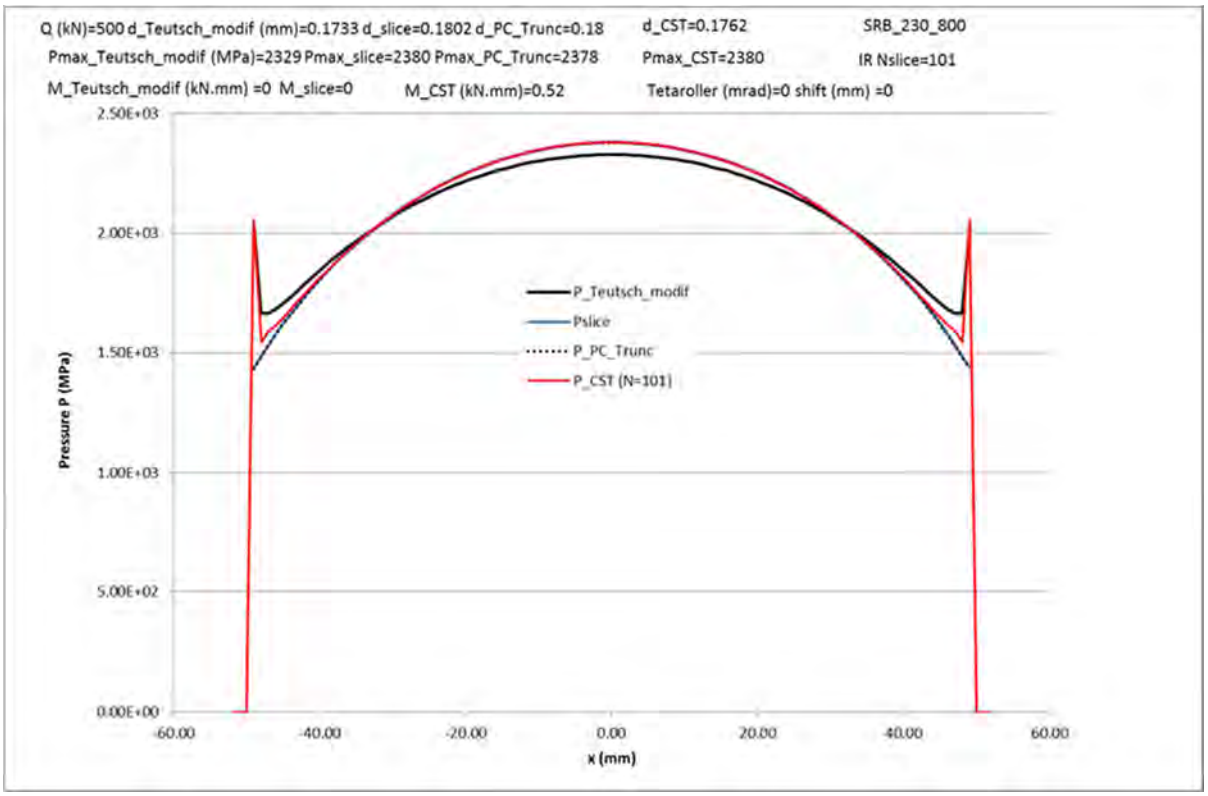

Fig. 9: SRB example at large load as presented in Ref. [1] (constant load imposed)

When using single crown profiles and ignoring pressure spikes, the pressure can finally be approximated at any (*x,y*) point using:

$$P(x,y) = \sqrt{Coef}.\frac{CP}{\sqrt{CD}}.E_{eq}.\sqrt{\frac{\delta_{\max}}{R_{x\_eq}}}.\sqrt{1-\left(\frac{x}{b}\right)^2-\left(\frac{y}{a}\right)^2} \quad (23)$$

$$with \quad b = \sqrt{Coef}.\frac{CB}{\sqrt{CD}}.\sqrt{R_{x\_eq}.\delta_{\max}} \quad and \quad a = \frac{CA}{\sqrt{CD}}.\sqrt{R_{x\_eq}.\delta_{\max}}$$

When truncation occurs, the *y* values are of course limited to ± *L*/2.

A double integration of *P(x,y).dx.dy* leads to the appropriate load *Q*.

7. Line contact calculation:

Although beyond the scope of this paper, the latter truncated point contact load relationship can also be used for defining a new load relationship (see Refs. [1] and [6], among others) corresponding to a line contact.

When severe truncation occurs, the bracket term in Eq. (18) is equal to 1 while *Coef* is always equal to $T^{0.18} = f_2^{0.18}.D^{0.09}$, so that the load becomes:

$$\frac{Q}{\frac{E_{eq}.L^3}{R_{x\_eq}}} = f_1.f_2^{0.18}D^{1.09} \quad (24)$$

The product $f_1.f_2^{0.18}$ is plotted next against *k*, thanks to the very wide *k* that was simulated. It can be fixed to 0.3 when *k* is large. The small increase observed at very large *k* values is due to pressure spikes and can be considered when using $f_1.f_2^{0.18}$ instead of 0.3.

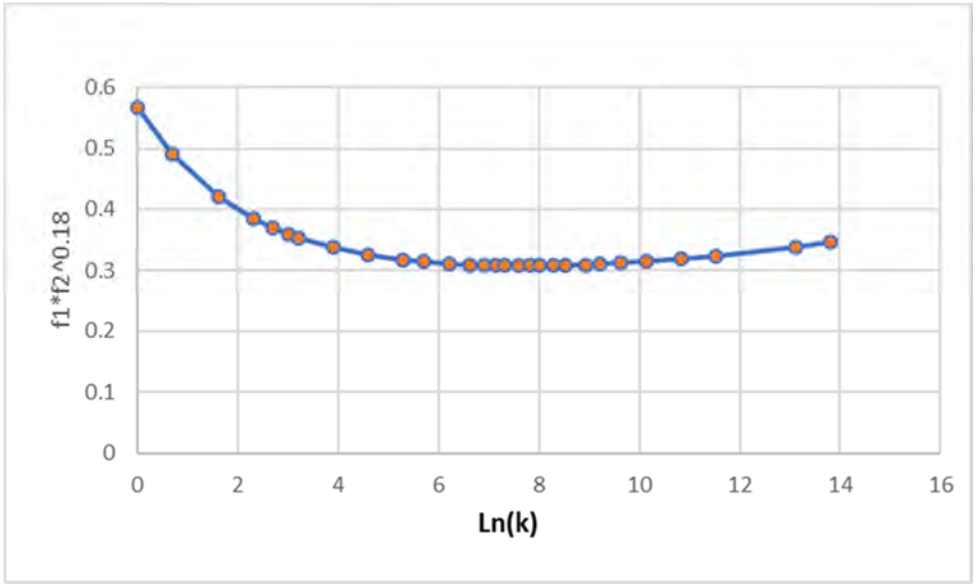

Fig. 10: Factor to use when defining Q_{LC_CST}

The *CST* line contact load can therefore be defined as:

$$\frac{Q_{LC\_CST}}{\frac{E_{eq}.L^3}{R_{x\_eq}}} \simeq 0.3 * D^{1.09} \quad (25)$$

Or

$$Q_{lc\_CST} \approx 0.3 * \frac{E_{eq}.L^3}{R_{x\_eq}}.D^{1.09} = 0.3 * E_{eq}.L^{0.82}.R_{x\_eq}^{0.09}.\delta^{1.09} \quad (26)$$

The latter relationship accounts for a minor effect of R_{x_eq} on the load and is close to the well-accepted "empirical" relationship of Palmgren (see the Palmgren load also plotted in Figure 5):

$$Q_{Palmgren} \approx 0.347 * E_{eq}.L^{\frac{0.8}{0.9}}.\delta^{\frac{10}{9}} \quad (27)$$

Other line contact relationships are discussed in more detail in Refs. [1] and [6], including an interesting effect of ring thickness on the load, but this topic is beyond the scope of this paper.

8. Additional model using a point contact-line contact smooth transition:

One can also include the latter Q_{lc_CST} relationship when calculating the load using the point contact-line contact model described in Refs. [6] and [1], which is valid only when no misalignment occurs. A smooth transition from point contact to line contact occurs when the deformation exceeds a deformation of transition δ_T:

$$Q_{PC} = \frac{E_{eq}.L^3}{R_{x\_eq}}.\left(\frac{1}{CD}\right)^{1.5}.D^{1.5} = \frac{E_{eq}.\sqrt{R_{x\_eq}}}{CD^{1.5}}.\delta^{1.5} = K_{PC}.\delta^{1.5} \quad with$$

$$K_{PC} = \frac{E_{eq}.\sqrt{R_{x\_eq}}}{CD^{1.5}} = f_3.E_{eq}.\sqrt{R_{x\_eq}}$$

$$Q_{LC\_CST} \approx 0.3 * \frac{E_{eq}.L^3}{R_{x\_eq}}.D^{1.09} = 0.3 * E_{eq}.L^{0.82}.R_{x\_eq}^{0.09}.\delta^{1.09} = K_{LC}.\delta^n \quad with$$

$$K_{LC} = 0.3 * E_{eq}.L^{0.82}.R_{x\_eq}^{0.09} \qquad n = 1.09$$

$$\delta_T = \left(\frac{n}{1.5}.\frac{K_{LC}}{K_{PC}}\right)^{\frac{1}{1.5-n}} \qquad \Delta Q = K_{LC}.\delta_T^n - K_{PC}.\delta_T^{1.5}$$

$$When\ \delta \le \delta_T: \qquad Q_{PC\_LC} = Q_{PC} = K_{PC}.\delta^{1.5}$$

$$When\ \delta > \delta_T: \qquad Q_{PC\_LC} \approx Q_{LC} - \Delta Q = K_{LC}.\delta^n - \Delta Q$$

(28)

9. Improvement of the *Modified Teutsch* model

In Ref. [10], Teutsch and Sauer develop an interesting approach for calculating the load and pressure distribution (including pressure spikes with coupling effects between slices) in line contact, using the geometrical interference Δ in slices and Houpert's line contact proposal with ring thickness effects included as described in Ref. [6].

Some substantial enhancements have been provided by Houpert in Ref. [1] for developing the so-called *Modified Teutsch* model:

- Use of a dimensionless approach with a compliance and stiffness matrix defined once only as a function of the number of slices used.
- Use of Houpert's curve-fitted factors *CD, CP* and *CB* for defining the factor *s* and *1/s* and the linear elastic model (where *dQ* is now proportional to the geometrical interference Δ in each slice) for adapting Teutsch's model to point contact as well.

This *Modified Teutsch* model is described in Figure 11, a slide extracted from Ref. [1].

Figures 8 and 9 show some results obtained with the latter model.

Geometrical interference: $\Delta_i = \delta_0 - \text{Profile}(x_i) - \theta . x_i$

Use in each slice Houpert's load - deformation model:

$\Delta_i = s.dQ_i \quad with \quad s = \frac{2}{\pi . E_{eq}} . \frac{CD}{CP.CB.dx} = f(k, E_{eq}, dx)$

Use a dimensionless approach: $w_{i,j} = \left(\frac{1}{|i-j|} \right)$ *and* $w_{i,i} = 4$ $(when\ i = j)$

Define $\left[S_{i,j} \right] = \frac{N_{slice}}{\sum_{i,j} w_{i,j}} . \left[w_{i,j} \right]$ (once only as a function of N_{slice})

Define $\left[S_{i,j} \right]^{-1}$ (once only as a function of N_{slice}) to read as input

Calculate load dQ_i & Q *as*: $\{dQ_i\} = \frac{1}{s} . \left[S_{i,j}^{-1} \right] \{\Delta_j\} \qquad Q = \sum_{i=1,N_{slice}} dQ_i$

Multiply dQ_1 & $dQ_{N_{slice}}$ *by* 1.25 *for matching CST results*

(solve for δ_0 if load Q is imposed)

Fig. 11: The Modified Teutsch model as explained in Ref. [1]

The novel *Teutsch_New* approach suggested herein uses *Coef/s* instead of *1/s* when calculating *dQ* and $Q_{Teutsch\ New}$, as well as the new contact pressure (including pressure spikes) in each slice, see for example Fig. 7 showing a good match with *CST* results.

10. Tests using other bearing types and no misalignment

Beside the *Teutsch_New* results already shown in Figure 7, one can now compare in the next two figures (12 and 13) the results published in Ref. [1] (Q_{pc_trunc} was then called $Q_{pc\_Trunc\_approach2}$) to the results obtained using this newly suggested approach and the introduction of the correction factor *Coef*.

Figure 12 shows some results presented in Ref. [1] (without the use of *Coef*) using tapered roller bearings and spherical roller bearings. Other models ($Q_{pc\_lc\_LH}$) with a ring housing thickness *t* were also tested in Ref. [1] but are not discussed herein. The previously described *Modified Teutsch* load (including pressure spikes) is also shown.

The calculated truncated point contact load was indeed in some cases up to 10% smaller than the *CST* results, but was deemed acceptable at this time in the context of an engineering approach.

In this paper, the *Teutsch_New* approach was simply tested in Fig. 13 using the same correction factor *Coef* previously described, while the point contact-line contact model was tested using Q_{lc_CST}, hence without considering the ring thickness effect on the load.

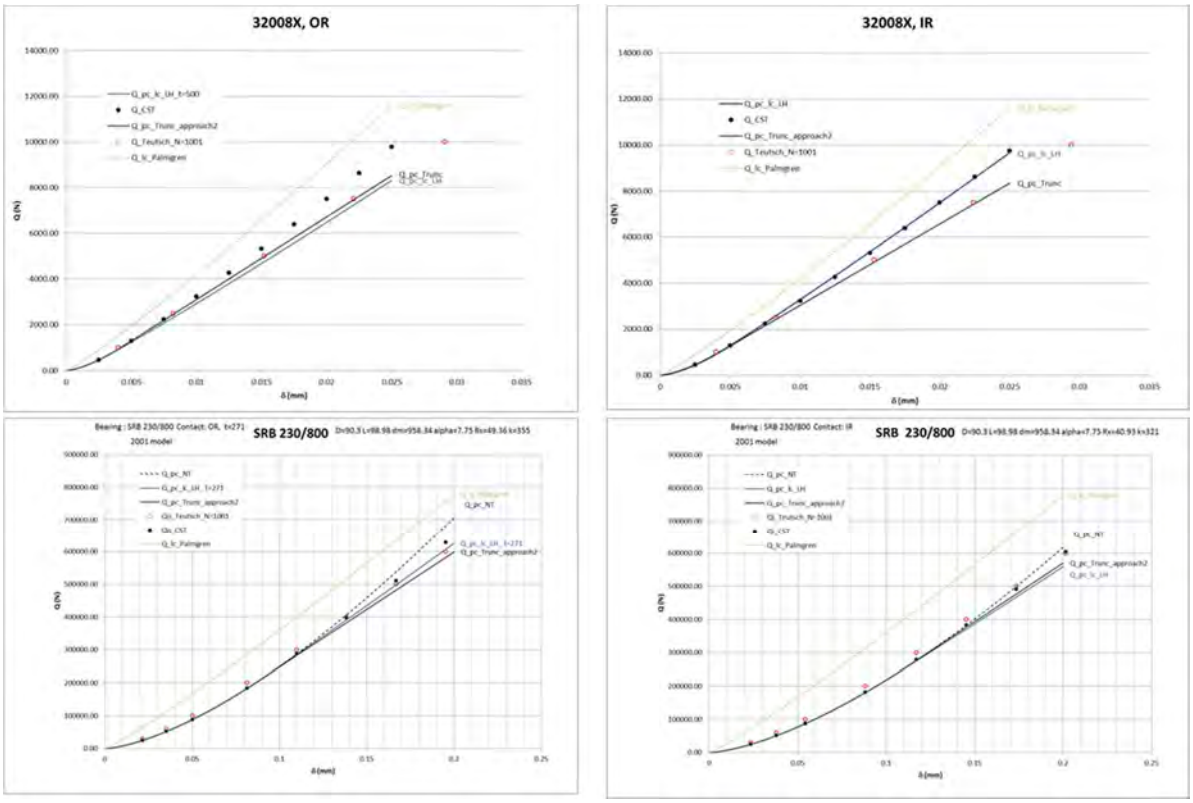

Fig. 12: Results presented in Ref. [1] without the use of Coef

Using next the new suggested truncated point contact model, excellent results and match with *CST* results were obtained; the *Teutsch_New* and *pc_lc_CST* results agree well, also. In this case, *Coef* varies from 1 to 1.2

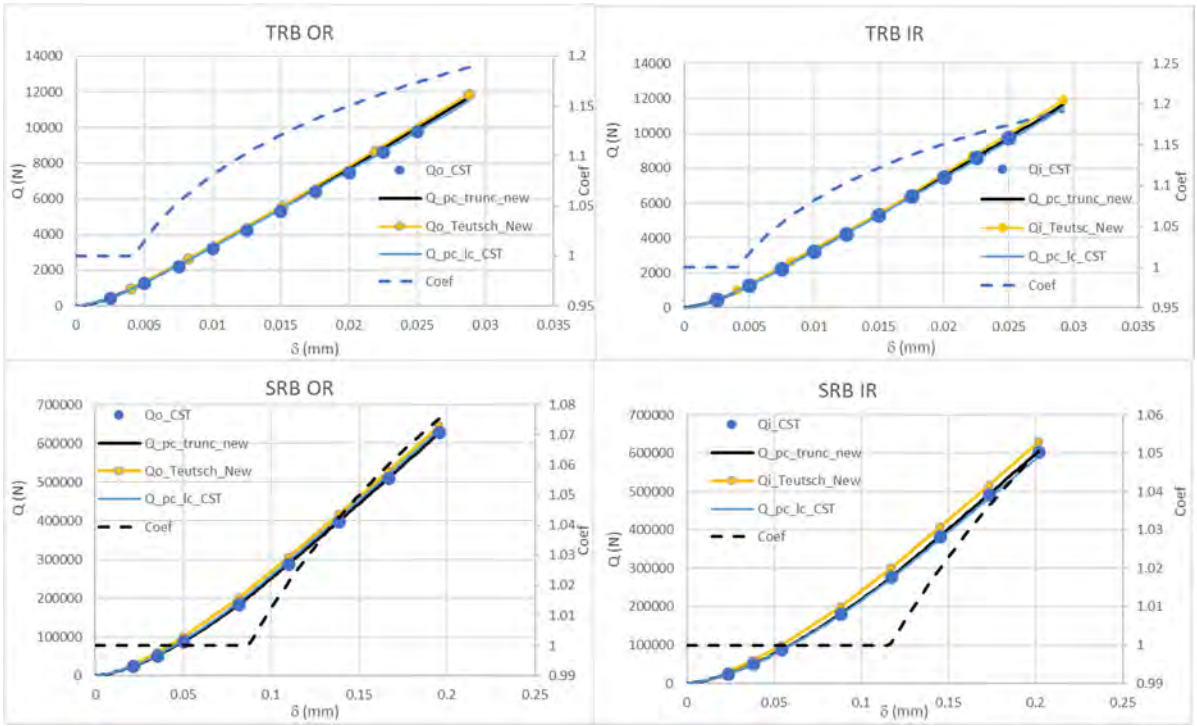

Fig. 13: Results obtained with the newly suggested model (with the correction factor Coef)

11. Suggested relationships accounting for misalignment

The author suggests that a similar model should be developed and tested against *CST* or Cretu's tool under misalignment when non-symmetrical truncation occurs. The new coefficient *Coef* (including misalignment) could be defined in future studies and, it is hoped, published in a subsequent paper.

Some preliminary and encouraging results have been obtained, although they are not shown here in detail.

Using the dimensionless contact boundaries ($Y = y/a_{NT}$) and misalignment, Y_{Left} is not equal to $-Y_{Right}$, but the use of *Coef* can be tested with the maximum dimensionless deformation D_{max}:

$$Coef \approx \left(f_2.\sqrt{D_{\max}}\right)^{0.18} \quad with\ D_{\max} = D_0 + \frac{k.\theta^2.R_{x\_eq}^2}{2.L^2} \tag{29}$$

where D_0 is the dimensionless deformation at the roller-race center.

Alternatively, assuming truncation occurs at both ends of the contact, one could also test:

$$Coef \approx X^{0.18} \quad with\ X = \frac{1}{2}.\left(\frac{1}{Y_{Right}} + \frac{1}{|Y_{Left}|}\right) \tag{30}$$

If truncation occurs at one end only (on the right, for example), one may also try:

$$X = \frac{1}{2}.\left(\frac{1}{Y_{Right}} + 1\right) \tag{31}$$

Although not fully tested and validated, the following truncated point contact load is suggested for studying the roller-inner race contact:

$$Q_{pc\_trunc} = E_{eq}.Coef.f_1 \cdot \left[\Delta_0\left(y_{2end} - y_{1end}\right) - \frac{r^2}{6 \cdot R_{y\_eq}}\left(y_{2end}^3 - y_{1end}^3\right) - \frac{\theta.r}{2}\left(y_{2end}^2 - y_{1end}^2\right)\right] \quad with$$

$$Coef \approx Max\left[1, \left(f_2.\sqrt{D_{\max}}\right)^{0.18}\right] \quad and \quad D_{\max} = D_0 + \frac{k.\theta^2.R_{x\_eq}^2}{2.L^2} \tag{32}$$

$$y_{1end} = \max\left[\frac{R_y.\left(-\theta - \sqrt{\theta^2 + 2.\frac{\Delta_0}{R_{y\_eq}}}\right)}{r}; -\frac{L}{2}\right] \qquad y_{2end} = \min\left[\frac{R_y.\left(-\theta + \sqrt{\theta^2 + 2.\frac{\Delta_0}{R_{y\_eq}}}\right)}{r}; \frac{L}{2}\right]$$

A dimensionless approach could also be developed for discussion in a subsequent study and paper.

When misalignment occurs, a tilting moment around the center of the race ($y = 0$) can also be calculated (see Refs. [1] and [9]), now corrected using the factor *Coef*. For example, at the roller-inner race contact, the tilting moment applied on the roller reads:

$$M_{pc\_trunc} = Coef.f_1.E_{eq} \cdot \left[\frac{\Delta_0}{2}\left(y_{2end}^2 - y_{1end}^2\right) - \frac{r^2}{8 \cdot R_{y\_eq}}\left(y_{2end}^4 - y_{1end}^4\right) - \frac{\theta.r}{3}\left(y_{2end}^3 - y_{1end}^3\right)\right] \tag{33}$$

Sign conventions should be well defined and applied when calculating the roller-outer race contact.

12. Conclusions and recommendations

Point contact parameters have been calculated using two approaches for calculating elliptical integrals (numerical and Tripp's analytical ones) in a very wide range of k, then curve fitted as a function of k.

The new curve fitted dimensionless relationship presented herein appears quite accurate for calculating the load in truncated or non-truncated point contact with a single crown profile.

The new dimensionless load can therefore be easily calculated analytically as a function of a dimensionless deformation parameter and k ratio.

Alternatively, another dimensionless load can be calculated as a function of one single dimensionless parameter T.

The analytical results have been successfully tested against accurate numerical results obtained using the numerical tool *CST*, under conditions of no misalignment, thanks to the introduction of a correction factor *Coef* equal to 1 when no truncation occurs and varying between 1 and 1.4 as truncation increases.

Also, a new line contact relationship corresponding to truncated point contact at very large k values has also been developed for retrieving CST results and accounting for a smooth transition from point contact to line contact relationship as k increases. The new CST line contact load relationship is close to Palmgren's relationship.

Although not extensively tested herein, it has been shown that the same factor *Coef* (or a slightly modified correction factor) can be used in the *Teutsch_New* approach (which includes pressure spikes and accounts for any profile) described in Ref. [1].

The main recommendation is to further test the suggested relationships when misalignment occurs.

The same model should therefore be tested against *CST* or Cretu's tool results when misalignment and non-symmetrical truncation occur.

Initial results obtained with misalignment and any profile (presented in Ref. [1] without the use of *Coef*) were satisfactory and are expected to improve when using the same or a revised factor *Coef*.

Also, the use of the same factor *Coef* (or a modified correction factor) with a log profile or any other complex profile) as described in Ref. [1] should be tested with the suggested analytical model and the k ratio defined using the main crown radius at $y = 0$. Preliminary results were very encouraging.

Alternatively, the author invites any readers having access to such enhanced tools to benchmark their numerical results against the results obtained using the suggested analytical relationships described in this paper.

Acknowledgments

The author would like to thank Dragos Oprescu, chief engineer for Timken Europe, for his permission to use some Timken tools (including *CST*) for studying the cylinder-on-cylinder case (used as a reference for defining the correction factor *Coef*).

The author would also like to thank Spiridon Cretu, Professor Emeritus, Mechanical Engineering Department, Iasi University, Romania, for his gracious study with his tools of the same cylinder-on-cylinder case, matching a few CST results within 1.2 %.

Prof. Patrick L. Wong and Dr. Liang Guo, City University of Hong Kong, China, are also deeply acknowledged for their interest in the study and some preliminary discussions on the topic.

References:

[1] L. Houpert, "Miscellaneous Engineering Approaches to Contact Elasticity Calculations," Bearing World International Bearing Conference, Kaiserslautern, Germany, Proceedings of the Conference (2018)

[2] M. Hoeprich, "Numerical procedure for designing rolling element contact geometry as a function of load cycle," SAE technical paper, series 850764 (1985)

[3] S. Cretu, "Pressure Distribution in Concentrated Rough Contacts", 2005, Bull.Inst. Polit. Iasi, **LI**, 1-2, pp. 1-31.

[4] T.A. Harris and M.N. Kotzalas, 2007, "Essential concepts of bearing technology," *Rolling Bearing Analysis*, 5th Edition, CRC Taylor & Francis Group.

[5] J.H. Tripp, "Hertzian contact in two and three dimensions," NASA technical paper 2473 (July 1985)

[6] L. Houpert, "An Engineering Approach to Hertzian Contact Elasticity – Part I," *J. Tribol* 123(3), 589-594 (July 10, 2000)

[7] G. Dalmaz, 'Le Film Mince Visqueux dans les Contacts Hertziens en Regime Hydrodynamique et Elastohydrodynamique' ("Thin Viscous Film in Hertzian Contacts in Hydrodynamic and Elastohydrodynamic Regimes"), Docteur d'Etat Es Sciences Thesis, INSA, Lyon, France (1979)

[8] L. Houpert, "Hydrodynamic Load Calculation in Rolling Element Bearings," Tribology Transactions Vol. 59, No. 3 (2016)

[9] L. Houpert, "An Engineering Approach to non-Hertzian Contact Elasticity – Part II," *J. Tribol* 123(3), 589-594 (July 10, 2000)

[10] *R. Teutsch and B. Sauer,* "An alternative slicing technique to consider pressure concentrations in non-Hertzian contacts," *J. Tribol* 126(3), 436-442 (June 28, 2004)

Appendix: Calculation of elliptical integrals and Hertz coefficients

Using Ref. [4] (Harris) or [5] (Tripp), one can calculate the two elliptical integrals *E* and *F* as a function of the input parameter $\kappa = a / b$. Once κ, *E* and *F* are known, the *k* ratio can be derived.
Following are the relationships used:

$$\kappa = \frac{a}{b} \qquad (input)$$

$$E = \int_0^{\frac{\pi}{2}} dE = \int_0^{\frac{\pi}{2}} \left[1 - \left(1 - \frac{1}{\kappa^2} \right) . \sin^2 \psi \right]^{\frac{1}{2}} . d\psi$$

$$F = \int_0^{\frac{\pi}{2}} dF = \int_0^{\frac{\pi}{2}} \left[1 - \left(1 - \frac{1}{\kappa^2} \right) . \sin^2 \psi \right]^{-\frac{1}{2}} . d\psi \qquad (34)$$

$$k = \frac{\kappa^2 - \frac{F}{E}}{\frac{F}{E} - 1} \qquad (output)$$

The numerical integrals can be conducted using 10,001 points and a degree 2 polynomial description describing three consecutive points, leading to:

$$Integral = \left(\sum_{i=4}^{i=N-3} y_i + \frac{9}{24} . y_1 + \frac{28}{24} . y_2 + \frac{23}{24} . y_3 + \frac{23}{24} . y_{N-2} + \frac{28}{24} . y_{N-1} + \frac{9}{24} . y_N \right) . \Delta x \qquad (35)$$

where y_i is the value of *dE* or *dF* calculated at abscissa ψ_i and Δx is equal to $\frac{\pi}{2*10000}$.

Using a series expansion valid at large κ values only, Tripp suggested two analytical relationships for calculating *E* and *F*:

$$\Lambda = \ln(4.\kappa)$$

$$At \text{ large } \kappa: \qquad (36)$$

$$E_{Tripp} \approx 1 + 0.5 * (\Lambda - 0.5) . \kappa^{-2} \qquad F_{Tripp} \approx \Lambda + 0.25 * (\Lambda - 1) . \kappa^{-2}$$

It is also possible to impose the *k* ratio. The latter input ($\kappa = a / b$) is then an unknown that can be calculated using iterations on κ until the new value of κ is equal to the previous one:

$$\kappa_{new} = \left[(k+1) . \frac{F}{E} - k \right]^{\frac{1}{2}} \qquad (37)$$

In the latter relationship, *E* and *F* are calculated using the previous κ value.

Tripp, Ref. [5], also recommended the use of the approximation $\kappa \approx k^{\frac{2}{3}}$ in his relationships, but this approximation should be avoided because not accurate enough.

The elliptical integrals can therefore be calculated for any *k* ratio, *k* ranging from 1 to 1.E7 for example, see next extreme example corresponding to *k* = 1.E7.

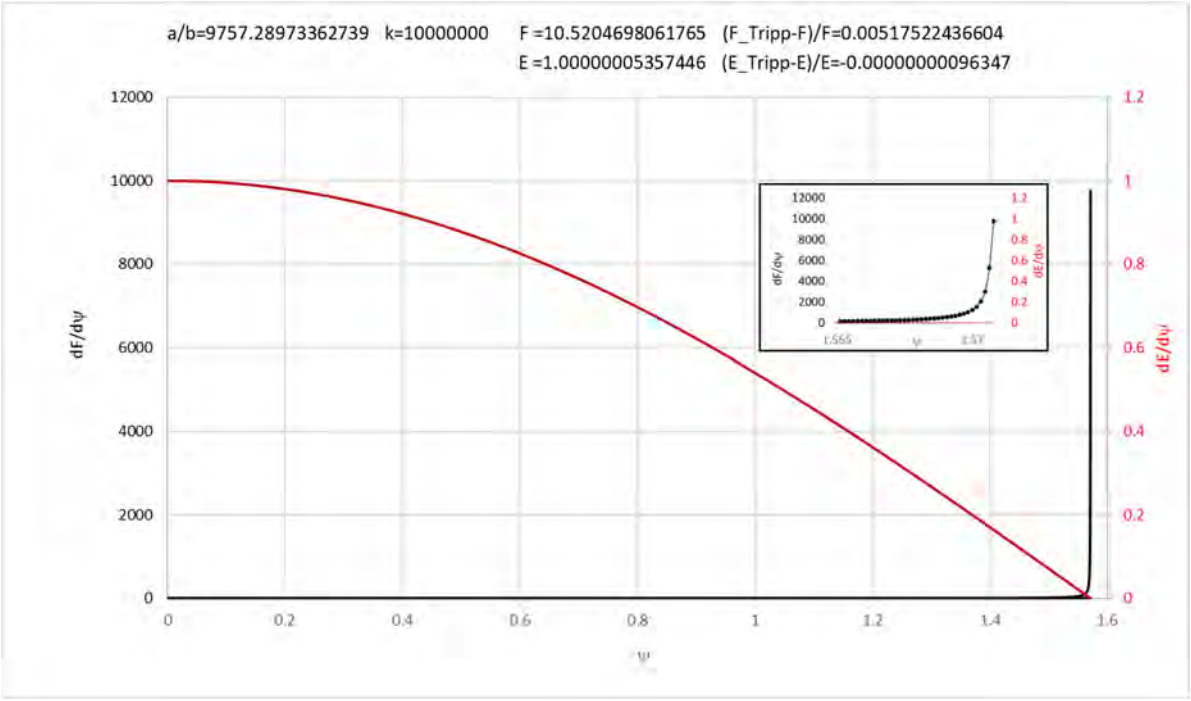

Fig. 14: $dF/d\psi$ & $dE/d\psi$ distribution for $k = 1*10^7$

A sharp increase of dF can be noticed near $\psi = \pi/2$ (see also the zoom in Fig. 14) explaining why the accuracy (when using Tripp's analytical solution as reference) on the calculated integral F is not very good (despite the 10,001 points used) and equal to about 5.18E-3.

It is however possible to improve the accuracy of the numerically calculated integrals by conducting the integration in two steps: for example, from 0 to 1.55 with 10,001 points and from 1.55 to $\pi/2$ again using 10,001 points. The relative difference with Tripp's integral then becomes equal to 1.20E-9 and 4.0E-14 for F_{Tripp} and E_{Tripp} respectively.

In Ref. [7], Dalmaz showed tabulated results versus the parameter $F(\rho)$ described by:

$$F(\rho) = \frac{\frac{1}{R_{x1}} - \frac{1}{R_{y1}} + \left(\pm\frac{1}{R_{x2}}\right) - \left(\pm\frac{1}{R_{y2}}\right)}{\sum\rho} \qquad with \quad \sum\rho = \frac{1}{R_{x1}} + \frac{1}{R_{y1}} \pm \frac{1}{R_{x2}} \pm \frac{1}{R_{y2}} \tag{38}$$

Let us introduce, as in Ref. [6], the equivalent radii ratio k defined by:

$$\frac{1}{R_{x\_eq}} = \frac{1}{R_{x1}} + \frac{1}{R_{x2}} \qquad \frac{1}{R_{y\_eq}} = \frac{1}{R_{y1}} + \frac{1}{R_{y2}} \qquad k = \frac{R_{y\_eq}}{R_{x\_eq}} \tag{39}$$

One can then write:

$$\sum\rho = \frac{1}{R_{x\_eq}} + \frac{1}{R_{y\_eq}} = \frac{1}{R_{x\_eq}}.\left(1 + k^{-1}\right) \qquad and \qquad F(\rho) = \frac{\frac{1}{R_{x\_eq}} - \frac{1}{R_{y\_eq}}}{\frac{1}{R_{x\_eq}} + \frac{1}{R_{y\_eq}}} = \frac{1 - k^{-1}}{1 + k^{-1}} \tag{40}$$

Dalmaz's tabulated results could therefore be shown in Ref. [6] as a function of $F(\rho)$ or k limited to a maximum value equal to 13,576.73, but for this study there was a need to calculate elliptical integrals and corresponding contact parameters at larger k values.

Using either the numerical integration or Tripp's approach and appropriate iterations, the values of κ , F and E are then known at a given k ratio, as well as the corresponding a^*, b^*, δ^*, leading to the derivation of the coefficients CA, CB, CD, CP, f_1, f_2 and f_3, see Table 2 for example.

$$a^* = \left[2.\kappa^2.\frac{E}{\pi}\right]^{\frac{1}{3}} \qquad b^* = \frac{a^*}{\kappa} \qquad \delta^* = \frac{2.F}{\pi}.\left[\frac{\pi}{2.\kappa^2.E}\right]^{\frac{1}{3}}$$

$$CA = \left[\frac{3.k}{1+k}\right]^{\frac{1}{3}}.a^* \qquad CB = \left[\frac{3.k}{1+k}\right]^{\frac{1}{3}}.b^* \qquad CD = \left[\frac{9.(1+k)}{k}\right]^{\frac{1}{3}}.\frac{\delta^*}{2} \tag{41}$$

$$CP = \frac{1.5}{\pi.a^*.b^*}.\left[\frac{1+k}{3.k}\right]^{\frac{2}{3}} \qquad f_1 = \frac{3}{4}.\frac{1}{CD.CA} \qquad f_2 = \frac{2.CA}{\sqrt{CD}} \qquad f_3 = \frac{1}{CD^{1.5}}$$

Results obtained with Tripp's models are compared in the next Figure to the numerical ones obtained using the two steps integration procedure.

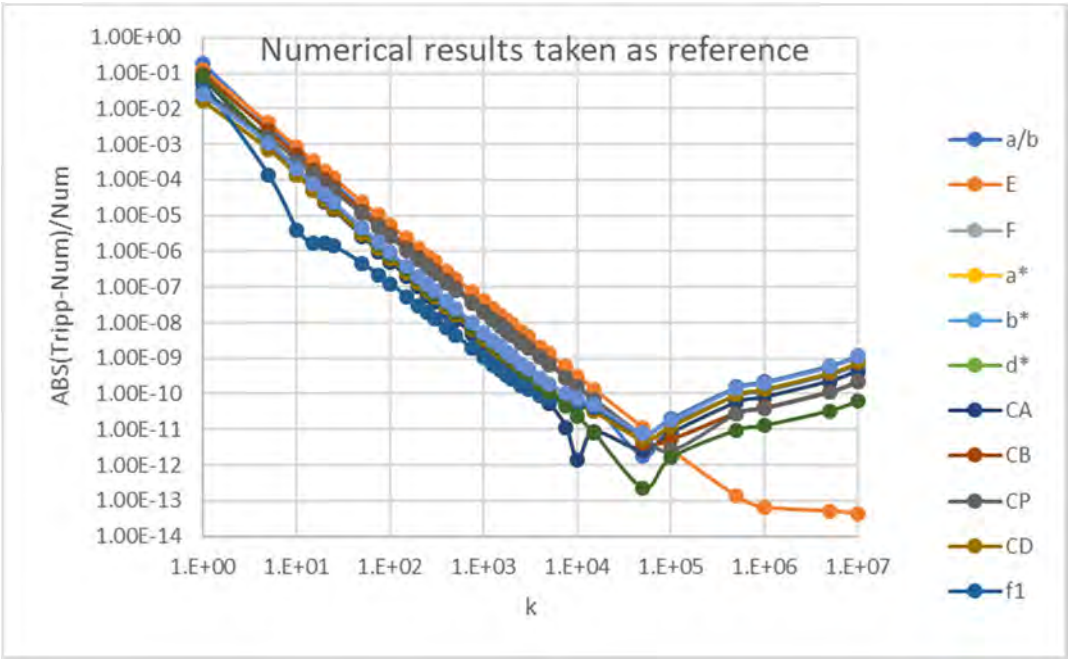

Fig. 15: Comparison of Tripp's results to those obtained using a numerical integration in two steps

One sees that Tripp's results are indeed not accurate enough at small k ratios ($k < 10$) but become very accurate as k increases — the error being of the order of 1.10^{-9} or less when k is larger than 3,000.

At very large ratio, the results obtained numerically with the two steps integration procedure are however less accurate than Tripp's analytical results.

It can therefore be recommended to adopt the two steps integration results when k *is* ≤ 3,000 and Tripp results when $k > 3{,}000$

The results obtained have been shown in Table 2 and Figure 1 with a proven accuracy of 1.E-9 or less.

Last, but not least, appropriate curved-fitted relationships must be suggested for calculating all Hertzian factors CA, CB, CP, CD, f_1, f_2 and f_3 as shown in Table 3 using the methodology described by Eq. (5).

Using the numerical results as reference, the relative error of the curve-fitted results can be calculated as equal to $ABS(V_{cf} - V_{Num})/V_{Num}$ and is smaller than 1.182E-3, as shown in Table 3 and Fig 16.

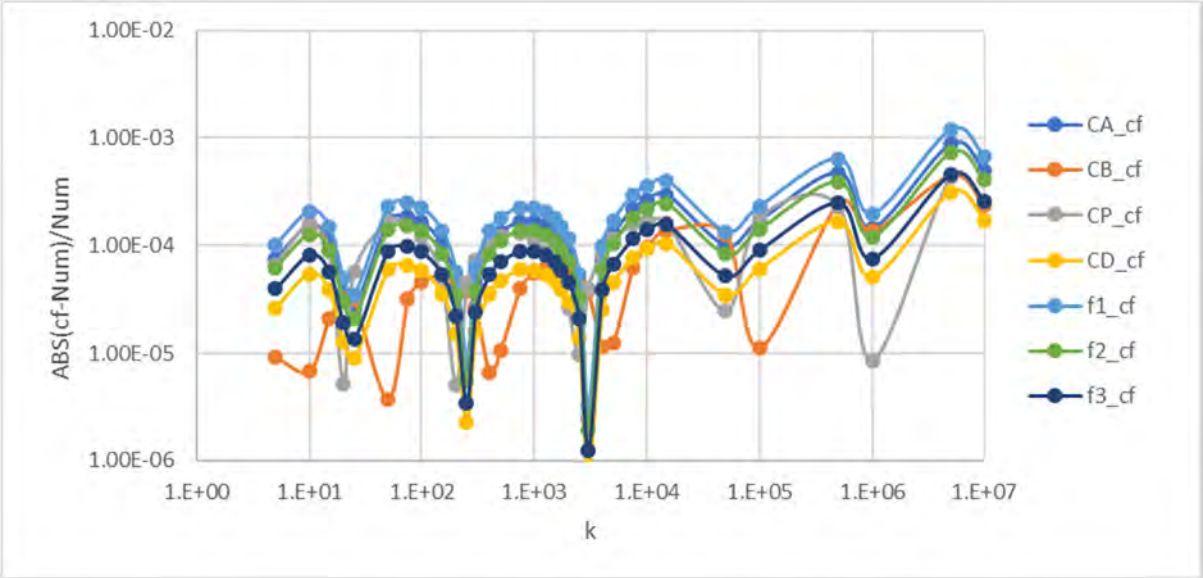

Figure 16: Accuracy of the curve-fitted results obtained using the very large k range.

The accuracy can be significantly improved (error < 6.49E-5) when limiting the maximum value of k to 15,000 (compatible with the maximum value of k found when studying cylindrical or needle roller bearing) as shown in Table 4.

A new through-hardenable high hardenability bearing steel designed by means of simultaneous optimisation of multiple responses using the desirability function approach

Mohamed Y. Sherif[1,*], Urszula Sachadel[1], Sébastien Blachère[1], Boris Minov[1], Manlio Becchetti[1], Ian Walker[1], Wijbe Buising[1]

[1]*SKF B.V., SKF Research and Technology Development, Meidoornkade 14, 3992 AE Houten, The Netherlands.*

[*]*Email: mohamed.sherif@skf.com*

Abstract– The current work presents a thermodynamics-based approach where the bearing steel alloy design was carried out such that several requirements, for instance high as-quenched hardness and minimum pearlite fraction, were optimised at once making use of inputs like a varying concentration of an alloying element. A solution as to the most desired composition space, or ranges, was thus demonstrated satisfying at once all outcomes being considered, instead of optimising each outcome separately.

Afterwards, the novel steel design characterised by reduced carbon content and with microalloying with vanadium, was verified by experimentally investigating a continuously cast industrial-scale melt *vs* a similarly produced heat of the reference 100CrMo7-3 steel.

In this work, the superiority of the new through-hardenable bearing steel in terms of hardenability, toughness, as well as resistance to white matter formation will be discussed in comparison with the reference steel. Furthermore, the results of rolling contact fatigue life testing of ACBB bearings will be presented. A suggestion as to future testing and potential implementation of the novel steel, henceforth called "SKF ToughTech", will be given.

Keywords – Alloy design, desirability function, bearing steel, large size bearings

1. Introduction

In the design phase, the newly designed steel alloy had to have the potential to exhibit high hardenability, that is, higher than the 100CrMo7-3 bearing steel. This is so the requirements of manufacturing large-size bearing rings could be met. Starting from the chemical composition of the 100CrMo7-3 steel, the concentration of several alloying elements such as carbon, chromium, silicon and molybdenum was optimised. In addition, microalloying with vanadium was carried out to arrive at the steel chemical composition presented in Table 1.

Table 1: The chemical composition of the vertically continuously cast steel concept, the SKF ToughTech. Heat no. 586200, DEW, Witten, Germany. Unless otherwise stated, the concentrations are in wt%. Hydrogen content was measured in the liquid steel. The balance is iron.

Chemische Zusammensetzung/ Chemical Composition/ Composition chimique

	C	Si	Mn	P	S	Cr	Mo	Ni	Cu	Sn	V	Al	As	
Ist/Actual/Actuel	0.80	0.36	0.79	0.011	0.001	1.55	0.37	0.12	0.09	0.004	0.09	0.026	0.004	[%]
	Ti	Ca	Pb	Sb	H2 ppm	O2 ppm								
Ist/Actual/Actuel	0.0013	< 0.0005	< 0.0010	< 0.0050	2.0	9								[%]

As can be seen in Table 1, carbon content was lowered to achieve higher hardenability without raising the martensite-start temperature (M_S) significantly, that is, for a given austenitisation condition. Too high a M_S temperature will render obtaining fine bainite (bainitic-ferrite) in the microstructure impossible, resulting in relatively softer microstructure.

It follows that, microalloying with vanadium proved indispensable to the SKF ToughTech steel design concept as austenitising at somewhat higher temperatures could easily be carried out to depress the M_S temperature without risking excessive austenite grain growth.

Another design consideration was the steel's suitability for continuous casting and to exhibit reduced segregation during solidification. To this end, both the Cr/C and Mo/Si ratios were aimed high, the former to ensure lower chromium segregation [1]. Meanwhile, the Mo/Si ratio was optimised to reduce the formation of segregation channels during solidification [2]. More details may be found in the patent application number WO 2016/083335 A1 [3].

2. Optimisation of the chemical composition

As already stated earlier, high hardenability is vital when it comes to manufacturing large size thick-walled bearing rings. A well-established experimental hardenability test is the Jominy or the end-quench test. The test can be executed in accordance with the test method in, for example, ASTM A255 – 10(2018) standard.

During the design of the SKF ToughTech steel, the expected hardenability performance of various steel compositions was predicted using the commercial software package JMatPro v 9.1. Using this software along with the thermodynamic database for steels, the Jominy or the end-quench test was simulated while varying only the carbon (0.4-1.6 wt%) and vanadium (0-2 wt%) contents of the SKF ToughTech steel shown in Table 1. A hypothetical austenitising temperature of 870 °C was selected, with an assumed prior austenite grain size (PAGS) of 15 µm. At this temperature the microstructure is composed of austenite and undissolved cementite. These conditions were chosen considering the experimental results gathered in an earlier work [2]. In total, 135 hypothetical alloys were calculated considering parameters such as HRC hardness, ferrite, pearlite, martensite and austenite fractions. These parameters were considered at certain distances along the length of the hypothetical bar as follows:

1- Adjacent to the quenched end (at a distance of 0.01 mm)
2- Mid-length (50 mm)
3- At the other end of the quenched bar (100 mm), which corresponds to the slowest cooling rate

For a 100 mm-long hypothetical quenched bar, two desirability functions were used depending on if a given simulation response was desired to be maximised (Eq. 1) or minimised (Eq. 2):

$$d_r^{max} = \begin{cases} 0 & if\ f_r(X) < A \\ \left(\dfrac{f_r(X) - A}{B - A}\right)^s & if\ A \le f_r(X) \le B \\ 1 & if\ f_r(X) > B \end{cases} \quad (1)$$

$$d_r^{min} = \begin{cases} 0 & if\ f_r(X) > B \\ \left(\dfrac{f_r(X) - B}{A - B}\right)^s & if\ A \le f_r(X) \le B \\ 1 & if\ f_r(X) < A \end{cases} \quad (2)$$

For every combination of vanadium and carbon content, and for every property calculated at a given distance from the quenched end, such as hardness (can also be called a response with an assigned function $f_r(X)$), a translation of the calculated values into a common scale of [0,1] was carried out using the response's individual or own desirability function. This process requires setting acceptance limits for every property calculated. The outcome of '0' is undesirable, and as will be shown, will inevitably eliminate the corresponding content of carbon and vanadium combination. The value of '1' means desirable, and fractions in between indicating somewhat acceptable values.

In total, 13 individual desirability functions were constructed, for five properties at three pre-selected positions along the simulated Jominy bar, each using the values presented in Table 2 for the limits A and B.

Table 2: The limits A and B for various properties at three locations. '-' not considered.

	Hardness, HRC	**Ferrite fraction**	**Pearlite fraction**	**Martensite fraction**	**Austenite fraction**
B & *A* at 0.01 mm	63.9 60.4	0.03 0.01	0.10 0.03	0.90 0.85	0.15 0.03
B & *A* at 50 mm	58.0 50.4	0.03 0.01	0.10 0.03	0.20 0.07	-
B & *A* at 100 mm	54.1 44.0	0.03 0.01	0.10 0.03	0.004 0.001	-
Scaling factor, *S*	0.5	0.5	1	0.5	1

It is important to mention that the desirability, rather obviously, is sensitive to the chosen limits. Therefore, such limits must make sense and be reasonable – using for example product/process acceptance limits.

Also, the importance of a property may be emphasised, such as in the current case, by analysing its responses at more than one location along the bar length, effectively assigning more weight to it. In addition, as will be discussed, the scaling factors may also be tuned.

The overall (or composite) desirability function (D) of the thirteen individual functions ($d_1 \ldots d_r$) was determined using the geometric mean as follows:

$$D = \left(\prod_{r=1}^{R} d_r\right)^{1/R} \quad (3)$$

where R equals 13. Therefore, the overall desirability can be seen in Figure 1.

The values for the thresholds A and B for the hardness calculated at 0.01 mm from the quenched end, for all combinations of carbon and vanadium contents, were 60.4 HRC (the average value of the population) and 63.9 HRC (the minimum of the top 10% of calculated values), respectively. S is the scaling factor, with a value of 0.5 for hardness, and is used to emphasise the importance of higher priority responses by rendering the calculated values within the limits A and B either easier or more difficult to yield higher desirability.

In this study, the scaling factors were varied resulting in either the enlargement or the contraction of the most

desired composition space presented in Figure 1 but never its disappearance and/or the emergence of a totally different region over the carbon and vanadium ranges under consideration. This suggested that a robust solution has been achieved, which could also be concluded due to the presence of a flattened top in the surface of the global desirability function, and not an isolated spike [4, 5].

According to the analyses, the optimised carbon content was centred at about 0.8 wt% with vanadium concentration of up to approximately 0.15 wt% (Figure 1). From the plot, it could be argued that a vanadium-free relatively low carbon variant (at 0.8 wt%) of the reference steel is desirable because of its expected higher hardenability. This is largely correct, however, the contribution of vanadium carbide precipitates to the bar hardness cannot be accounted for in JMatPro simulations, neither is the precipitate effect on refining prior austenite grains.

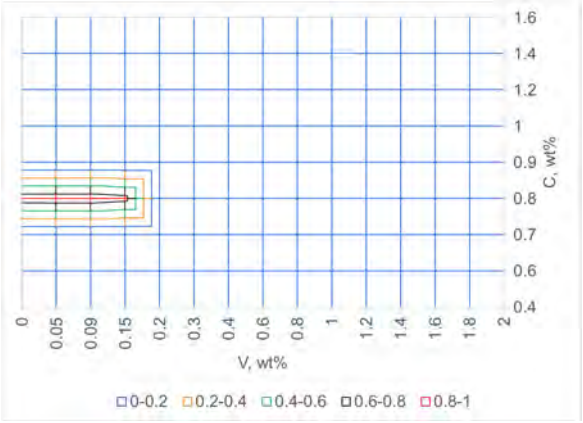

Figure 1: The overall desirability domains as a function of vanadium and carbon concentration in a hypothetical Jominy test steel bar quenched from 870 °C with assumed prior austenite grain size of 15 µm. The value of '1' stands for desirable and '0' undesirable. The balance of the chemical composition is that of the steel shown in Table 1. The calculated properties were HRC hardness and martensite fraction, both maximised, while ferrite, pearlite and austenite fractions were all minimised. The calculations were performed using JMatPro v 9.1.

3. Experimental results

3.1. Hardenability

Figure 2 exhibits Jominy curves of the SKF ToughTech steel along with other high hardenability bearing steels. All the tested bars had been normalised prior to testing in accordance with the ISO 642:1999 standard. The example shown in Figure 2 demonstrates that austenitising at 870 °C resulted in the SKF ToughTech steel clearly outperforming all but the 100CrMnMoSi8-4-6 bearing steel in terms of hardenability. Although not shown here, the somewhat lower hardness measured upon testing the SKF ToughTech steel, compared with the 100CrMnMoSi8-4-6 steel, appeared to diminish upon quenching from higher temperatures, for example, 890 °C [2].

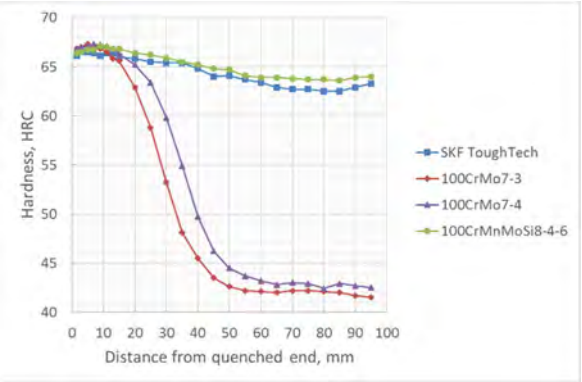

Figure 2: The Jominy curves of the SKF ToughTech steel vs other established high hardenability bearing steels. The austenitisation temperature was 870 °C. Tested according to ISO 642:1999.

In view of their hardenability being the highest, dilatometry testing was subsequently carried out to further assess the hardenability of both the SKF ToughTech and the 100CrMnMoSi8-4-6 bearing steels. A push-rod TA Instruments DIL805A/D/T dilatometer was used in the quenching mode. All dilatometer specimens were solid cylinders measuring 4 mm in diameter and 7 mm in length. SKF ToughTech steel specimens, however, were 10 mm long. The dilatometry work required that both steels were normalised and spheroidise-annealed prior to machining dilatometer specimens, which were subsequently used to construct continuous cooling transformation (CCT) diagrams austenitising at 870 °C (70 min soak) and at 885 °C (120 min soak). In all instances, the cooling to the temperature of 100 °C was of the Newtonian type with preset t8/5 times. Figure 3 shows the microstructures of the steels prior to the dilatometry work.

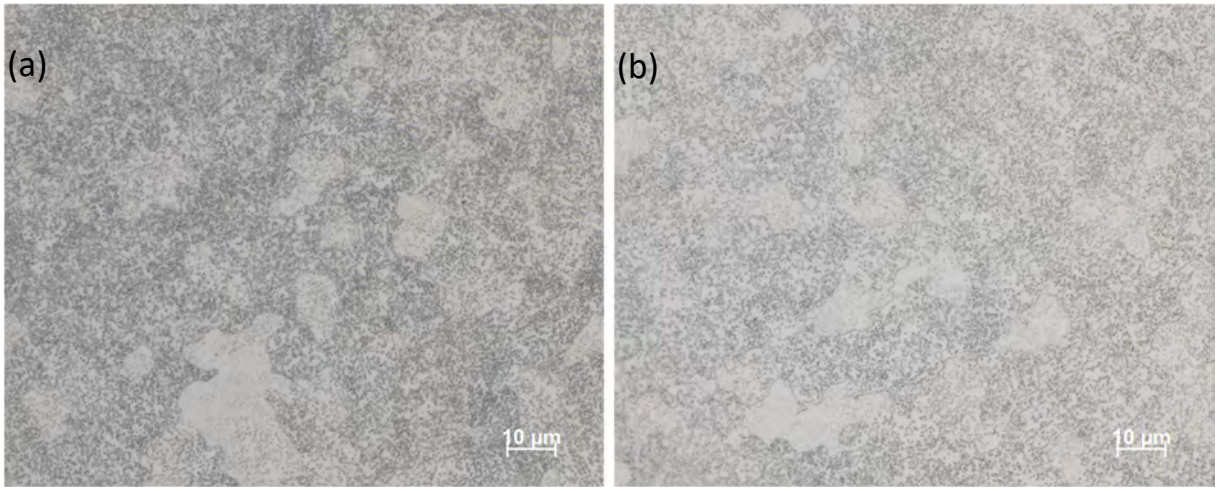

Figure 3: The normalised and spheroidise-annealed microstructures of the dilatometer specimens of (a) the SKF ToughTech steel and (b) steel 100CrMnMoSi8-4-6. Images were taken at the centre of the specimen. The rolling direction is horizontal.

t8/5, s	25	100	200	300	500	800	1200	1600	2400
HV10	828	819	813	790	696	484	445	415	363
±	1.8	3.3	4.3	4.7	13	6.5	3.3	2.8	3.7

Table 3: The measured hardness of SKF ToughTech steel dilatometer specimens as a result of increasing the cooling time between 800 °C and 500 °C. Austenitised at 870 °C for 70 min.

t8/5, s	25	100	200	300	500	800	1200	1600	2400
HV10	833	820	819	789	702	548	442	393	345
±	1.1	2.9	4.2	1.6	9.5	8.6	2.9	2.7	2.2

Table 4: The measured hardness of 100CrMnMoSi8-4-6 steel dilatometer specimens as a result of increasing the cooling time between 800 °C and 500 °C. Austenitised at 870 °C for 70 min.

As can be seen in Figure 4, the CCT diagrams of both the SKF ToughTech and the 100CrMnMoSi8-4-6 steel were quite indistinguishable upon austenitising at 870 °C for 70 min. Note the high hardenability of both steels manifested by the need to cool by t8/5 of 2400 s so that fully pearlitic microstructures could be obtained.

The hardness measured for both steels' specimens can be seen in Table 3 and Table 4. Again, the two steels appeared to show approximately the same hardness after specimens were quenched with the fastest cooling between t8/5 of 25 s and 500 s. On the specimens cooled by t8/5 of 800 s, the 100CrMnMoSi8-4-6 steel specimen had clearly higher hardness. However, the hardness was approximately the same when the specimens were cooled by t8/5 of 1200 s. Nevertheless, cooling by the two slowest rates, the SKF ToughTech steel specimens showed higher hardness than that measured on the 100CrMnMoSi8-4-6 steel specimens.

As shown in Figure 5, the SKF ToughTech steel specimen cooled by t8/5 of 500 s appeared to contain somewhat less slack-quench phases in its microstructure, that is, compared with the 100CrMnMoSi8-4-6 steel specimen austenitised and cooled in the same manner. Most important perhaps is that, unlike the case with the SKF ToughTech steel, the 100CrMnMoSi8-4-6 steel specimen showed several prior austenite grain boundaries delineated by the formation of upper bainite. The presence of this phase might reduce the strength at the grain boundaries.

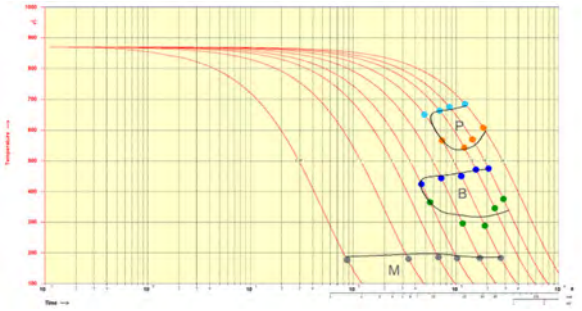

Figure 4: The CCT diagrams of the SKF ToughTech steel (lines) vs the steel 100CrMnMoSi8-4-6 (dots) quenching from 870 °C after soaking for 70 min at temperature. "P" denotes pearlite; "B" bainite and "M" martensite. The measured hardness can be seen in Table 3 and Table 4.

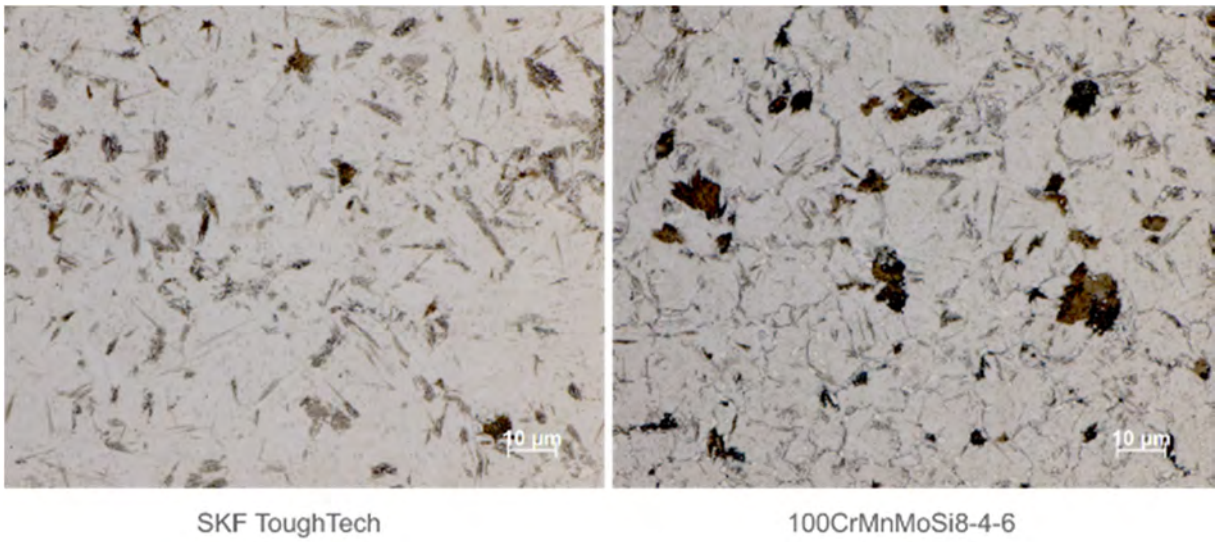

Figure 5: The microstructure of the steels cooled by t8/5 of 500 s after austenitisation at 870 °C for 70 min. Images were taken at the centre of the specimen. The rolling direction is horizontal.

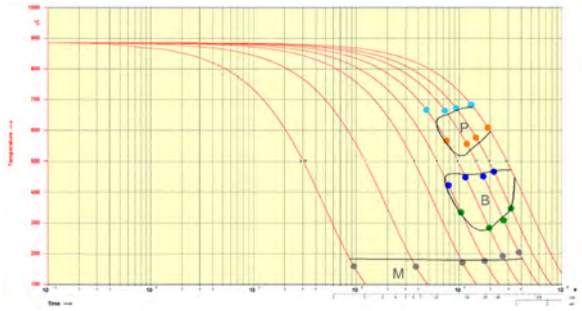

Figure 6: The CCT diagrams of the SKF ToughTech steel (lines) vs the steel 100CrMnMoSi8-4-6 (dots) quenching from 885 °C after soaking for 120 min at temperature. "P" denotes pearlite; "B" bainite and "M" martensite. The measured hardness can be seen in Table 5 and Table 6.

t8/5, s	25	100	300	500	800	1200	1600	2400
HV10	852	832	831	783	578	491	446	394
±	2.9	2.8	6.9	6.1	8.3	2.2	4.2	3.6

Table 5: The measured hardness of SKF ToughTech steel dilatometer specimens as a result of increasing the cooling time between 800 °C and 500 °C. Austenitised at 885 °C for 120 min.

t8/5, s	25	100	300	500	800	1200	1600	2400
HV10	828	831	804	759	596	474	420	362
±	2.4	4.5	1.2	5.8	8.6	5.1	6.5	1.9

Table 6: The measured hardness of 100CrMnMoSi8-4-6 steel dilatometer specimens as a result of increasing the cooling time between 800 °C and 500 °C. Austenitised at 885 °C for 120 min.

When the austenitisation temperature was raised to 885 °C with prolonged soaking time of 120 min, there appeared some differences between the two steels once cooled (Figure 6). At the fastest cooling rates, the M_S temperature was more depressed for the 100CrMnMoSi8-4-6 steel, presumably due to its higher carbon content which most likely raises its austenite concentration of carbon as well. Also, the 100CrMnMoSi8-4-6 steel appeared to show higher tendency for the formation of pearlite as its nose was somewhat shifted upwards and slightly to the left, to shorter times, compared with the SKF ToughTech steel. At t8/5 of 2400 s, no bainite was detected in the 100CrMnMoSi8-4-6 steel specimen, unlike the case with the SKF ToughTech steel specimen. Accordingly, it could be concluded that the SKF ToughTech steel showed higher hardenability austenitised at 885 °C for 120 min. Table 5 and Table 6 show the hardness of the as-quenched specimens from both steels. It is difficult to discern much from the difference in hardness between the two groups of specimens cooled the fastest as this most probably is complicated by the presence of higher amount of residual austenite compared with the case austenitising at 870 °C for 70 min. However, upon cooling by t8/5 of 500 s and up to 2400 s, except when cooled by t8/5 time of 800 s, the SKF ToughTech steel specimens showed higher hardness compared with the 100CrMnMoSi8-4-6 steel specimens. Figure 7 shows the microstructure of two specimens from both steels cooled by t8/5 of 500 s. The same observations mentioned regarding the micrographs shown in Figure 5 could also be extended here for the images in Figure 7. However, it appeared that raising the austenitisation temperature with prolonged soaking time at temperature did not result in a significant increase in hardenability of the 100CrMnMoSi8-4-6 steel. Even though austenitising at higher temperatures causes more alloying elements which increase hardenability to be in solid solution in the austenitic matrix, such as molybdenum and chromium, the austenite will also dissolve more carbon, the latter reduces hardenability for hypereutectoid steels [6].

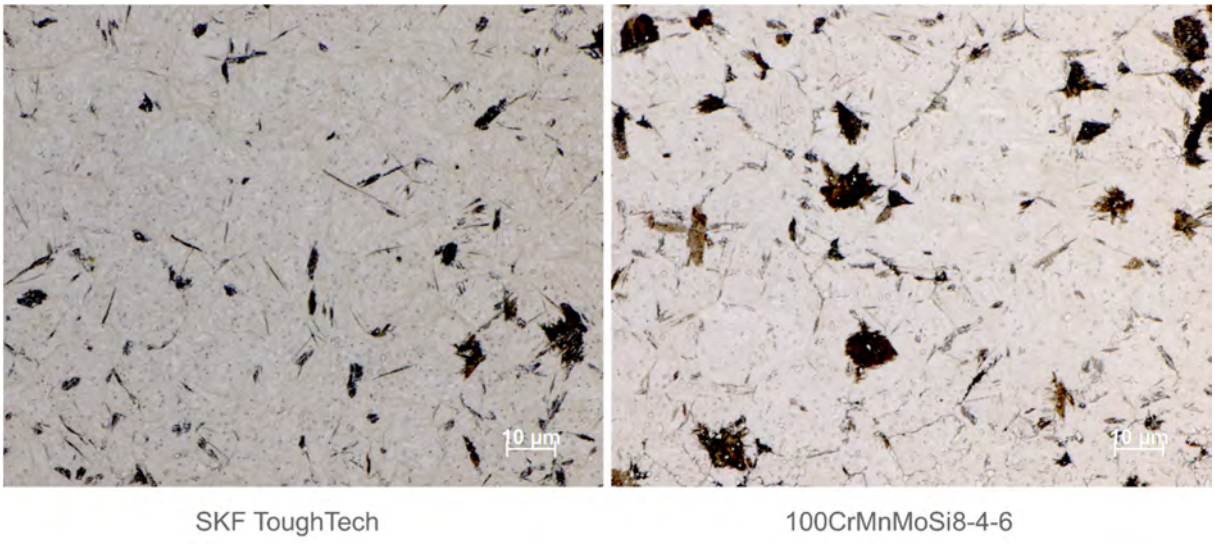

Figure 7: The microstructure of the steels cooled by t8/5 of 500 s after austenitisation at 885 °C for 120 min. Images were taken at the centre of the specimen. The rolling direction is horizontal.

3.2. K_{Ic} toughness

Figure 8 shows the obtained linear-elastic plane-strain fracture toughness K_{Ic} of the SKF ToughTech steel compared with the steel 100CrMo7-3 according to ASTM E399. Figure 8 shows higher average K_{Ic} toughness for the SKF ToughTech steel specimens compared with the 100CrMo7-3 steel counterparts, both transformed into bainite with the same hardness prior to the test.

3.3. Life testing

In addition, life tests using angular contact BAH-0012 AD bearings were carried out using one inner ring per bearing which was soft-turned then bainitically hardened without prior hot-forging. The remainder of the bearing elements, including the other inner ring, were standard components. Soft-turning from bar was executed so the properties of the SKF ToughTech steel and the reference 100CrMo7-3 bearing steel may be determined.

The Ø 120 mm round hot-rolled black bars had area reduction ratio of 14.3:1. Afterwards, the bars had been normalised then spheroidise-annealed by the steel supplier prior to soft-turning of the bearing rings. The micro-cleanliness level measured for both steels according to the ISO 4967, method A, may be seen in

Table 7 and Table 8. For both steels the micro-cleanliness is within the limits described in the ISO 683-17 and the results for both steels are not significantly different.

Life testing was carried out under pure axial load resulting in C/P of 1 and with kappa value of 3. The test speed was 6000 rpm and the temperature of the test oil was 70 °C. Figure 10 shows an example schematic drawing of SKF type 2 test rig used for rolling bearing fatigue experiments, along with an overview picture of a battery of test rigs. BAH-0012 AD bearing tests were carried out on the same rig whilst only applying axial load.

Figure 9 presents the Weibull probability plot with normalised life of all bearing inner ring sub-surface failures of both steel types while Figure 11 exhibits the re-analysis considering only the data points that influence the L_{10} value. Although with a different Weibull slope, the L_{10} performance of the SKF ToughTech steel variant showed a statistically significant increase in the L_{10} value compared with that of the 100CrMo7-3 steel variant, with A-Trunc, the latter being a proprietary SKF test analysis methodology.

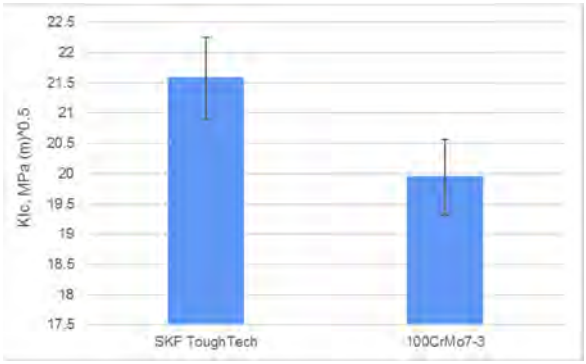

Figure 8: K_{Ic} toughness of single-step bainite transformed specimens with the same hardness.

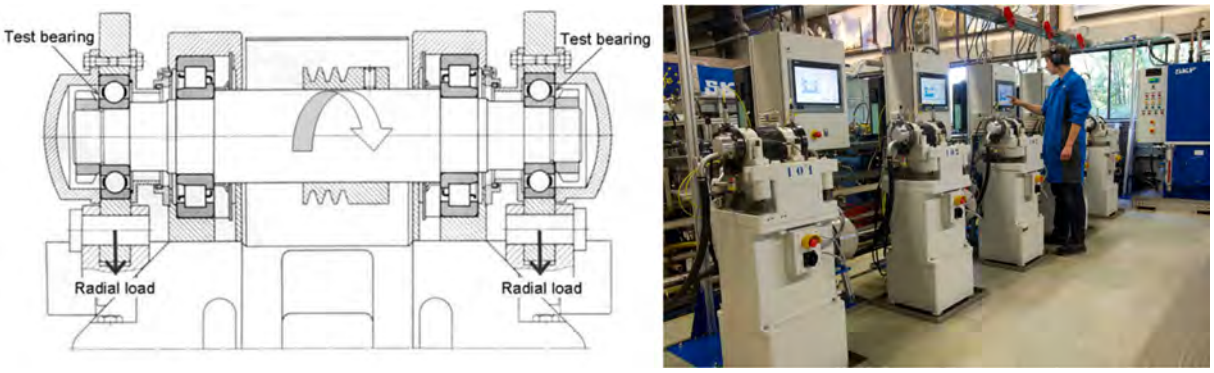

Figure 10: Left: a drawing of an example bearing life test rig; Right: a picture showing a battery of bearing test rigs.

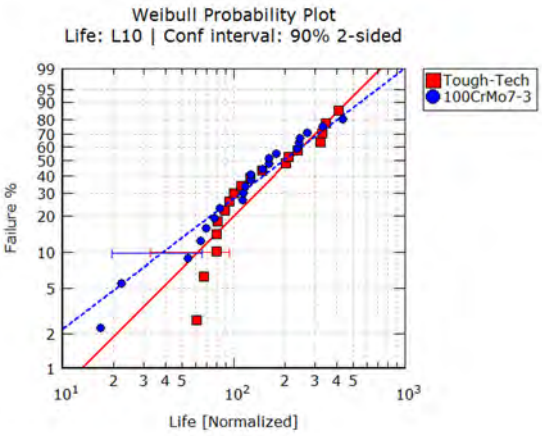

Figure 9: Weibull Plot with normalised life of the SKF ToughTech steel and the 100CrMo7-3 steel inner rings sub-surface failures.

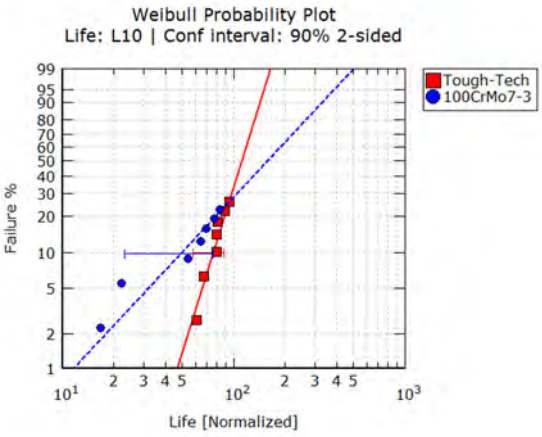

Figure 11: Weibull Plot with normalised life of the SKF ToughTech steel and the 100CrMo7-3 steel inner rings sub-surface failures applying the "A-Trunc" methodology.

Table 7: 100CrMo7-3, Ø 120 mm, DEW, heat no. 579260.

Specimen code	Type A		Type B		Type C		Type D		Type DS
	Fine	Thick	Fine	Thick	Fine	Thick	Fine	Thick	
1	0.0	0.0	1.0	0.0	0.0	0.0	0.5	0.5	1.0
2	0.5	0.0	1.0	0.5	0.0	0.0	1.0	0.5	1.0
3	0.5	0.0	1.0	0.5	0.0	0.0	1.0	0.5	1.0
4	0.5	0.0	1.0	1.5	0.0	0.0	1.0	0.5	1.0
5	0.5	0.0	1.0	0.0	0.0	0.0	1.0	0.5	0.5
6	0.5	0.0	1.0	0.5	0.0	0.0	1.0	0.5	1.0
Average	**0.4**	**0.0**	**1.0**	**0.5**	**0.0**	**0.0**	**0.9**	**0.5**	**0.9**
ISO 683-17 limits	**2.5**	**1.5**	**2.0**	**1.0**	**0.5**	**0.5**	**1.0**	**1.0**	**2.0**

Table 8: SKF ToughTech, Ø 120 mm, DEW, heat no. 586200.

Specimen code	Type A		Type B		Type C		Type D		Type DS
	Fine	Thick	Fine	Thick	Fine	Thick	Fine	Thick	
1	0.0	0.0	1.0	0.5	0.0	0.0	1.0	0.5	0.5
2	0.5	0.0	1.0	0.5	0.0	0.0	0.5	0.5	0.5
3	0.5	0.0	0,5	0.5	0.0	0.0	1.0	0.5	0.5
4	0.0	0.0	1.0	0.5	0.0	0.0	0.5	0.5	0.5
5	0.0	0.0	1.0	0.5	0.0	0.0	0.5	0.5	1.0
6	0.5	0.0	1.0	0.5	0.0	0.0	1.0	0.5	1.0
Average	**0.2**	**0.0**	**0.9**	**0.5**	**0.0**	**0.0**	**0.7**	**0.5**	**0.7**
ISO 683-17 limits	**2.5**	**1.5**	**2.0**	**1.0**	**0.5**	**0.5**	**1.0**	**1.0**	**2.0**

Table 9: A partial list of post-test failure analyses carried out on life-tested SKF ToughTech and 100CrMo7-3 bainitic bearing inner rings. "DER" denotes dark-etching region; "LAB" low-angle band; "HAB" high-angle band and "WEC" white-etching crack.

Ring no.	Steel	DER	LABs	HABs	WECs	Butterflies	Remarks
76	100CrMo7-3	No	No	No	Yes	Yes	WEM around spall or crack
119		Yes	No	No	No	Yes	NO WEM around spall or crack
101		Yes	No	No	No	Yes	WEM around spall or crack
100		Not clear	No	No	Yes	No	WEM around spall or crack
81		Yes	No	No	No	No	WEM around spall or crack
111		Yes	No	No	No	No	WEM around spall or crack
94		Yes	No	No	No	No	WEM around spall or crack
127	SKF ToughTech	Yes	No	No	No	No	NO WEM around spall or crack
21		Yes	No	No	No	Yes	WEM around spall or crack
72		Yes	No	No	No	No	NO WEM around spall or crack
10		Yes	No	No	No	No	NO WEM around spall or crack
3		Yes	No	No	Yes	No	NO WEM around spall or crack
117		Yes	No	No	No	No	NO WEM around spall or crack

Bearing performance is conventionally measured via the L_{10}, 90% reliability time or number of cycles, of the life distribution. From test data, it is possible to derive an estimation of the L_{10}, providing the life distribution corresponds to a 2 parameters Weibull distribution. Nevertheless, evidence [7] shown that the full life distribution may deviate from the assumed 2 parameters Weibull at high or lower reliability levels.

To prevent such deviation altering the L_{10} estimation, in case of test with a high proportion of failures, the late failure and suspension times may need to be truncated. Doing so, no data is discarded, only the part of the information that does not bring information of the desired target (L_{10}) is reduced. That method was used on the present test data where all failures and suspensions later than the 7th failure are truncated at this time. The data are then the same as if the test would have been stopped when reaching the 7th failure. The resulting analysis shows a better fit with the failure times around the L_{10}.

3.4. Resistance to white-matter formation

Post life-test failure analyses showed more resistance to white-etching matter (WEM) formation in the SKF ToughTech steel rings, compared with the reference steel in the test (

Table 9). An example of WEM can be seen in Figure 12.

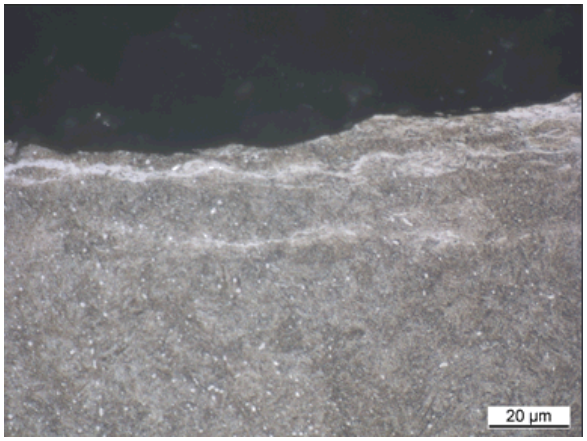

Figure 12: The extent of sub-surface damage with white-etching matter clearly visible on a life-tested 100CrMo7-3 bearing ring.

4. Conclusions

The following points may be summarised:

1- A new bearing steel concept (SKF ToughTech) has been successfully designed that is through-hardenable and particularly suits large thick-walled bearing rings/components in virtue of its high hardenability. Compared with the 100CrMo7-3 bearing steel chemical composition, the SKF ToughTech steel is characterised by lower carbon content with the microalloying addition of vanadium
2- As per design, the SKF ToughTech steel demonstrated hardenability higher than that of the well-established 100CrMnMoSi8-4-6 bearing steel, when austenitised at 885 °C for 120 min at temperature
3- The SKF ToughTech steel demonstrated good and somewhat higher K_{Ic} bainite toughness, compared with similarly produced test components manufactured from the 100CrMo7-3 bearing steel
4- The preliminary L_{10} performance of the SKF ToughTech steel variant showed a statistically significant increase in the L_{10} value compared with that of the 100CrMo7-3 bearing steel variant with A-Trunc, a proprietary SKF test analysis methodology. That said, further life tests are recommended while reducing the level of hoop stress, for two reasons. Firstly, in view of the inherent difference between SKF ToughTech and 100CrMo7-3 steels in terms of the number density of carbides in the microstructure. Secondly, noting that the bearing rings were soft-turned, not hot-forged, it is expected that they are more sensitive to the levels of hoop stress usually applied when testing bainitic-hardened rings
5- Compared with the reference 100CrMo7-3 bearing steel bainitically hardened, the SKF ToughTech steel appeared more resistant to white-matter formation

For future work, large bearing rings should be manufactured such that the SKF ToughTech steel could then be put to test under conditions closer to those experienced in applications requiring such bearing sizes.

Acknowledgements

The authors wish to thank Deutsche Edelstahlwerke (DEW), Witten, Germany, for their help and commitment during the manufacturing of the continuously cast steels used in this study.

References

[1] Kozeschnik, E., 2000, "A Scheil-Gulliver model with back–diffusion applied to the microsegregation of chromium in Fe-Cr-C alloys," Metall. Mater. Trans. A, 31A, pp. 1682-1684.

[2] Sherif, M. Y., Sachadel, U., Kerrigan, A., Minov, B., Huang, H., Paape, I., Gerritzen, R., 2017, Bearing Steel Technologies: 11th Volume, Progress in Steel Technologies and Bearing Steel Quality Assurance, ASTM STP1600, J. M. Beswick, Ed., ASTM International, West Conshohocken, PA, pp. 296-322.

[3] Sherif, M. Y., Sachadel, U., 2016, "Bearing component formed from a steel alloy," International Patent Application no. PCT/EP2015/077436, publication number WO 2016/083335 A1.

[4] Karatapanis, A. E., Fiamegos, Y. C., Sakkas, V. A., Stalikas, C. D., 2011, "Effect of chromatographic parameters and detector settings on the response of HILIC–evaporative light-scattering detection system using experimental design approach and multicriteria optimization methodology," Talanta, 83, pp. 1126-1133.

[5] Candioti, L. V., De Zan, M. M., Cámara, M. S., Goicoechea, H. C., 2014, "Experimental design and multiple response optimization. Using the desirability function in analytical methods development," Talanta, 124, pp. 123-138.

[6] Jatczak, C. F., 1973, "Hardenability in high carbon steels," Metall. Trans., 4, pp. 2267-2277.

[7] Tallian, T., 1962, "Weibull Distribution of Rolling Contact Fatigue Life and Deviations Therefrom," *ASLE transaction ,* vol. 5, pp. 183-196.

Starved Lubrication in Rolling Contacts-A Review

Gerhard Poll[1], Xinming Li[2], Norbert Bader[1], Feng Guo[2]

[1] *Institute of Machine Design and Tribology, Leibniz University Hannover, poll@imkt.uni-hannover.de*

[2] *School of Mechanical and Automotive Engineering, Qingdao University of Technology, mexinmingli@163.com*

Abstract– Starvation is frequently encountered in rolling element bearings. The occurrence of starvation inhibits the generation of pressure and hence results in reduction in film thickness. On the other hand, starvation is helpful to suppress rolling friction and gross skidding of rolling bearings. This paper reviews some typical issues related to starvation such as the generation mechanism of starvation, starvation criteria, lubricant replenishment, starved grease lubrication and starved contacts with restricted oil feeding. The model of feed-loss balance determining the starvation state in both model tests and full bearing tests is discussed. This paper may be useful for understanding and controlling starvation in rolling contacts.

Keywords – starvation; rolling contacts; elastohydrodynamic lubrication; grease lubrication; replenishment

1. Introduction

In rolling element bearings, the contacts between rolling elements and raceways are lubricated by elastohydrodynamic lubrication (EHL) films. Basically, the formation of EHL films is determined by the physical parameters at the inlet zone [1, 2] such as lubricant viscosity, speed and inlet geometry. Given these parameters under sufficient lubricant supply, film thickness can be well predicted with simple film thickness formulas [3-5]. Under fully flooded state, the inlet gap is completely filled and the film thickness will no longer rise with increasing lubricant amount, whilst churning losses may continue to grow. However, if the inlet gap is partially filled, the initial point of pressure formation is shifted closer to the edge of the Hertzian contact. This results in the hydrodynamic effect playing a role in a more restricted area and thus in a reduction in film thickness, a situation which is known as starvation. Unlike under fully flooded conditions, EHL films in starved contacts will be sensitive to the conditions of inlet lubricant supply which are closely related to running speed, lubricant viscosity and lubricant feeding methods. For instance, starvation is prone to be encountered in rolling bearings running at high speeds [6], lubricated by grease [7], with restricted lubricant feeding by oil mist [8] or oil-air [9] lubrication, or operating at low temperatures [10-12]. The presence of starvation may eventually force the contacts into a severe situation where asperity contacts will take place and the risk of failure e.g. by scuffing increases.

On the other hand, a restricted lubricant supply to the inlet zone will inhibit reverse flow and subsequently reduce rolling friction [13]. As Baly [14] observed in grease lubricated bearing tests, the variations of friction torque against speed exhibited a regime where the values were relatively lower. Correspondingly, the film thicknesses at the same speed range were lower as well, which was believed to be caused by starvation. This suggests that moderate starvation can be helpful in reducing bearing friction. In addition, the reduced film thickness will result in a higher traction to suppress the gross skidding [15]. Therefore, from the aspects of suppression in friction torque and gross skidding, partial starvation may be beneficial to bearing lubrication.

Lubricant starvation in EHL rolling contacts has attracted attention since the 1960's. Over the past decades, persistently studies on starvation were conducted. In this paper, some typical work related to starvation such as the generation mechanism of starvation, starvation criteria, lubricant replenishment, model and full bearing tests of starvation and others will be reviewed. This work may be beneficial to better understanding of the mechanisms of starvation.

2. Generation mechanism of starvation

According to the Ertel-Grubin [1, 2] theory, the EHL lubricating films are mainly developed in the inlet region. As shown in Figure 1, in fully flooded EHL contacts, the inlet convergent gap is fully filled by lubricant. The pressure will initially build up at an infinite position far away from the edge of the Hertzian contact region. For a given inlet gap geometry, by inputting the dimensionless parameters of loading, speed and solid material, the film thickness can be obtained through film formulas [3-5]. However, if the lubricant amount is not sufficient to fill the whole gap, the pressure will start to develop at a limited distance from the edge, resulting in a starved contact. Under starvation conditions, characterized by the appearance of an oil-air meniscus ahead of the contact, film thickness will also be a function of the oil amount supplied to the inlet. That means, inlet lubricant supply is an additional input parameter. One of the methods to describe this parameter is the inlet distance S from the oil-air boundary to the contact edge [16], as shown in Figure 1. It should be noted that pressure formation starts right at the position of the oil-air meniscus. It is apparent that the closer the meniscus approaches the contact, the thinner the film thickness and the greater the degree of starvation. Therefore, the inlet oil supply condition is a crucial parameter determining film formation.

During bearing operation, lubricant on the track is displaced to both sides by the rolling elements due to successive passages. Partial lubricant attached on the boundary surfaces (h_{disc} and h_{ball} in Fig.1) in

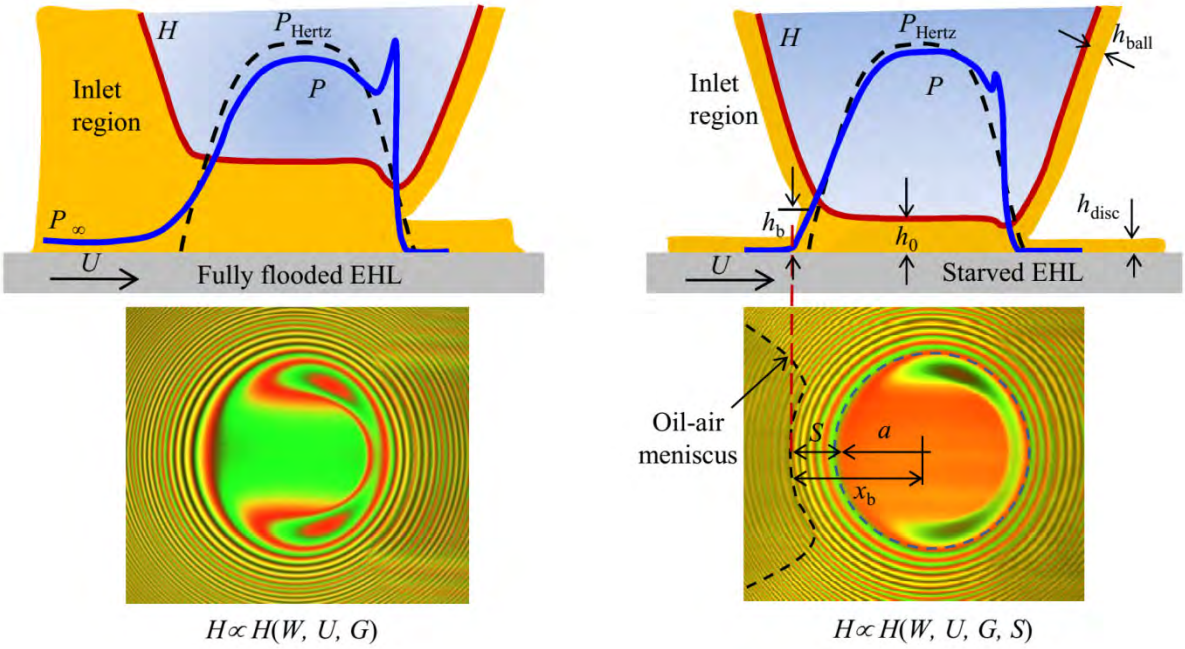

Figure 1: Fully flooded EHL and starved EHL

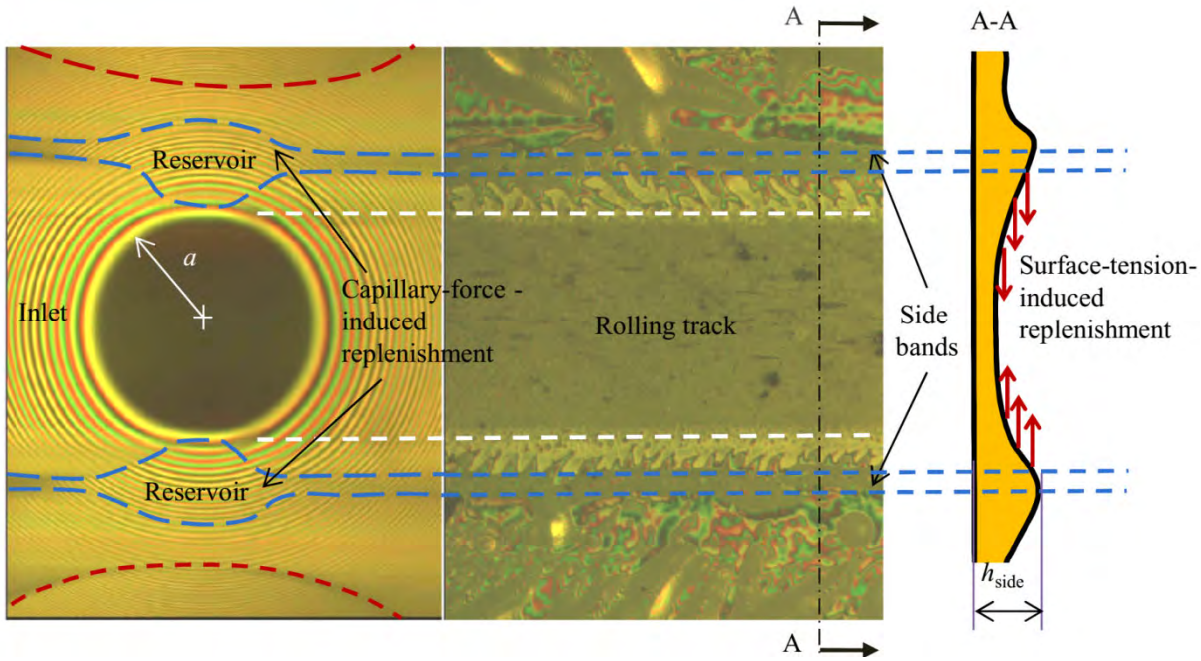

Figure 2: Equilibrium films and replenishment mechanisms (Greased contacts)

combination with the replenished lubricant, will converge at the inlet zone. The total lubricant amount determines the inlet boundary. In principle, the displaced lubricant in the side bands [17] (in Figure 2), should flow back to the rolling track due to a surface tension gradient [18]. The reflow amount of lubricant from the side bands can be predicted from a formula proposed by Chiu

$$\Delta\zeta = \frac{C_0 \gamma_{OA}}{2\eta_0} t \qquad (Eq.\ 1)$$

C_0 is a factor obtained from a computation depending on the ratio of the contact radius a and the height of the ridges h_{side}. γ_{OA} denotes the surface tension at the oil-air interface and t is the time interval between successive rolling element passages. It is clear that at high speeds the time interval will be so short that the replenishment will be dramatically reduced. A similar situation occurs if the lubricant viscosity η_0 is too high, e.g., when the lubricant, especially grease, operates at low temperatures. The parameter of h_{side} is usually determined by the amount of (external) lubricant charging. h_{side} will be much lower under restricted oil feeding (e.g., oil mist or oil-air lubrication). Therefore, at high speed, highly viscous oil and/or restricted oil feeding conditions, the lubricant amount available will be less than necessary to form a full EHL film, Although lubricant replenishment induced by capillary force contributes to the formation of side reservoirs [19], it only

plays a local role. In essence, the degree of starvation is determined by the balance between the loss of bulk lubricant from the track and the lubricant replenishment adjacent to the track.

3. Starvation criteria

To quantitatively assess the onset and the degree of starvation, different criteria have been defined to correlate the inlet conditions with the film thickness.

3.1. Inlet distance

The features of starved EHL contacts were first observed visually by Wedeven [16] via optical interferometry. Wedeven linked the inlet boundaries to the reduction in film thickness by defining the inlet distance S as shown in Fig. 1, which can be expressed as

$$S = \left(\frac{h_b/h_0 - 1}{1.21} \right)^{2/3} \frac{(Rh_0)^{2/3}}{a^{1/3}} \qquad (Eq.\ 2)$$

The variables of S, h_b, h_0 and a are also presented in Fig. 1. Equation (2) indicates that the central film thickness is a function of the position of the inlet meniscus. As the inlet meniscus approaches the Hertzian contact circle, the film thickness will decrease. In terms of the experimental data, Wedeven found that $h_b/h_0 \approx 9$ is the critical condition for the onset of starvation. Furthermore, Wedeven provided a semi-empirical formula to predict the starved EHL film thickness

$$\frac{h_0}{R} = 1.73 \left[\frac{S}{S_f} \left(2 - \frac{S}{S_f} \right) \right]^{1/2} \left(\frac{\alpha \eta_0 u_e}{R} \right)^{5/7} \left(\frac{w}{E'R^2} \right)^{-1/21} \qquad (Eq.\ 3)$$

Using inlet distance as input parameter, Hamrock and Dowson [20] numerically solved the starvation problem. The critical dimensionless inlet distances m^* are expressed as

$$m^* = 1 + 3.06 \left[\left(\frac{R_x}{b} \right)^2 H_{c,F} \right]^{0.58} \qquad (Eq.\ 4)$$

$$m^* = 1 + 3.34 \left[\left(\frac{R_x}{b} \right)^2 H_{\min,F} \right]^{0.56} \qquad (Eq.\ 5)$$

where $H_{c,F}$ and $H_{min,F}$ denote the dimensionless central and minimum film thickness under fully flooded states. Beginning from a dimensionless inlet distance $m \le m^*$, lubricant starvation will occur. By means of the least-square curve fit method, the relationships between starved film thickness and that of fully flooded film thickness are defined as

$$H_{c,S} = H_{c,F} \left(\frac{m-1}{m^*-1} \right)^{0.29} \qquad (Eq.\ 6)$$

$$H_{\min,S} = H_{\min,F} \left(\frac{m-1}{m^*-1} \right)^{0.25} \qquad (Eq.\ 7)$$

where $H_{c,S}$ and $H_{min,S}$ denote the central and minimum film thickness under starved conditions.

Although the inlet distance is a simple and direct criterion to describe the degree of starvation, the limitation is that the value of inlet distance is difficult to determine in practice. Also, the assumption of straight inlet boundaries does not match the experimental observations. Moreover, when the inlet boundary reaches the contact edge, numerical predictions will become not available, limiting the utilization of this criterion to moderate starvation conditions.

3.2. Inlet free boundary layer

Actually, in reality the inlet boundary is a free boundary. A new criterion considering free boundary conditions was developed by Chevalier [21] based on Elrod's theoretical work [22, 23]. The main idea is to define a fractional film content θ which represents the ratio between the film thickness of the inlet oil layer h_{oil} and the gap height h. The complementarity conditions are set as: $0 \le \theta \le 1$, $p = 0$ (starved part of the inlet zone), or $\theta = 0$, $p > 0$ (fully flooded part of the inlet zone). A modified Reynolds equation used for starvation is expressed as

$$\frac{\partial}{\partial x}\left(\frac{\rho h^3}{12\eta} \frac{\partial p}{\partial x} \right) + \frac{\partial}{\partial y}\left(\frac{\rho h^3}{12\eta} \frac{\partial p}{\partial y} \right) = u_e \frac{\partial(\theta \rho h)}{\partial x} + \frac{\partial(\theta \rho h)}{\partial t} \qquad (Eq.\ 8)$$

Thus the inlet boundaries can be determined automatically by calculations. Both the shape and location of the inlet meniscus can be controlled. Using this method, Chevalier [21] investigated the features of starved EHL films by setting different distributions of inlet layers such as a constant oil layer or a harmonic oil layer.

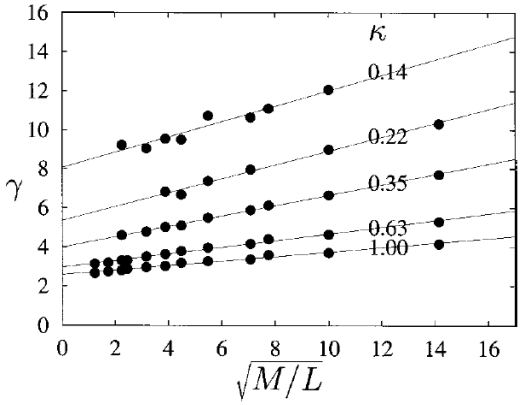

Figure 3: γ as a function of $\sqrt{M/L}$ for different ellipticities: $\sqrt{M/L} = 0.14, 0.22, 0.35, 0.63, 1.00$, $r \approx 1$ [25]

To link the evolutions of inlet layer and EHL films to the number of overrollings, Chevalier [24] introduced a parameter γ to reflect the resistance against side flow. The relation between film thickness reduction and oil layer available is established as

$$\Re = \frac{r}{\sqrt[\gamma]{1 + r^\gamma}} \qquad (Eq.\ 9)$$

where $\Re = H_c/H_{cff}$ denotes the dimensionless film thickness reduction, while $r = H_{oil}/\bar{\rho} H_{cff}$ denotes the dimensionless oil thickness on the track. It is then possible to evaluate the film decay with the number of passes n under the assumption of $r(n) = \Re(n\text{-}1)$. Thus, $\Re(n)$ can be written as

$$\Re(n) = \frac{1}{\sqrt[\gamma]{1/r_0^\gamma + n}}, \quad \lim_{n \to \infty} \Re(n) = n^{-1/\gamma} \qquad (Eq.\ 10)$$

The parameter γ is determined experimentally or can be numerically obtained from plots of $\Re(n) = f(n)$. Later, Damiens [25] obtained the parameter γ for different operating conditions. The influence of ellipticity κ on the values of γ was also studied. Figure 3 shows the variations of γ with $\sqrt{M/L}$, indicating the increase in γ with $\sqrt{M/L}$ decreasing.

Obviously, this criterion describes a precise geometry of the inlet meniscus and the starvation degree is physically determined.

3.3. Free surface thin layer flow

In rolling bearings, there are many factors such as cage effects and centrifugal forces affecting the distribution of the lubricant layer on the races. Van Zoelen et al. [26] developed a free surface thin layer flow model using axisymmetric rotating surfaces. The effects of centrifugal forces on the surface flow of an oil layer were analyzed in relation to the geometry of the raceway. The general trend of layer decay under centrifugal effects was accurately predicted. The film thickness inside the starved EHL contacts was directly related to the distribution of the layer on the track. Based on this model, Van Zoelen et al. [27] developed an improved model to predict the contact pressure-induced film thickness decay for long-term operation without replenishment [28]. A central film formula was obtained to predict the decay of starved film thickness. One feature of this model is that the reduction of film thickness is a function of time, whereas according to the Chevalier-Damien model it is a function of number of rolling element passages n. Moreover, it can accurately predict the decay rate for small values of $r(n)$.

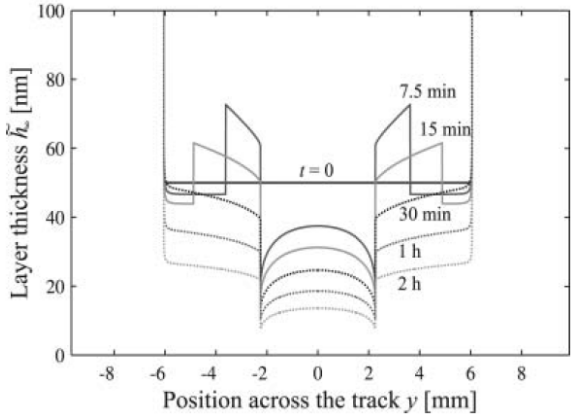

Figure 4: Layer variation across track at different times for roller bearing 22317 [29]

Extended work was carried out by Van Zoelen [29] to model the oil loss from the track in a complete bearing with multiple rolling element EHL contacts and with the applied load to the rolling elements varying along the circumference of the bearing. The results showed that a bearing cannot sustain an adequate layer of base oil on the running track unless significant replenishment takes place. Figure 4 shows the layer variations across the track at different times for a spherical roller bearing 22317. This model presents a new alternative way to study and optimize lubricant migration, EHL film thickness prediction, and lubrication related bearing life [30].

3.4. Starvation degree model

Taking into account the lubricant replenishment induced by surface tension effects, Cann et al. [31] proposed a starvation degree model, which can be expressed as

$$SD = \frac{\eta_0 u a}{h_{\text{oil}\infty}\sigma_s} \qquad \text{(Eq. 11)}$$

where σ_s denotes surface tension and $h_{\text{oil}\infty}$ is the oil height in the vicinity of track. SD is the starvation degree. The influence of each parameter on film thickness was studied individually by keeping other parameters constant. From the value of SD, both the onset and degree of starvation can be determined. Thus the film thickness could be quantified under different operating conditions [31].

4. Lubricant replenishment

To maintain an acceptable inlet lubricant condition, lubricant replenishment from two sides of the track is expected. The replenishment process was first modeled by Chiu [18] who gave equation (1) to predicate the replenishment amount. The replenishment behavior was later experimentally observed by Pemberton and Cameron [17]. Figure 5 shows an oil reservoir around the EHL contact, which presents a typical "butterfly" shape. At the rear of the contact, the lubricant splits into two distinct side bands which will spread due to the squeezing motion of the surfaces and surface tension forces. The inlet boundary condition is determined by the balance between the rate at which oil is entrained and the rate at which it is lost around the contact edges [17].

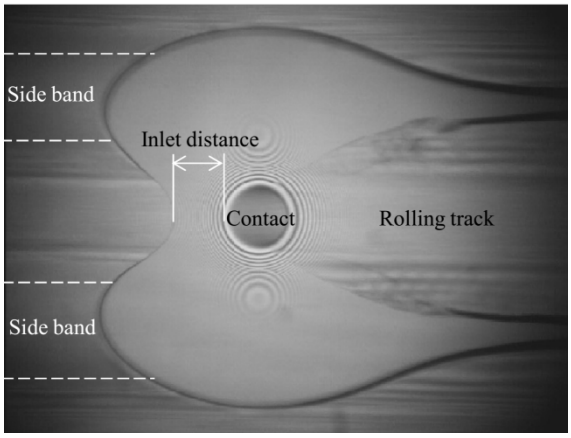

Figure 5: Oil reservoir, contact and track (own work)

Chiu's model was extended to oil-mist lubricated full bearings by Olaru and Gafitanu [32, 33] who modified the replenishment model according to the bearing geometry parameters. By considering the lubricant replenishment, the starvation criterion [20], film thickness reduction factor, and thermal factor [34], a good agreement between test results and theoretical predictions was obtained.

However, one limitation of Chiu's model is that the side bands are assumed thick so that it is only suitable for moderate starvation. In order to simulate extremely

starved EHL contacts e.g., the parched EHL [35], Guangteng and Spikes [27] proposed a disjoining pressure induced replenishment mechanism. The evolutions of film thickness with entrainment speed under fixed oil amount of 1.5 g are shown in Figure 6. For the curve of w = 70 N, the stage of rapid drop in film thickness can be simulated by Chiu's model, and the stage at which the curve tends to level off can be predicted by the disjoining-pressure-driven flow model.

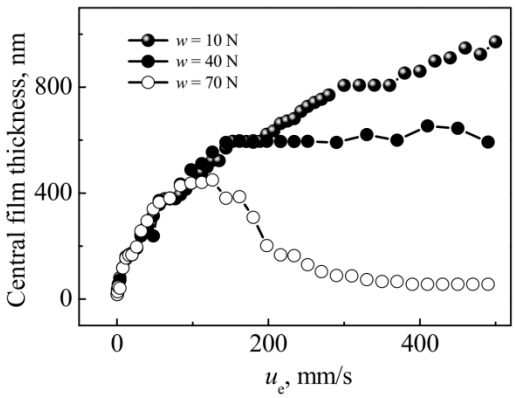

Figure 6: Evolutions of central film thickness with entrainment speed u_e under different loads, PAO 40, oil amount 1.5 g (own work)

Later, Jacod et al [37] divided the replenishment mechanisms into an 'out-of-contact' mechanism and an 'in-contact' mechanism. As shown in Figure 2, the 'out-of-contact' reflow is generated due to the surface tension gradient and disjoining-pressure. The 'in-contact' reflow is induced by local capillary forces. The effect of 'in-contact' reflow was verified experimentally by observing the oil reservoir grow-up under stationary contacts [37].

However, Gershuni et al. [31] found for fully lubricated bearings that the lubricant replenishment induced by surface tension was negligible, whilst the centrifugal forces played a dominant role. Due to a similar reason, the effect of centrifugal forces is primarily considered in Van Zoelen's simulations [26]. Liang et al. [39] investigated the influence of centrifugal forces on oil reservoir distributions using a model test device.

From the model tests, it was found that the critical speeds beyond which progressive starvation will take place [31], is far lower than those encountered in practice [40]. However, bearings can usually safely work long periods, indicating that other mechanisms impact lubricant replenishment. For instance, the spin effect may transport lubricant back into the rolling track [41]. Damiens et al. [42] found that the cage clearance could significantly affect the starvation response due to lubricant redistributions. Cann and Lubrecht [43] confirmed that due to the reduction in contact width under unloading, the contact replenishment was improved. In another work, Cann and Lubrecht [44] observed the film recovery when the bearing is at a standstill.

Some approaches are utilized to artificially force replenishment. Ali et al. [45] developed a lubricant channeling unit to guide lubricant flowing back to the track. By imposing lateral vibrations on the main rolling direction, lubricant can be drawn back into the central track [46]. In light of the theory of free boundary layer [24, 25], an oil layer was pre-formed by preceding contact and then was delivered into the contact to be tested [47], thus the starvation degree can be controlled.

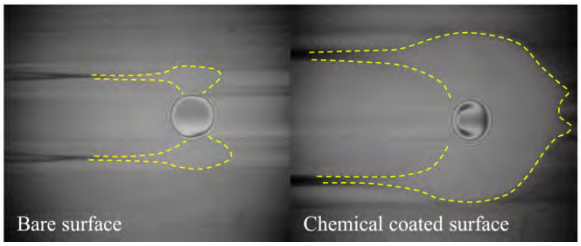

Figure 7: Enhancement of oil replenishment by wettablility gradient (own work)

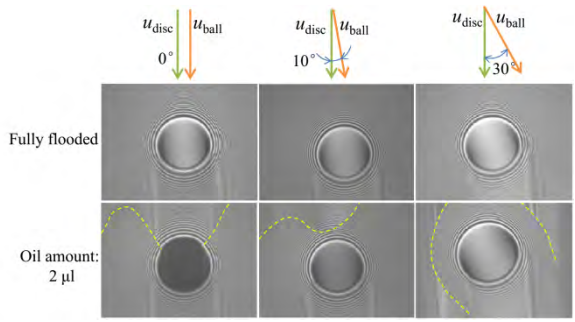

Figure 8: Enhancement of oil replenishment by skewed surface flow (own work)

In the absence of an external aid, lubricant spontaneous replenishment is expected to maintain an acceptable EHL film. By creating a wettability step with chemical coating at the two sides of a rolling track, a robust lubricant replenishment was induced [48]. As shown in Figure 7, the oil reservoir is enhanced remarkably by a wettability gradient. Apart from this, it is found that if a gyroscopic effect is introduced, a side slip effect increases the inlet distance [49] of the meniscus. Figure 8 shows that the inlet oil supply is improved when the surface velocities are skewed with respect to the rolling direction.

5. Starved grease lubrication

The majority of rolling element bearings is grease lubricated. However, the mechanisms of grease lubrication are much more complex than those of oil lubrication. The main reason is that, as a two-phase material, the rheological properties of grease highly depend on the shear situations. The base oil bleeding rate and replenishment behaviors are closely related to the grease shear degradation. Other factors such as temperature, centrifugal force and pressure also affect the base oil bleeding rate. But there is a common belief that starvation prevails in grease lubrication. To acquire the information about grease lubrication both model tests and full bearing tests are conducted. The purpose of model tests is to explore the basic lubrication mechanisms, whilst full bearing tests are necessary for the comprehensive evaluations of grease performance.

5.1. Model tests

Ball-and-disc configuration is usually employed to model the contacts between rolling elements and rings. By this model test approach, the behaviors of grease lubrication can be detected. Great efforts were invested by Cann to reveal the grease lubrication mechanisms. By observing the evolution of film thickness as a function of disc revolutions or time, Cann [50, 51] found that film thickness was initially higher than that with a corresponding base oil lubrication, but then dropped rapidly. Eventually, an equilibrium film lower than that with base oil, was reached. Similar observations are shown in Figure 10. The initial higher film thickness indicates that thickener particles are entrained into the contact [52]. The drop of thickness is caused by progressive starvation due to the displacement of lubricant from the track. The displaced lubricant does not readily reflow unless the yield stress is exceeded.

During the evolution process shown in Figure 9, grease thickener particles are deposited on the rolling track. With the test proceeding, more base oil is released due to a breakdown of the thickener structures, but the released oil is also prone to be expelled from the contact. Finally, a stabilized film is reached due to a flow balance. In some cases, film recovery at a final stage is also found. This is mainly due to an increase in fluidity of the base oil or worked grease caused by repeated shear or elevated temperatures [53]. The evolution of lubricating films determined by a flow balance is schematically given by Cann [53], see Figure 10. The film thickness recovery at stage III is attributed to the improved local supply of lubricant to the contact area at higher temperatures. Similar measurements were conducted by Hurley et al. [54] and Huang et al. [55]. In the whole process, the flow balance is influenced by the oil bleeding rate and the yield stress of the bulk grease. The relationship between shear degradation of grease and the amount of oil release is modeled by Mérieux [56].

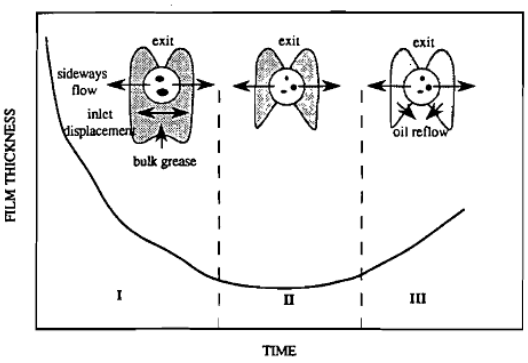

Figure 10: Flow balance in grease lubrication [53]

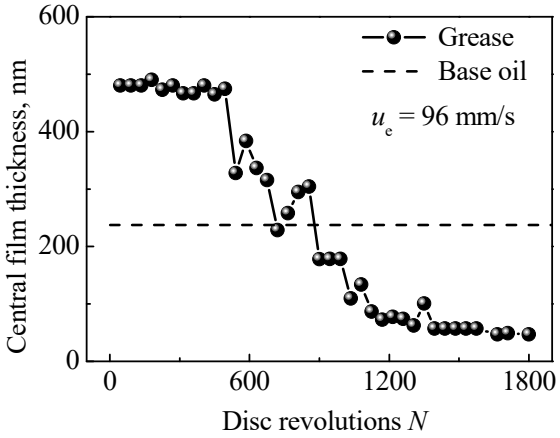

(a) Variations of film thickness with disc revolutions

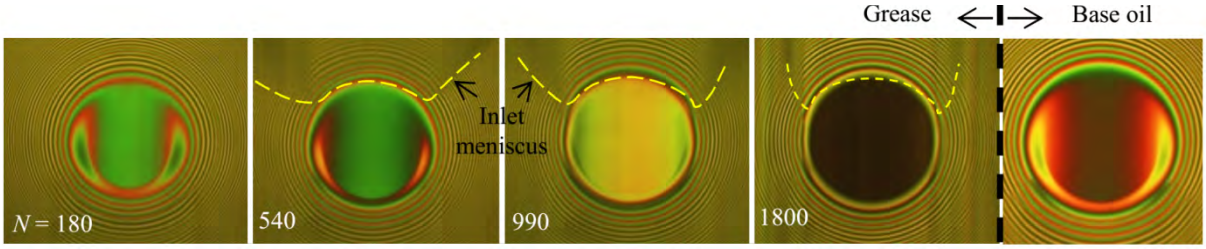

(b) Images of grease and base oil films

Figure 9: Evolutions of grease lubricated contacts with disc revolutions (own work)

From her observations, Cann concluded that the separating films were constituted by two components: a residual film and a hydrodynamic component, which can be expressed as

$$h = h_{residual} + h_{EHL} \qquad (Eq.\ 12)$$

The residual layer is a static layer on the track which has been confirmed by Cann et al. [57] using IR spectroscopy and optical interferometry. Both shear degradation and elevated operating temperature could facilitate the intermittent flow of worked grease and continued flow of base oil, which improves the lubricant availability and hence contributes to the hydrodynamic film component [58].

The mechanism of film formation is schematically described in Figure 11. Åström found that a primary reservoir at the sides of contact governed the lubricant replenishment [59]. The surface tension forces were strong enough to extract base oil or grease with lower soap content from the bulk grease. The size of the primary reservoir also depends on the grease charging amount [60]. As shown in Fig. 12, for the smaller amount of grease, the primary reservoir is also smaller and the inlet distance diminishes. It is found that the film thickness levels off and is speed independent, suggesting an equilibrium state. The curve for 50 mg is elevated compared to that of 3 mg, indicating a higher level of flow balance. With 200 mg, the starvation effect is to a certain extent counteracted by the effect of centrifugal force on the grease reservoir located closer to center than the track in a ball on disc set-up. Under such starvation conditions, Cann [58] emphasized the effects of capillary force on the local replenishment and the resulting flow balance. It is apparent that a large reservoir forms under 200 mg. But depending on the shear situations at different speeds, the film thickness varies with speed.

The main drawbacks of model test comparing with full bearing situations are the rather short time scale, lower contact pressure, absence of spin effect, different feed-loss balance mechanisms, different rolling-sliding states, different effects of centrifugal force and different lubricant flow states [61, 62]. But the model tests are beneficial to explore the basic mechanisms of grease lubrication.

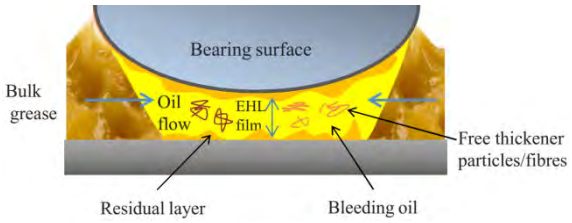

Figure 11: Composition of grease film in a bearing contact (not to scale)

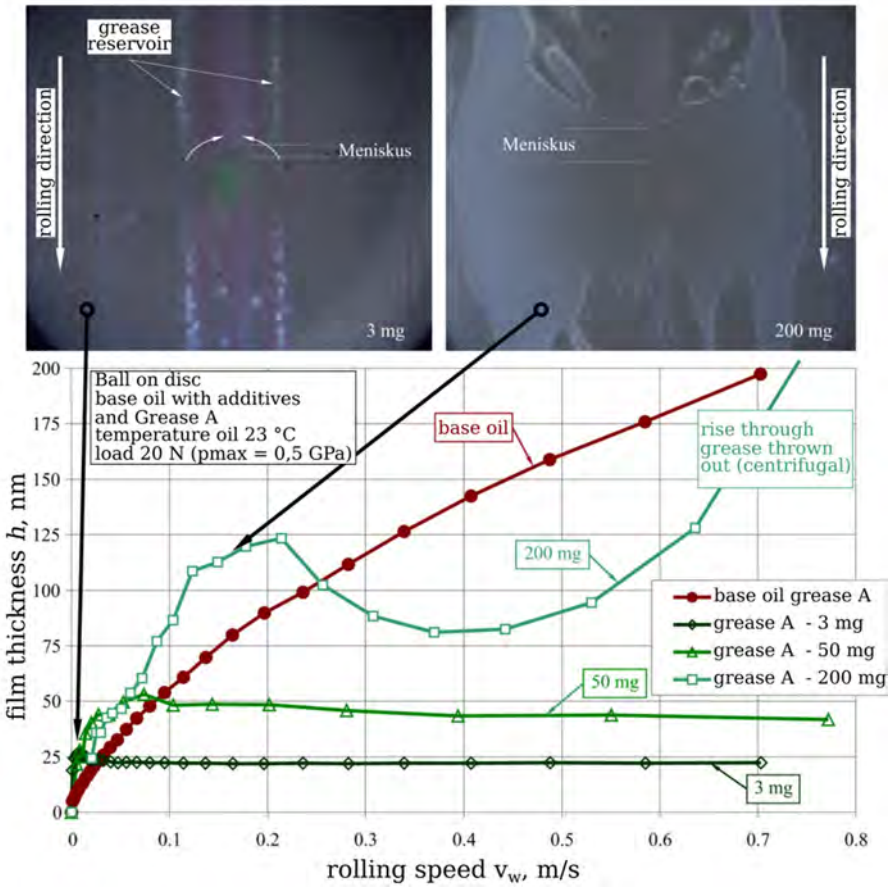

Figure 12: Influence of the amount of grease on the EHL films on the ball-on-disk apparatus [60]

5.2. Full bearing tests

Little work is conducted to assess the full bearing performance under starvation conditions. Using a full bearing test bench, Baly et al. [14, 63] simultaneously measured the film thickness via a capacitance method and the friction torque in angular contact ball bearings (7008C). The results of frictional torque and film thickness are shown in Figure 13. The regime where film thickness drops with speed suggests that the bearing operates under moderate starvation state. Correspondingly, in the same speed range, the friction torque also experiences a regime with lower values. The final increase in friction torque with speed infers a severely starved lubrication state is reached. Due to starvation, unlike for full lubrication, there is no strictly positive correlation between base oil viscosity on one hand and film thickness resp. bearing friction torque on the other

hand. The minimum values of film thickness, and, correspondingly, of friction torqueses are encountered for the base oil with the highest viscosity.

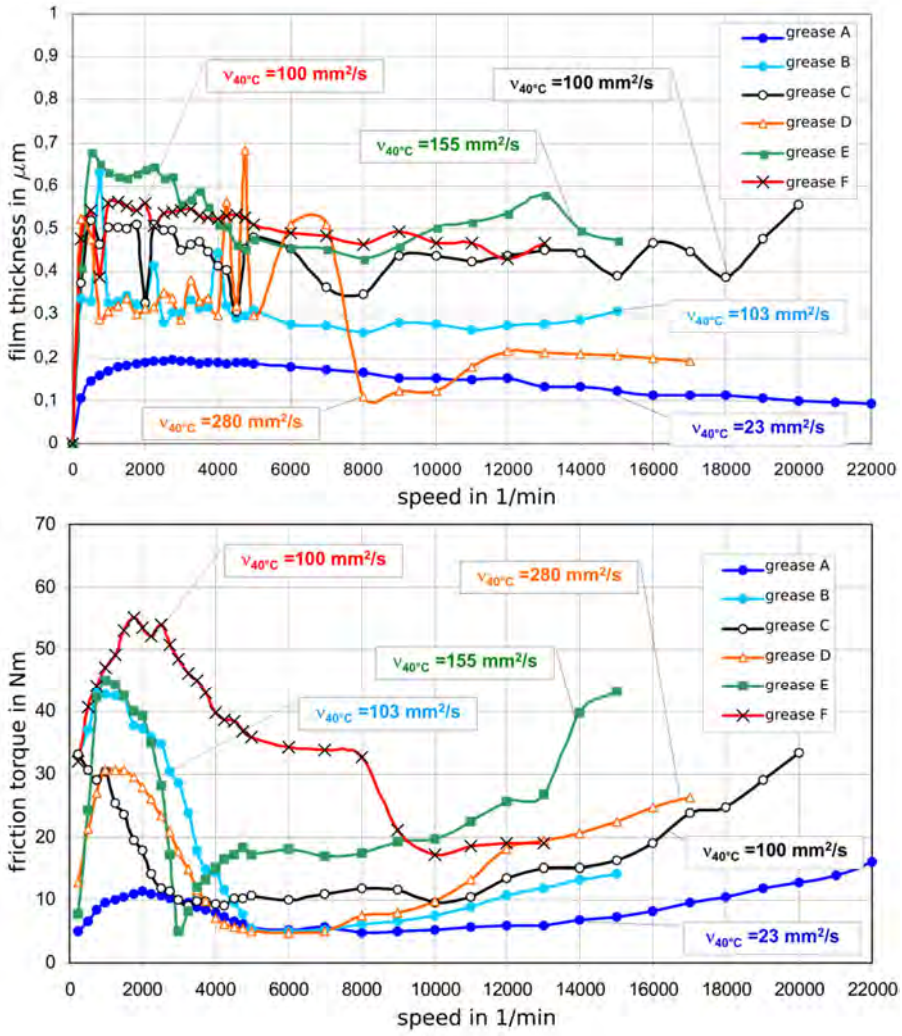

(A) Film thickness *(B) Friction torque*

Figure 13: Test results using greases with different base oil viscosities [14]

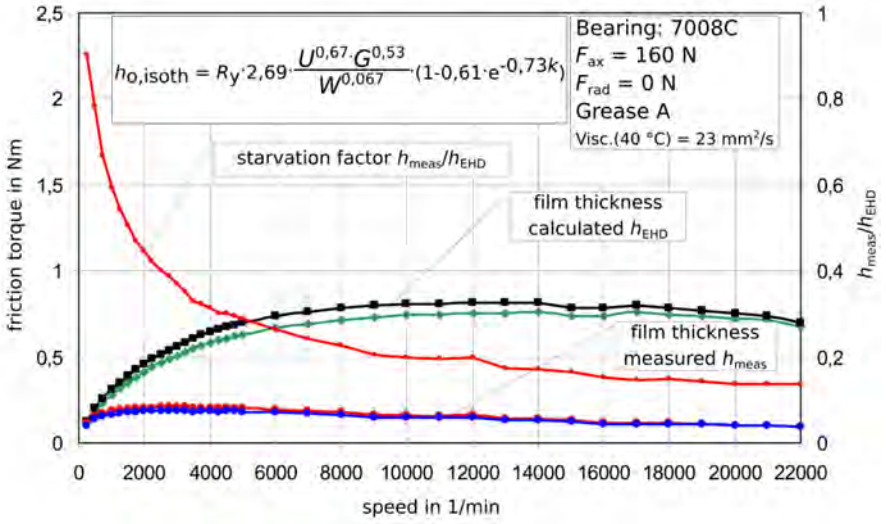

Figure 14: Variations of film thickness and starvation-factor with speed [14]

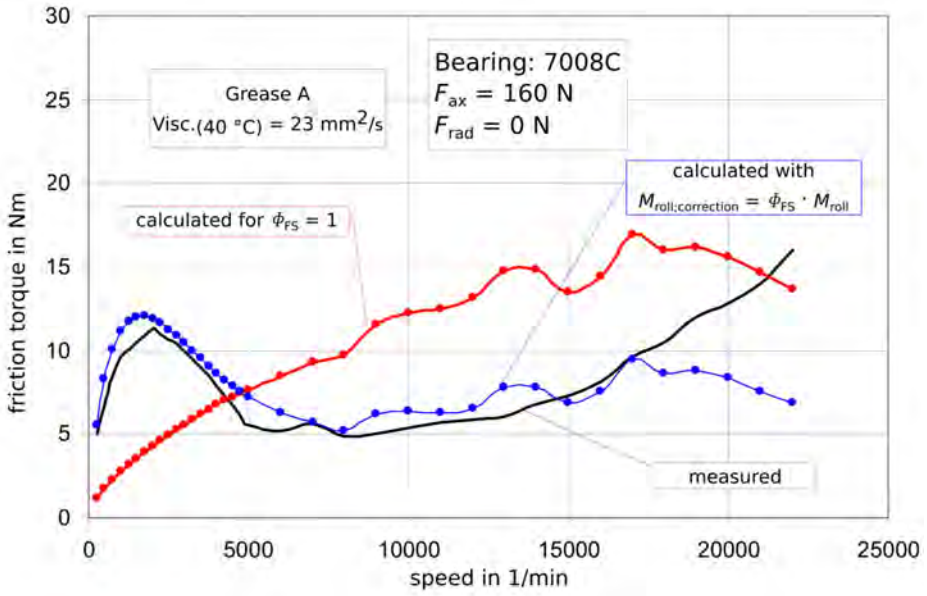

Figure 15: Comparison of moment between measurement and calculation with correction factor [14]

Figure 14 shows that, starting from moderate speeds, the measured film thicknesses were considerably lower than those predicted by the traditional EHL theory. In this example, the measured film thickness continuously decreased in a large speed scope from 3000 min^{-1} to 22,000 min^{-1}. In order to characterize this discrepancy, a 'Starvation-Factor' was introduced by defining the ratio between the actual and theoretical film thickness h_{mess}/h_{EHD}. It can be seen that this factor is an exponential function of speed, which decreases from 2.5 to 0.2. It should be noted, though, that such a relationship is strongly history-dependendent and only valid after reaching a certain maximum speed and waiting for steady-state conditions at each speed where a measurement is taken. Returning from periods with high speeds, film thicknesses will at first be lower and then will then recover to a certain extent when subsequently operating steadily at a lower speed. The higher the maximum speed, the more pronounced this effect will be. In contrast, when steadily increasing speed with a freshly greased bearing, film thicknesses will at first be higher for each speed and then slowly decay when the bearing continues to run steadily at this speed. Thus, the results presented in Figs. 12, 13, 14 and 15 are only valid for truly steady state conditions and after reaching the individual maximum speed of each test. It can be concluded that the real degree of starvation depends on a sensitive equilibrium which requires time to re-adjust after each change of conditions.

Furthermore, to characterize the starvation effects on the friction torque, a rolling resistance correction factor Φ_{FS} was employed [64], which was originally used for the calculation of oil-lubricated bearings. The modified factor Φ_{FS} links the real hydrodynamic friction torque to the uncorrected hydrodynamic friction torque:

$$M_{Roll\ red\ hyd} = \Phi_{FS} \cdot M_{Roll\ voll\ hyd} \qquad (Eq.\ 13)$$

where $M_{Rollredhyd}$ and $M_{Rollvollhyd}$ denote the real hydrodynamic friction torque and the uncorrected hydrodynamic friction torque. The factor Φ_{FS} can be calculated from

$$\Phi_{FS} = \frac{A}{e^{B\frac{\upsilon}{\upsilon_{40} n C_L}}} \qquad (Eq.\ 14)$$

In equation (14), the coefficients A and B need to be individually determined for each grease. C_L is a bearing type specific factor, n the rotational speed and ν the viscosity of the base oil at operating temperature. It is interesting to note that a roughly linear relationship exists between h_{mess}/h_{EHD} and Φ_{FS}. Obviously, the change of inlet conditions brought about by starvation simultaneously reduces film thickness and, in the same way, shear losses in the fluid before entering the parallel gap in the contact.

Figure 15 compares the measured results with the calculated results corrected by Φ_{FS}. It can be seen that the calculated curve matches well with the measured curve up to 17,000 min^{-1}; beyond that speed the correction function is no longer valid. Overall, it can be noted that at low speeds the correction values are greater than 1 and at high speeds, significantly smaller than 1.The "undulations" in the calculated curves are due to the fact, that the measured bearing outer ring temperatures were used to determine the base oil viscosities for each speed which in turn formed one input for the calculations.

Baly's work also showed that the number of balls – and therefore the time between ball passages - affects the film thickness in some speed ranges. Moreover, the full bearing test results were compared with those of model tests. Similar patterns of film thickness with speed were found [63].

Cen and Lugt [65] also investigated the film thickness behavior in full bearings, finding that all bearings run in starvation. Similar to the findings in model tests they also observed that during start up the films are usually higher than the films expected for base oil lubrication,

but decrease after a typical running time. Then the film usually stays unchanged and even speed independent, i.e., the starvation increases with higher speeds. Furthermore, Cen and Lugt [65] observed that the greases with lower shear stability gave higher film thicknesses than greases with higher stability films. This of course does not mean that these greases are better suited as the study did not investigate grease life [65].

Starvation seems more prone to occur at low temperatures due to high apparent viscosity and low bleeding rate. At low temperatures, the grease will be subject to high shear stresses even at low shear rates, which will subsequently result in high start-up and running torques. Wikström [10] measured the starting and steady-state friction torque of grease lubricated rolling bearings at low temperatures. The main conclusion is that the base oil properties are important for starting and running torques both at low and high temperatures. Gerstenberger [11, 65] measured the friction torque at continuously low temperatures over a long period of time. It can be seen in Figure 16 after 150 hours; the friction torque and the temperature at the inner-ring flange begin to fluctuate considerably, indicating the occurrence of starvation. Furthermore, the lubrication state at the large roller ends was observed using UV-induced fluorescence technique. Figure 17 gives a series of roller ends pictures. In this way, the profiles of grease can be plotted which provides direct evidence of starvation.

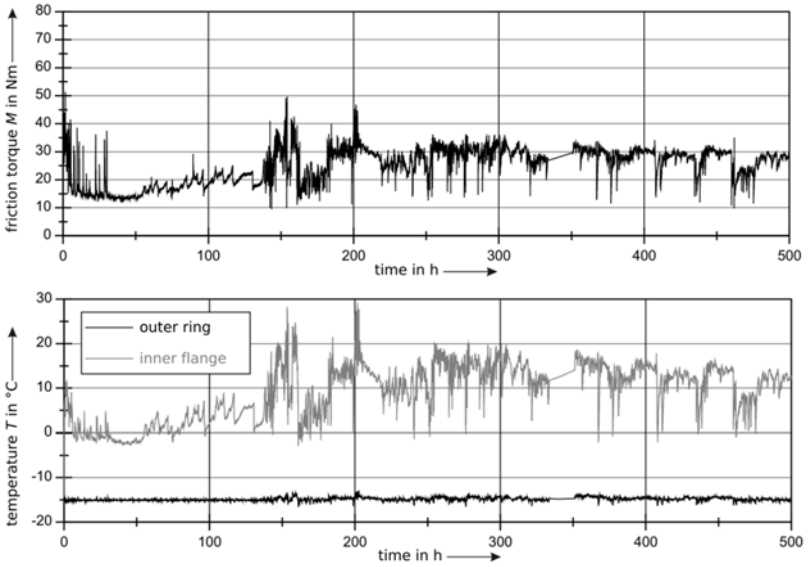

Figure 16: Friction torque compared to the temperatures at the inner-ring flange (grey) and at the outer ring exterior surface (black) (barium-complex soaped grease, Fax = 50 kN, n = 75 min-1, T = -15°C) [11, 65]

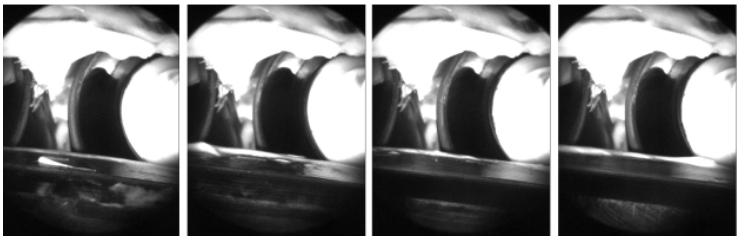

Figure 17: Pictures of a roller, each picture is separated by a period of 6 revolutions of the inner ring [11, 65]

Similar to lubrication states controlled by feed-loss balance in model tests, this balance also exits in grease lubricated full bearings. Booser [67] and Baker [68] were the first to propose the feed-loss balance to clarify the mechanisms of grease lubrication. Based on the results at low temperatures, Wikström [62] suggested a new feed-loss balance as shown in Figure 18. Obviously, the mechanism of feed-loss balance in full bearings is more complex than that of model tests.

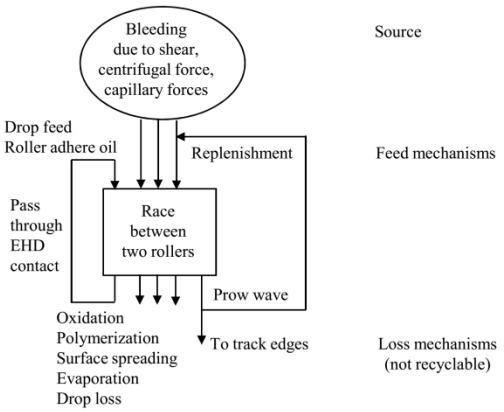

Figure 18: Suggested feed-loss balance [62]

6. Starved contacts with restricted oil supplying

Nowadays, high speed spindles are employed by machine tools to improve the surface quality of mechanical parts. Consequently, there is a requirement of higher limiting speed of rolling element bearings. Some conventional lubrication methods such as oil bath, circulating oil and grease lubrication face challenges in such environments. Alternatively, the oil-air lubrication technique which directly delivers fine droplets to the rolling track by pressurized air has received attention [13]. However, the mechanisms of oil-air lubrication are not fully explored yet. In oil-air lubrication, only a minute amount of oil is injected into the bearings. It is actually a type of restricted oil supplying technique, which leads to a constantly starved operation in the region of optimal friction torque. The parameters of air pressure, tube length, oil feeding interval as well as the nozzle structures will affect the distributions of droplet and hence lubrication state. Fundamental studies under oil-air supplying were conducted by Liang et al. [69] who investigated the influence of the oil supply rate on the degree of starvation.

More fundamental work has been carried out numerically and experimentally to investigate the film formations under droplet feeding [70-72]. Figure 19 shows the numerical results of the passage of a single droplet. It shows that the droplet is so small that it cannot fully spread and causes local surface deformation. Most recently, van der Kruk et al. [73] employed droplet-on-demand printing as a novel method to precisely control lubricant supply at a minimum level. In Figure 20, the film thickness evolution over time is presented. With droplet feeding, the transition of lubrication state from severe starvation to nearly fully flooded state can be observed. The results provide a very strong incentive for further investigation of droplet-on-demand printing as a method to achieve optimum (re)lubrication at minimum level in the realistic setting of a rolling bearing [73].

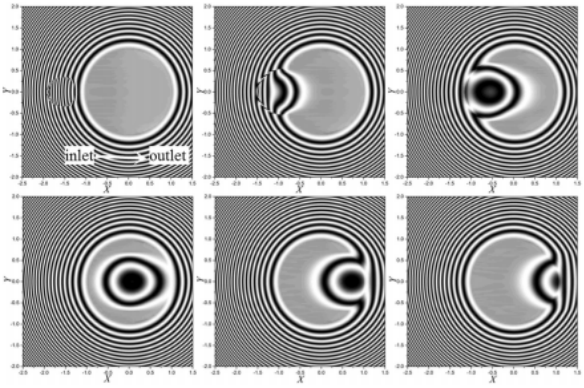

Figure 19: Numerical EHL pseudo-interference patterns when an oil droplet passing through an EHL contact, lubricant: 5P4E, w =30 N, ue =10 mm/s, radius of the steel ball =12.7 mm [70]

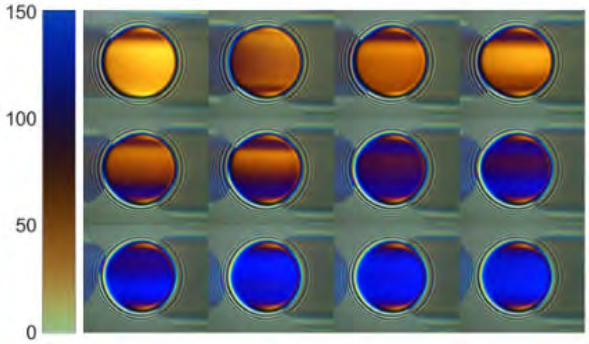

Figure 20: Image sequence of a contact that is lubricated with a droplet supply frequency of 5 Hz. The entrainment direction is from left to right. Time develops in lexicographic order from left to right [73]

7. Summary

This paper reviewed some typical issues related to starvation in rolling contacts. The starvation mechanism, starvation criteria, lubricant replenishment, starved grease lubrication and starved contacts with restricted lubricant supply were introduced. The starvation degree is determined by a feed-loss balance which is encountered both in model tests and in full bearing tests. Lubricant replenishment mechanisms induced by surface tension gradients, disjoining pressure and capillary force are distinguished by model tests. More complex sources of lubricant replenishment such as rolling element spin, vibration, cage effect etc exist in full bearings. These replenishment mechanisms contribute to an available feed-loss balance level and thus starvation state. Full bearing tests have demonstrated that the occurrence of starvation is beneficial to reduce friction torque. This idea is shown in Figure 21 where an optimum range exists [69]. Within this range, the frictional coefficient is as low as possible without causing mixed friction and wear. That means the supplied amount of lubricant and hence starvation degree should be precisely controlled. For grease lubrication, the oil bleeding behavior depending on the grease degradation, the grease flow and distributions in rolling bearing should be further explored. For oil-air lubrication method, more fundamental knowledge about the influence of the solid surface on droplet distributions, the design of oil supplying structures and mechanisms of dynamic film formation are to be acquired.

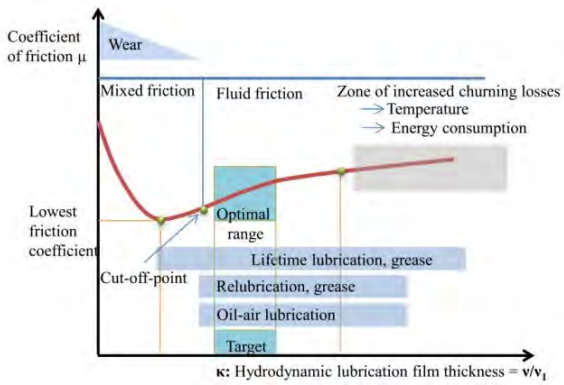

Figure 21: Variation of friction coefficient with κ [13]

Acknowledgment

The authors would like to express their thanks to the financial support from the Natural Science Foundation of China (Project No. 51875299).

References

[1] A. M. Ertel. Hydrodynamic Lubrication Based on New Principles. Akad. Nauk. SSSR, Prikladnaya Matematika i Mekhanika, 3(2) (1939) 41-52. (in Russian).

[2] A. N. Grubin. Fundamentals of the Hydrodynamic Theory of Lubrication of Heavily Loaded Cylindrical Surfaces, Book No. 30, Central Scientific Research Institute for Technology and Mechanical Engineering, Moscow (DSIR Translation) (1949) 115-166.

[3] B. J. Hamrock, D. Dowson. Isothermal elastohydrodynamic lubrication of point contacts, part 1-theoretical formulation. ASME J Lubr Technol, 98 (1976) 223-229.

[4] B. J. Hamrock, D. Dowson. Isothermal elastohydrodynamic lubrication of point contacts, part 2-elipticity parameter results. ASME J Lubr Technol, 98 (1976) 375-383.

[5] B. J. Hamrock, D. Dowson. Isothermal elastohydrodynamic lubrication of point contacts, part 3-Fully Flooded Results, ASME J Lubr Technol, 99 (1977) 264–276.

[6] Using a friction model as an engineering tool. SKF-Evolution, 8 July, 2006.

[7] P. M. Lugt. A Review on grease lubrication in rolling bearings. Tribol Trans, 52 (2009) 470-480.

[8] D. N. Olaru, M. D. Gafitanu. Starvation in ball bearings. Wear, 170 (1993) 219-234.

[9] F. Itoigawa, T. Nakamura, T. Matsubara. Starvation in ball bearing lubricated by oil and air lubrication system. Tribology International, 34 (1999) 243-252.

[10] V. Wikström. Rolling bearing lubrication at low temperature. PhD Thesis, Luleå University of Technology, Luleå Sweden, 1996.

[11] Gerstenberger J. Rolling bearing lubrication with grease at low temperatures. PhD Thesis, Leibniz Universität Hannover, Hannover Germany, 2005. (In German)

[12] J. Kuhlmann. Tribology of bearing lubrication greases under steady low temperature conditions. PhD Thesis, Leibniz Universität Hannover, Hannover Germany, 2009. (In German)

[13] Schmidt H, Schwartz J. Energy-efficient minimal quantity lubrication for high-speed spindles. SKF-Evolution, 11 September, 2014.

[14] H. Baly. Reibung fettgeschmierter Wälzlager. Dissertation, Leibniz Universität Hannover, 2005.

[15] M. Pasdari, C. R. Gentle. Effect of lubricant starvation on the minimum load condition in a thrust-loaded ball bearing. ASLE Transactions, 30(3) (1987) 355-359.

[16] L.D. Wedeven, D. Evans, A. Cameron. Optical analysis of ball bearing starvation. ASME J Lub Tech, 93(3) (1971) 349-361.

[17] Pemberton J, Cameron A. A mechanism of fluid replenishment in elastohydrodynamic contacts. WEAR 1976; 37(1): 185-190.

[18] Y. P. Chiu. An analysis and prediction of lubricant film formation in rolling contact systems. ASLE Tribol Trans, 17 (1974) 22-35.

[19] B. Jacod, F. Pubilier, P. M. E. Cann, A. A. Lubrecht. An analysis of track replenishment mechanisms in the starved regime. Proceedings of the 25th Leeds–Lyon Symposium on Tribology (1998) 483-92.

[20] B. J. Hamrock, D. Dowson. Isothermal elastohydrodynamic lub rication of point contacts: part IV-starvation results. ASME J Lub Tech, 99(1) (1977) 15-23.

[21] F. Chevalier, A.A. Lubrecht, P.M. Cann, F. Colina, G. Dalmaz. Starvation phenomena in E.H.L. point contacts: influence of inlet flow distribution. The Third Body Concept Interpretation of Tribological Phenomena, (1996) 213-223.

[22] H. G. Elrod, M. L. Adams. A computer program for cavitation and starvation problems. Proceedings of the 1st Leeds-Lyon Symposium on Tribology, (1974) 37-41.

[23] H. G. Elrod. A cavitation algorithm. ASME J Lub Tech, 103(3) (1981) 350-354.

[24] F. Chevalier, A.A. Lubrecht, P.M. Cann, F. Colina, G. Dalmaz. Film thickness in starved EHL point contacts. ASME J Tribol, 120 (1) (1998) 126-133.

[25] B. Damiens, C. H. Venner, P. M. Cann, A. A. Lubrecht. Starved lubrication of elliptical EHD contacts. ASME J Tribol, 126 (1) (2004) 105-111.

[26] M. T. van Zoelen, C. H. Venner, P. M. Lugt. Free surface thin layer flow on bearing raceways. ASME J Tribol, 130 (2008)1-10.

[27] M. T. van Zoelen, C. H. Venner, P. M. Lugt. Prediction of film thickness decay in starved EHL contacts using a thin layer flow model. Proc Imech E, Part J J Eng Tribol, 223(2009) 541-552.

[28] E. Kingsbury. Cross-flow in a starved EHD contacts. ASLE Tribol Trans, 37(10) (1973) 276-280.

[29] M. T. van Zoelen, C. H. Venner, P. M. Lugt. The prediction of contact pressure-induced film thickness decay in starved lubricated rolling bearings. STLE Tribol Trans, 53(6) (2010) 831-841.

[30] C. H. Venner, M. T. van Zoelen, P. M. Lugt. Thin layer flow and film decay modeling for grease lubricated rolling bearings. Tribol Int, 47 (2012) 175-187.

[31] P. M. Cann, B. Damiens, A. A. Lubrecht. The transition between fully flooded and starved regimes in EHL. Tribol Int, 37 (2004) 859-864.

[32] D. N. Olaru, M. D. Gafitanu. Starvation in ball bearings. Wear, 170 (1993) 219-234.

[33] D. N. Olaru, M. D. Gafitanu. A new methodology to estimate starvation in ball bearings. Tribotest, 4(1) (1997) 93-106.

[34] L. E. Murch, W. R. Wilson. Thermal elastohydrodynamic inlet zone analysis. Trans ASME I. Luh Tech, 97 (1975) 211-216.

[35] E. Kingsbury, B. Schritz, J. Prahl. Parched elastohydrodynamic lubrication film thickness measurement in an instrument bearing. Tribol Trans, 33 (1993) 11-14.

[36] G. Guangteng, H. A. Spikes. The role of surface tension and disjoining pressure in starved and parched lubrication. Proc ImechE Part J J Eng Tribol, 210 (1996) 113-134.

[37] B. Jacod, F. Pubilier, P. M. E. Cann, A. A. Lubrecht. An analysis of track replenishment mechanisms in the starved regime. Proceedings of the 25th Leeds–Lyon Symposium on Tribology, (1998) 483-92.

[38] L. Gershuni, M. G. Larson, P. M. Lugt. Lubricant replenishment in rolling bearing contacts. STLE Tribol Trans, 51(5) (2008) 643-651.

[39] H. Liang, D. Guo, L. R. Ma, J. B. Luo. Experimental investigation of centrifugal effects on lubricant replenishment in the starved regime at high speeds. Tribo Lett 59(3) (2015).

[40] P. M. Cann. Starvation and reflow in a grease lubricated elastohydrodynamic contact. Trib Trans, 39 (1996) 698-704.

[41] H. Åström, J. Östensen, E. Höglund. Lubricating grease replenishment in an elastohydrodynamic point contact. ASME J Tribol, 115(3) (1993) 501-506.

[42] Damiens B, Cann PM, Lubrecht AA. Influence of cage clearance on bearing lubrication. Trib Trans, 47 (2004) 2-6.

[43] P. M. Cann, B. Damiens, A. A. Lubrecht. The effect of transient loading on contact replenishment with lubricating greases. Proceedings of the Leeds-Lyon Symposium, Lyon, 2-5 September 2003, Publisher: Elsevier, Pages: 745-750.

[44] P. M. Cann, A. A. Lubrecht. Analysis of grease lubrication in rolling element bearings, Lubrication Science, 11(3) (1999) 227-245.

[45] F. Ali, I. Křupka, M. Hartl. Enhancing the parameters of starved EHL point conjunctions by artificially induced replenishment. Tribol Int, 66 (2013) 134-142.

[46] Y. Nagata, K. Kalogiannis, R. Glovnea. Track replenishment by lateral vibrations in grease-lubricated EHD contacts. Tribol Trans, 55(1) (2012) 91-98.

[47] P. Svoboda, D. Kostal, I. Krupka, M. Hartl. Experimental study of starved EHL contacts based on thickness of oil layer in the contact inlet. Tribol Int, 67 (2013) 140-145.

[48] X. M. Li, F. Guo, P. L. Wong, Y. Zhao . Regulation of lubricant supply by wettability gradient in rolling EHL contacts. Tribol Int, 120 (2018) 565-574.

[49] P Larsson. Lubricant replenishment in the vicinity of an EHD contact. PhD thesis, Luleå University of Technolgoy, Luleå Sweden, 1996.

[50] P. M. Cann, H. A. Spikes. Visualisation of starved grease and fluid lubricant films. Lubricants and Lubrication-Proceedings of the 21th leeds-Lyon Symposium on Tribology, (1995) 161-166.

[51] P. M. Cann, F. Chevalier, A. A. Lubrecht. Track depletion and replenishment in a grease lubricated point contact: a quantitative analysis. Proceedings of the 23rd Leeds-Lyon Symposium on Tribology, (1996) 405-413.

[52] H. Åström, O. Isaksson, E. Höglund. Video recordings of an EHD point contact lubricated with grease. Tribol Int, 24(3) (1991) 179-184.

[53] P. M. Cann. Starvation and reflow in a grease-lubricated elastohydrodynamic contact. Tribology Transactions, 39(3) (1996) 698-704.

[54] S. Hurley, P. M. Cann, H. A. Spikes. Lubrication and reflow properties of thermally aged greases. Tribol Trans, 43(2) (2000) 221-228.

[55] L. Huang, D. Guo, S. Z. Wen. Film thickness decay and replenishment in point contact lubricated with different greases: A study into oil bleeding and the evolution of lubricant reservoir. Tribol Int, 93 (2014) 620-627.

[56] J. S. Mérieux, S. Hurley, A. A. Lubrecht, P. M. Cann. Shear-degradation of grease and base oil availability in starved EHL lubrication. Thinning Films and Tribological Interfaces Proceedings of the 26th Leeds-Lyon Symposium on Tribology, (2000) 581-588.

[57] P. M. Cann, M. Aderin, H. A. Spikes. Optical and infrared studies of the EHD behaviour of greases. EUROGREASE, (1991).

[58] P. M.Cann. Understanding grease lubrication. The Third Body Concept Interpretation of Tribological Phenomena, 31 (1996) 573-581.

[59] H. Åström, J. O. Östensen, E. Höglund. Lubricating grease replenishment in an elastohydrodynamic point contact. ASME J Tribol, 3 (1993) 501-506.

[60] C. Meyer. Reibung in hoch belasteten EHD-Wälzkontakten. Dissertation, Leibniz Universität Hannover, 2010.

[61] P. Lugt. A review on grease lubrication in rolling bearings. Triblogy Transactions, 52 (2009) 470-480.

[62] V. Wikström, B. Jacobson. Loss of lubricant from oil-lubricated near-starved spherical roller bearings. Proceedings of the Institution of Mechanical Engineers, Part J: Journal of Engineering Tribology, 211(1) (1997): 51-66.

[63] H. Baly, G. Poll, P. M. Cann, A. A. Lubrecht. Correla-tion between model test devices and full bearing tests under grease lubricated conditions. IUTAM symposiu-mon elastohydrodynamics and micro elastohydrodyna-mics, 134 (2006) 229-240.

[64] G. M. Espejel. Using a friction model as an engineering tool. SKF-Evolution, 2 (2006).

[65] H., Lugt, P.M., 2019. Film thickness in a grease lubricated ball bearing. Tribology International 134, 26–35. DOI: 10.1016/j.triboint.2019.01.032

[66] Gerstenberger J. Poll G. Rolling bearing lubrication with grease at low temperatures. Tribology Series, Elsevier, 2001, 39: 303-312.

[67] E. R. Booser, D. F. Wilcock. Minimum oil requirements of ball bearings. Lubric, Engng, (1953) 140-143.

[68] A. E. Baker. Grease bleeding-a factor in ball bearing performance. NLGI Spokesman, (1958) 271-277.

[69] H. Liang, D. Guo, L. R. Ma, J. B. Luo. The film forming behavior at high speeds under oil-air lubrication. Tribology International, 91 (2015) 6-13.

[70] S. Y. Li, F. Guo, X. M. Li, C. L. Liu. Numerical simu-lation of an oil droplet passing through an EHL contact. Tribology International, 112 (2017) 58-67.

[71] X. M. Li, F. Guo, S. P. Wang, C. L. Liu, W. Z. Wang. Behaviors of a micro oil droplet in an EHL contact. Fri-cation, 4(4) (2016) 359-368.

[72] C. L. Liu, F. Guo, X. M. Li, S. Y. Li, S. L. Han, Y. Wan. Experimental study of elastohydrodynamic lubrication behaviour under single oil droplet supply. Tribology International, 118 (2018) 432-440.W. M. van der Kruk, S. A. Smit, T. J. Segers, X. M. Li,

[74] C. H. Venner. Drop-on-demand printing as novel method of oil supply in elastohydrodynamic lubrication. Tribology Letters, 67 (2019) 95. Cen,

Method for the investigation of the EDM breakdown voltage of grease and oil on rolling bearings

Dani Bechev[1], Resat Capan[1], Attila Gonda[1], Bernd Sauer[1]

[1] *University of Kaiserslautern, Institute of Machine Elements, Gears and Transmissions, bechev@mv.uni-kl.de, capan@mv.uni-kl.de, attila.gonda@mv.uni-kl.de, sauer@mv.uni-kl.de*

Abstract – Rolling bearing currents cause damage both to the bearing and to the lubricant contained therein. To prevent such damage, the influence of the lubricant in the bearing is becoming increasingly important. By analysing the discharge currents and the breakdown voltage in rolling bearings with lubricants of different composition, knowledge of the electrical behaviour of the system (bearing and lubrication) can be gained. In the context of this paper, a method for characterizing the breakdown voltage at the rolling bearing and results of investigated greases and oils are presented.

Keywords – EDM, breakdown voltage, bearing currents

1. Introduction

The use of frequency inverters to control variable-speed inverter-fed electric motors and generators causes damage to the rolling bearings as a result of bearing currents [1-6]. This problem has become even more significant in recent years with the increasing use of inverter-controlled electric motors in the automotive industry. As known current-related damages, the crater formation in the bearing raceway, the fluting across the raceway and the oxidation of the lubricant in the contact zone between the rolling element and raceway can be observed [7-10]. They can be seen in Figure 1. Investigations in recent years have shown that the lubricant used in the rolling contact and its electrical properties have a major influence on these damages caused by current passage. Depending on the composition and the electrical and rheological properties of the lubricant, different electrical effects can be observed in the bearing [8-10]. Currently there are no standards or prescribed test methods for the characterization of the electrical lubricant properties: relative permittivity, specific electrical conductivity and breakdown field strength for rolling bearing lubrication under realistic rolling bearing conditions of high pressure, high temperature and shearing [8]. There are standards for the investigation of the electrical lubricant properties only for transformer oils [11-13]. Investigations regarding the electrical lubricant properties were carried out in [14-21], and the breakdown properties of lubricants were examined in [21-24].

2. Aim of the paper

In the context of this paper, investigations of the damaging current passage in rolling bearings subjected to voltage for lubricating greases and oils of different composition are presented. The lubricants differ in their rheological and electrical properties. The focus is on the discharge currents, also called "Electric Discharge Machining" currents (EDM-currents). Interesting in this context is the occurrence of EDM-currents as a function of the conductivity of the lubricant used. In addition, this paper presents a method for the determination of the breakdown voltage of the lubricant in the rolling bearing contact under conditions of practical relevance.

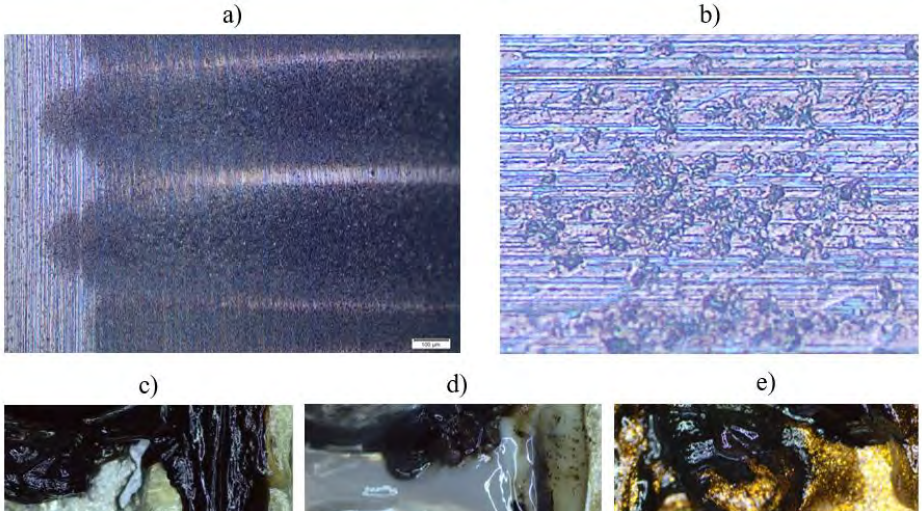

Figure 1: Damages caused by bearing currents and bearing voltage: a) fluting, b) crater formation, c), d), e) grease degradation

3. Basics

3.1. EDM-breakdowns and EDM-currents

Depending on the insulating capacity of the lubricating film in the rolling bearing and the system capacities, bearing voltages occur. Figure 2 shows oscillograph measurements of bearing currents and bearing voltages.

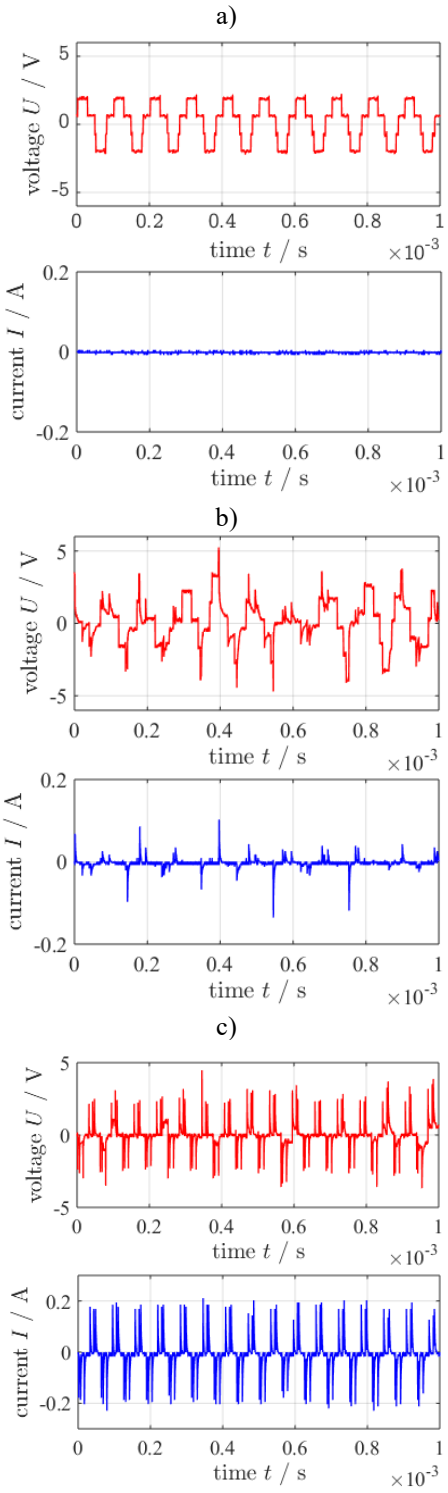

Figure 2: Oscillograph measurements of bearing currents and bearing voltages: a) no EDM-breakdowns, recharging currents, b) EDM-breakdowns, c) no EDM-breakdowns, ohmic-currents

An EDM-current occurs as soon as the voltage across the bearing exceeds the insulating capacity of the lubricating film. The sudden discharge occurs in the form of an arc between the bearing rings and the rolling elements. When conventional rolling bearing greases or oils are used, the insulating behaviour of the lubricating film depends on the lubricating film thickness and the breakdown field strength of the lubricant. The lubricant used in the bearing thus has a crucial influence on the occurrence of EDM-currents. The use of conductive lubricants is expected to prevent voltage build-up across the lubricating gap and thus prevent EDM flows [8], [19], [20]. Figure 2 shows typical electrical events during the application of voltage to a rolling bearing.

Figure 2 a) shows that the voltage can be built up completely over the lubricating film. The insulating properties of the lubricating film are not exceeded, in this way no EDM-breakdowns occur. Only non-critical recharging currents flow. A complete voltage build-up is only possible if the bearing runs in full lubrication condition.

Figure 2 b) shows the voltage and current characteristics when EDM-currents occur. If the insulating property of the lubricating film is exceeded, the voltage drops abruptly and a discharge current flows. The bearing runs in full lubrication condition. A reduction in the height of the lubricating film (e.g. due to a reduction in speed) or an increase in the bearing voltage lead to the fact that the breakdown field strength of the lubricating film is reached earlier, so that the probability of an EDM-breakdown increases.

If the bearing runs in mixed friction condition, metallic contact occurs between the rolling elements and the bearing rings. As a result, no voltage can be built up across the lubrication gap. Figure 2 c) shows this condition. Only voltage pulses and ohmic currents can be observed. With high bearing voltages, the event shown in Figure 2 c) also occurs at full lubrication in the bearing. By using conductive lubricants, it is also expected that no voltage will build up across the lubrication gap [7], [8], [19], [20]. The breakdown voltage of the lubricant can be determined by the generation of EDM-breakdowns in the bearing.

3.2. Investigated lubricants

In order to investigate the effects of insulating and conductive lubricating greases and oils on bearing voltage, lubricating greases with different base oils, thickeners and additives were investigated. G1 (grease 1) and O1 (oil 1) are two insulating lubricants. O1 is the base oil of grease G1. G2 has the same composition as G1. In addition, 10 % copper powder was added to increase the conductivity. O2 is an oil with medium conductivity. O3 and G3 are company products for which the composition is not known. O3 is the additive base oil of G3. It is known that O3 and G3 are conductive, and the conductivity is increased with the help of ionic liquids. The basic lubricant data of the investigated greases and oils can be found in Table 1.

Table 1: Investigated lubricants

Grease	Base oil viscosity at 40°C [mm²/s]	Base oil viscosity at 100°C [mm²/s]	Base oil	Thickener	Additive
G1	105	11	mineral oil	lithium	no
G2	105	11	mineral oil	lithium	10% copper
G3	108	14	product	product	Ionic liquid
Oil	**Base oil viscosity at 40°C [mm²/s]**	**Base oil viscosity at 100°C [mm²/s]**	**Base oil**		**Additive**
O1	105	11	mineral oil	-	no
O2	100	20	polyglycol	-	no
O3	108	14	product	-	Ionic liquid

3.3. Used test benches and test procedure

For the investigation of rolling bearing voltage and currents, several test rigs were developed and set up at the Institute of machine elements, gears and transmissions (MEGT) at the Technical University of Kaiserslautern, which allow the realistic reproduction of the electrical conditions in the rolling bearing of inverter-fed electric motors. The special feature of the experiments is that, in comparison to the real electric motor, the electrical and mechanical operating conditions can be varied independently of each other. The converter used was developed especially for these applications, more detailed information is given in [7] and [8].

The investigations for this study were carried out on an axial bearing test bench called "GESA - Device for extended lubricant analysis". The GESA test cell can be seen in Figure 3. The test setup was developed and set up as part of the research project FVA 650 II “Methodology for the practical characterization of electrical lubricant properties to improve the computational prediction of bearing currents” at the Research Association for Drive Technology (FVA). GESA consists of a vertically arranged shaft equipped with a deep groove ball thrust bearing type 51208 (15 rolling elements) and it is driven by an electric motor. The test stand is characterised by quiet and low-vibration running, which ensures stable formation of a lubricating film in the rolling bearing. This is a requirement for characterizing the electrical properties of lubricants [10], [21].

Voltage and current flows at the rolling bearing can be measured under controlled and reproducible conditions (speed, load and temperature). The measurement and the control of the current flow and temperature are realized by a self-developed slip ring. Both the rotating shaft and the housing can be cooled with the help of water cooling. The impedance and the capacity of the lubricated bearing can be determined with this measuring setup, as well.

The test sequence for each of the six tested lubricants is the same and it is shown in Figure 4. In the first phase, the lubricant is pre-conditioned and the bearing runs in under constant load and speed for a period of 16 hours without applying voltage. In phase 2, a test voltage is applied to the bearing. The applied test voltage is varied from 1 V to 60 V under constant load, speed and a fixed switching frequency of the inverter. In the subsequent phases 3 and 4, the bearing temperature is increased from approx. 10 °C to 100 °C at constant load and speed. A constant test voltage is applied to the bearing in these phases (phase 3 with 5 V; phase 4 with 20 V). The bearing current and the bearing voltage are measured in regular temperature steps. The detailed test conditions of the individual phases can be found in Table 2.

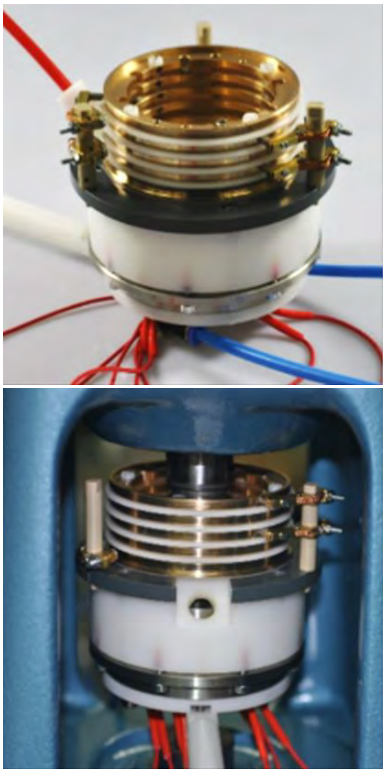

Figure 3: GESA - Device for extended lubricant analysis

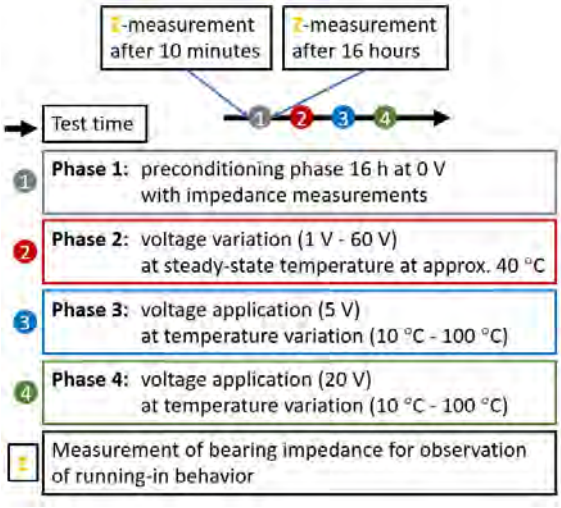

Figure 4: Test procedure including 4 phases

Table 2: Test conditions for the GESA tests in 4 phases

	Speed n / rpm	Load F / N	Test voltage U / V	Switching frequency f / kHz	Temperature ϑ / °C	Duration t / h
1 Phase 1	1000	240	0	0	steady-state ca. 40	16
2 Phase 2	1000	200	1 - 60	10	steady-state ca. 40	0,5
3 Phase 3	1000	200	5	10	10-100	2
4 Phase 4	1000	200	20	10	10-100	2

4. Results of the investigations

At the beginning of the investigations, no information on the electrical properties of the lubricants was available. For this reason, the lubricants were measured on a cylinder capacitor. The results are shown in Figure 5.

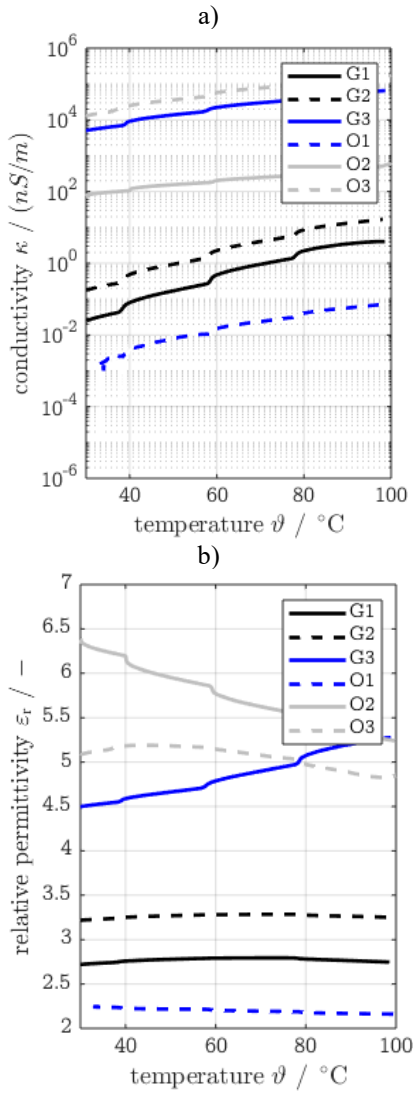

Figure 5: Measurements of a) conductivity of grease and oil at 20 Hz and of the relative permittivity at 100 kHz from 30 °C to 100 °C , at 1 bar in a cylinder capacitor

A cylinder capacitor called EPSILON+ was used to determine the specific conductivity and relative permittivity of all lubricants as a function of the lubricant temperature. The results for the conductivity are shown in Figure 5 a) and for the permittivity in Figure 5 b). It is expected that the conductive lubricants G2, G3 and O3 should have the highest specific conductivities. However, the capacitor measurements show that O3 has the highest conductivity among the six lubricants. G2 shows a relatively low conductivity near to the result of G1, although copper particles have been mixed in G2. This can be explained by the fact that additives and particles dissolved in the grease only lead to a conductivity of the grease at small distance between the electrodes, as they occur in rolling contact, for example. In the cylinder condenser (distance 1 mm), these additives are encapsulated by the insulating base oil. For determining the electrical properties of rolling bearing lubricants, the measurements on the cylinder capacitor can therefore only be used to a limited extent.

4.1. Results from phase 1 of the GESA investigations

Phase 1 of the investigations is required for the preconditioning of the lubricants and for the running-in of the bearings. This step homogenizes the grease, allowing the subsequent tests to be carried out with the rheological and electrical properties of the grease as constant as possible [25]. The run-in of the bearing causes smoothing on the bearing raceways and on the rolling element surfaces. This is necessary because otherwise roughness peaks may come into contact at an early stage and a stable lubricating film build-up is not possible. Therefore measurements of the bearing impedance and the bearing currents and voltages have a lower informative value before this phase. At this stage, the viscosity ratio κ is greater than 5 for all lubricants and tests.

Figure 6 a) and b) shows the impedance and phase angle measurements for system characterization. They are performed after preconditioning. The measurements are performed at a steady-state temperature of the bearings of approx. 40 °C, a speed of 1000 rpm and a load of 200 N. The system is characterized by a high degree of stability. A lower impedance of the conductive lubricants over a frequency spectrum can be expected compared to the insulating greases. The measured phase angle should remain at about 0° for the conductive greases over a frequency spectrum. It can be seen, that the impedance and phase angle are approximately the same for all investigated lubricants. As the frequency increases, the impedance decreases and the phase angle shifts in the direction of -90 °. The impedance measurement shows, that in this operating condition (bearing steady-state temperature) an insulating lubricating film separates the surfaces in the bearing for all investigated lubricants. This film can break through under an electrical charge.

Based on the impedance measurement, G1 is the best insulator. O3 should have the highest conductivity due to the low impedance values at low frequencies. Figure 5 a) shows that O3 has the highest conductivity. O1

and G1 are the lubricants that can insulate. G3 also has high conductivity, like O3. However, this cannot be detected by the impedance measurement. The copper particles from G2 have no significant influence on the bearing impedance. Probably the copper particles were pressed out of the raceway after the 16 h run. The bearing with G2 has a lower impedance than the bearing with G1. This can be an indication of the existing conductivity through copper particles.

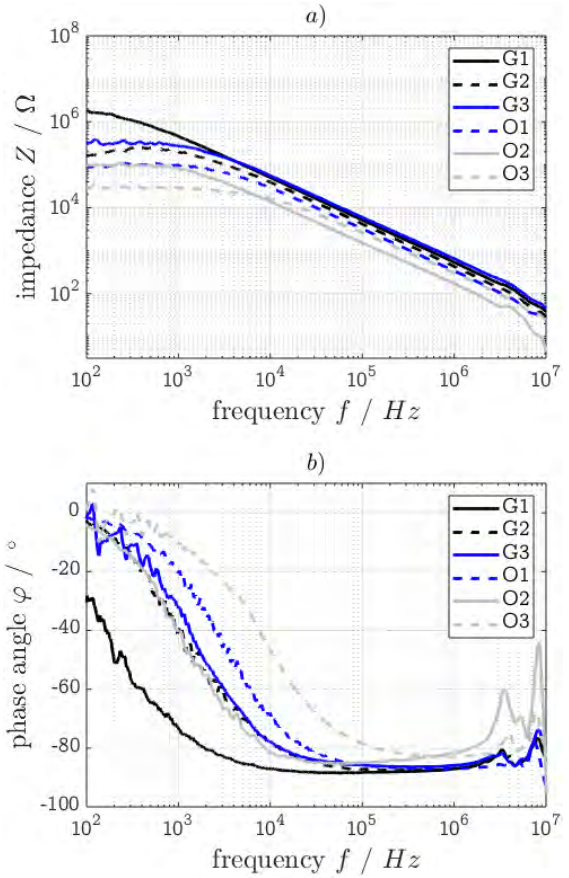

Figure 6: Measurements of a) bearing impedance and b) phase angle after 16 hours preconditioning at approx. 40 °C at a speed of 1000 rpm, a load of 200 N

4.2. Results from phase 2 of the GESA investigations

In phase 2 of the GESA investigations, a test voltage is applied to this system. The inverter switching frequency is 10 kHz. The further conditions can be found in Table 2. The aim of the investigation is to determine the breakdown voltage of the lubricating film for all lubricants. For this purpose, the test voltage is gradually increased (1 V - 10 V with 0.1 V steps; 10 V - 60 V with 5 V steps). For the examined lubricants, a voltage range can be determined in which EDM-currents occur. Figure 7 shows the results from phase 2 of the investigation. For all lubricants, there is a complete build-up of voltage over the lubricating film in the low voltage range. EDM-currents also occur with all lubricants. The conductive lubricants G3 and O2 show improvements with regard to their electrical behaviour in the bearing. When the voltage is increased, no voltage is built up above the lubricating gap in any of the six lubricants tested. In this case ohmic currents flow. This effect already occurs with conductive lubricants G3 and O2 at lower voltages compared to G1, G2 and O3. G3 behaves best with regard to the electrical behaviour in the bearing. A complete voltage build-up is only possible up to approx. 12 V. EDM-currents of up to about 25 V then occur.

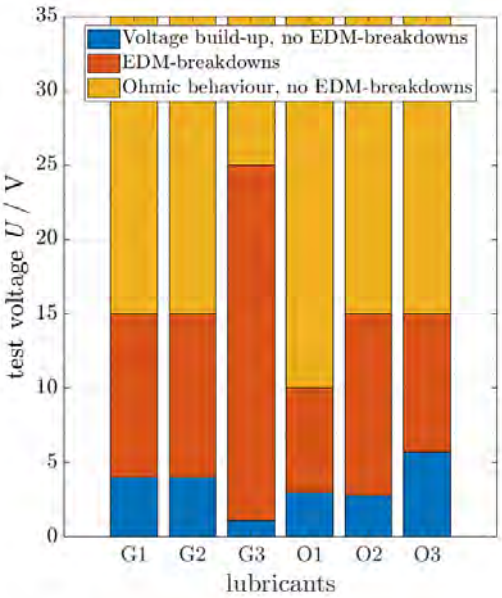

Figure 7: Results from phase 2 of the GESA tests. Measurements of EDM-voltage at voltage variation (1 - 60 V). Determination of electrical-tribological limits at approx. 40 °C at a speed of 1000 rpm, a load of 200 N and an inverter switching frequency of 10 kHz.

4.3. Results from phase 3 and 4 of the GESA investigations

In phase 2, the voltage build-up over the lubricating film was investigated as a function of the applied voltage level. In phases 3 and 4, the voltage build-up in the bearing as a function of the bearing temperature is examined more closely. The bearing is first cooled down to approx. 10 °C for this purpose. After reaching temperature of 10 °C, the operating conditions specified in Table 2 are set on the GESA. Increasing the bearing temperature results in a reduction of the base oil viscosity and thus also in a reduction of the lubricating film thickness. The investigations are completed after reaching 100 °C bearing temperature. During the increase in bearing temperature, bearing voltage and bearing current are measured in regular temperature steps (every 0.5 K). After evaluation of the recorded data, the temperature range in which EDM-currents occur can be specified. The ranges in which a complete voltage build-up is possible or ohmic currents flow are also defined. When EDM-currents occur, the number of detected currents per second and the level of the flowing EDM-current and the EDM-voltage are determined. The results from phase 2 have shown that the level of the applied bearing voltage has an influence on whether EDM-currents or ohmic-currents flow. Therefore, the investigations presented in this chapter are performed at both a low applied test voltage of 5 V (phase 3) and a higher applied test voltage of 20 V (phase 4). Figure 8 a) shows the average number of measured EDMs as a function of bearing temperature

at an applied test voltage of 5 V and 20 V (see Figure 8 b)).

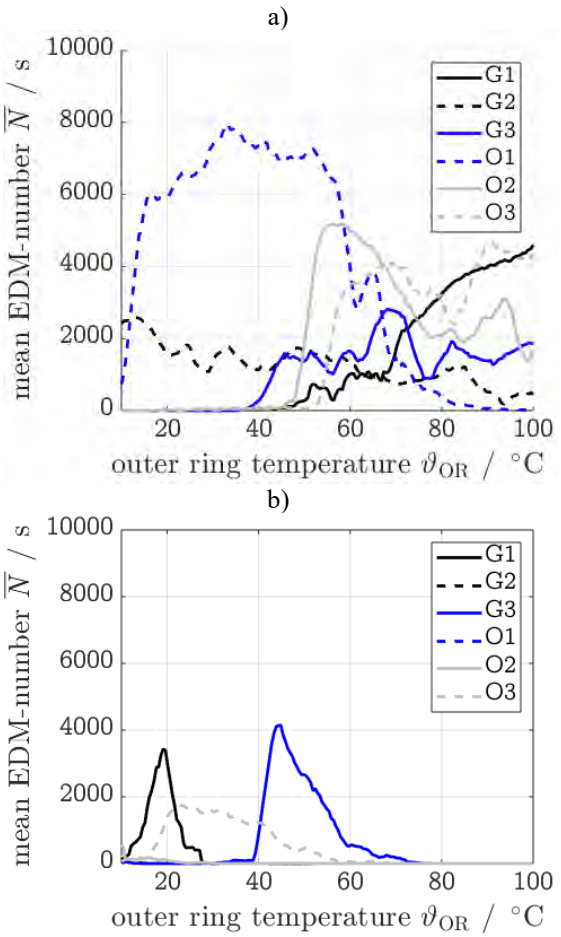

Figure 8: Results of phase 3 and 4 of the GESA investigations on the average EDM number per second as a function of bearing temperature (10 °C – 100 °C) at a speed of 1000 rpm, a load of 200 N and an inverter switching frequency of 10 kHz a) Results for an applied test voltage of 5 V b) Results for an applied voltage of 20 V.

It can be clearly seen that at an applied test voltage of 5 V, the temperature range in which EDM-breakdowns occur is very large for all investigated lubricants. In the case of greases G1, G2, G3 and oils O1, O2, O3 EDM-breakdowns can be observed. This means that EDM-breakdowns can also occur with conductive lubricants. The temperature range, in which EDM-breakdowns take place, is wide.

At an applied test voltage of 20 V (Figure 8 b) there are differences to Figure 8 a). EDM-breakdowns increasingly occur for lubricants G1, G3 and O3 at lower bearing temperatures, where the lubricating film thickness is higher. Low number of EDM-breakdowns can be observed for G2, O1 and O2 at temperature about 10 °C.

The temperature range of the EDM-discharge currents is significantly lower. As the temperature rises, ohmic currents predominantly occur. With the conductive lubricants G2 and O2, EDM-discharge currents could only be detected sporadically at low bearing temperatures about 10 °C. With grease and oil only few voltage builds up across the lubricating film and EDM-breakdowns can be observed. Predominantly ohmic currents are detected.

In addition to the temperature ranges in which bearing currents occur, the frequency distribution of the EDM-currents and voltages are also helpful for further assessment. Figure 9 and Figure 10 therefore shows the maximum, minimum and mean EDM-voltages occurring at an applied test voltage of 5 V and 20 V for all investigated lubricants. The values are resulted as a mean value from all current and voltage measurements of phases 3 and 4. In addition, the frequency distribution of the average EDM-voltages is shown in Figure 11 and Figure 12. Figure 11 shows the frequency distribution at an applied voltage of 5 V and Figure 12 shows the frequency distribution at an applied voltage of 20 V for all investigated lubricants.

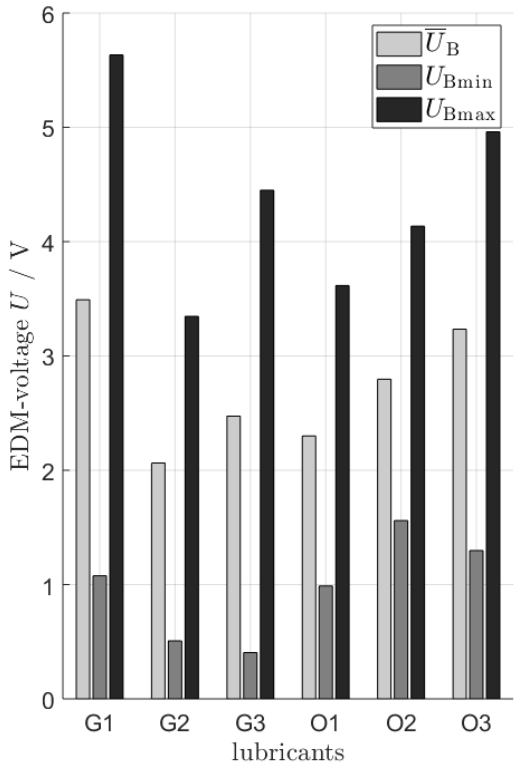

Figure 9: Average values of the EDM-voltage averaged over all 900 measured values at GESA in phase 3 on the axial grooved ball bearing 51208 at an axial load of 200 N, speed of 1000 rpm, temperature variation from 10 °C to 100 °C, measurement of voltage after temperature change in 0.5 K steps, with applied voltage of 5 V and switching frequency of 10 kHz.

When considering the results from phase 3 of the GESA investigation (applied test voltage 5 V), differences between the conductive greases and the insulating greases can be seen. The mean EDM-voltages for all greases are just over 2 V. Depending on the conductivity, the mean, maximum and minimum EDM-breakdown voltage for conductive lubricants is lower.

Based on the frequency distributions of the voltages occurring in phase 3 (Figure 11), there are no large deviations between conductive and insolating lubricants. EDM-breakdowns can occur with all lubricants, independent of their insulating or conductive properties.

The results from phase 4 of the tests (applied test voltage 20 V) clearly show the influence of the conductive lubricant with cooper particles on the occurrence of EDM-breakdowns. The mean and the maximum EDM-voltage measured for the greases G2 are significantly lower than for the other lubricants (Figure 10). Clear differences can also be seen between the frequency distribution of the measured mean EDM-voltage at 5 V (Figure 11) and at 20 V (Figure 12).

Conclusions from phase 3 and 4 of the investigation:

- The breakdown voltage, measured at the bearing, fluctuates strongly. This can be explained by the dynamics of the rotating bearing.
- In the case of insulating and conductive lubricants, EDM-breakdowns may occur. In the case of conductive lubricants, the breakdown occurs at a lower voltage.
- The influence of conductive lubricants at a low applied test voltage (5 V) is low. The mean and maximum EDM-voltage of conductive lubricants is lower compared to insulating lubricants, but the differences are low.
- The influence of conductive lubricants at a high applied test voltage (20 V) are clearly recognizable. Voltage build-up in the bearing is predominantly prevented, thus ohmic currents flow.

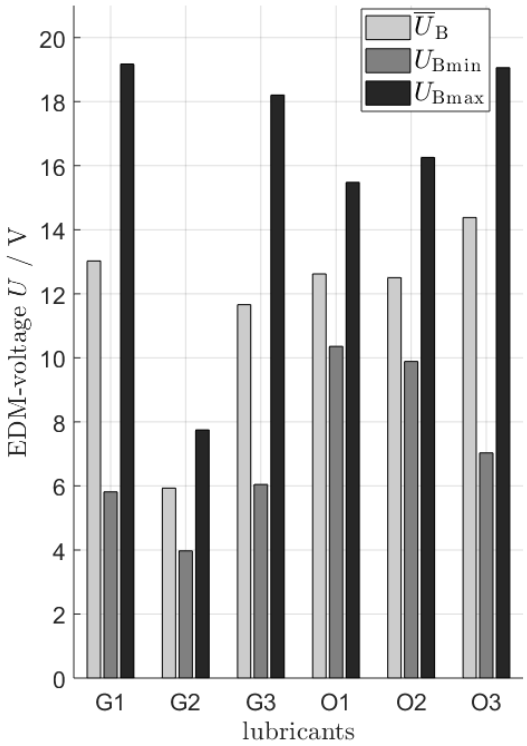

Figure 10: Average values of the EDM-voltage averaged over all 900 measured values at GESA in phase 3 on the axial grooved ball bearing 51208 at an axial load of 200 N, speed of 1000 rpm, temperature variation from 10 °C to 100 °C, measurement of voltage with temperature change in 0.5 K steps, with applied voltage of 20 V and switching frequency of 10 kHz.

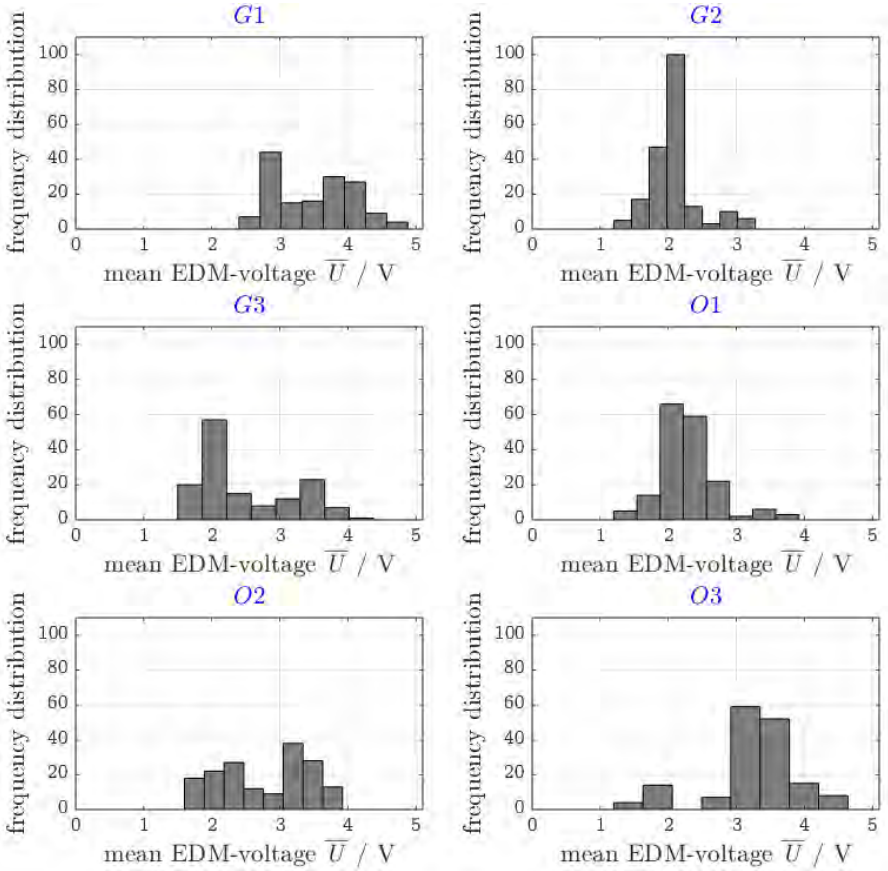

Figure 11: Results of phase 3 of the GESA test at constant speed of 1000 rpm, load of 200 N and inverter switching frequency of 10 kHz. Frequency distribution of the average EDM-voltage at applied voltage of 5 V

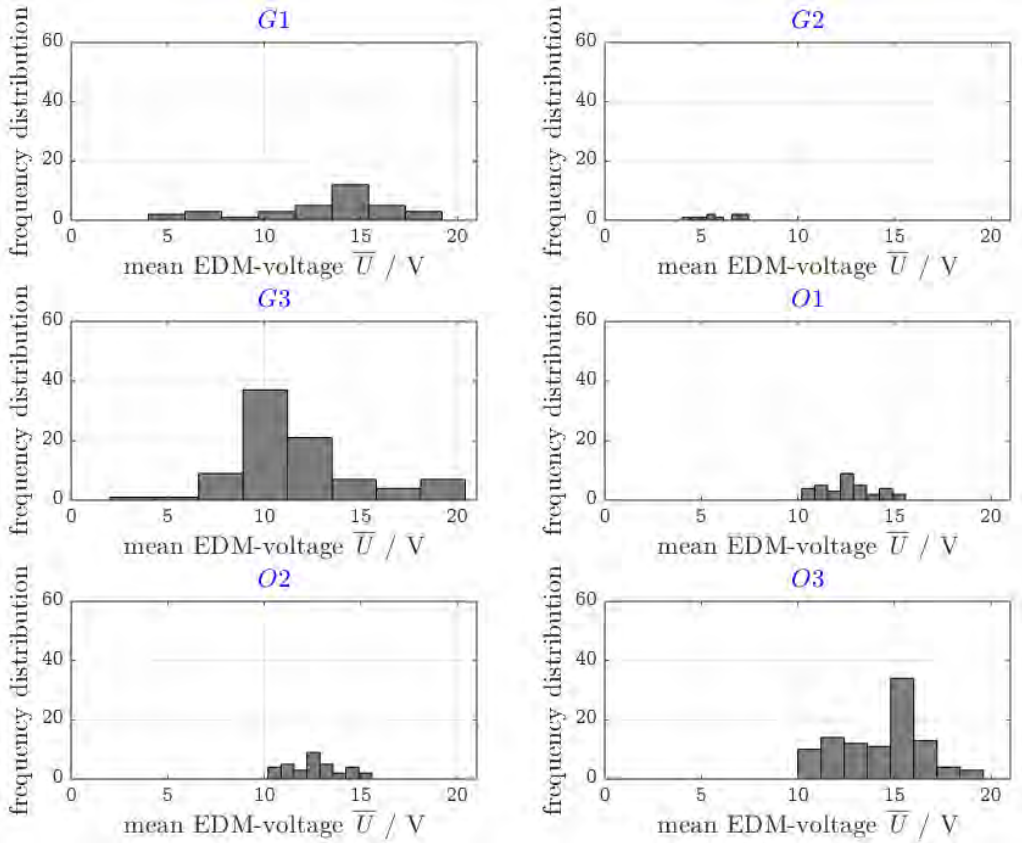

Figure 12: Results of phase 3 of the GESA test at constant speed of 1000 rpm, load of 200 N and inverter switching frequency of 10 kHz. Frequency distribution of the average EDM-voltage at applied voltage of 20 V

5. Conclusions

In the context of this article, results from investigations of conductive and insulating lubricants in rolling contact under test voltage application were examined. The focus was on the occurrence of EDM-currents and the electrical conditions in the rolling bearing. The axial bearing test rig "GESA" developed at the MEGT was used for this purpose. The tests on a cylindrical capacitor to determine the specific conductivity of the greases can only be used to a limited extent, as the distance between the capacitor electrodes is greater than the lubricating film thickness in rolling bearing contacts. When measuring the bearing impedance at bearing steady-state temperature, no significant differences between the conductive and insulating lubricants are discernible. If conductive lubricants are used, a lower bearing impedance can be measured. When applying voltage to the bearing, it was shown that with a lower test voltage at the bearing a complete voltage build-up across the lubricating film is possible for all tested greases and oils. EDM-currents can also be detected for all greases and oils. As the applied test voltage increases, clear differences in the electrical behaviour of the conductive greases compared to the other greases can be detected. Tests with an applied test voltage of 20 V show that the conductive greases already prevent a build-up of voltage at higher lubricating films in the case of higher and lower bearing temperatures. Mostly ohmic currents flow, which are comparable to currents occurring in mixed friction operation conditions.

The results, presented in this paper, show that the use of conductive lubricants has an influence on the electrical conditions in the rolling contact.

It must also be examined which electric effects have influence regarding the bearing damages presented in the introduction. For this purpose, it is recommended to carry out long-term tests with conductive grease in the rolling contact. This also allows to investigate the long-term effect of the conductivity.

In the context of this paper, a method for the investigation and comparison of the EDM-breakdown voltage of lubricants for rolling bearings was presented. The method can be used to investigate insulating and conductive greases and oils. The lubricants were tested on thrust ball bearing 51208 under test conditions close to the conditions of electrical motors and gears. EDM-breakdowns were generated in the bearing by the application of test voltage. After automated detection of these EDM-breakdowns, the breakdown voltage was analysed and compared. With the developed method greases and oils were investigated and evaluated.

Acknowledgment

The authors gratefully acknowledge financial support from FVA e.V. and AiF with IGF-Project Nr. 19161 N/2.

References

[1] G. Preisinger: Cause and effect of bearing currents in frequency converter drive electrical motors – investigation of electrical properties of rolling bearings, PhD thesis, TU Wien, (2002).

[2] A. Muetze: Bearing Currents in Inverter-Fed AC Motors, PhD thesis, TU Darmstadt, (2004).

[3] A. Romanenko: Study of inverter-induced bearing damage monitoring in variable-speed-driven motor systems, PhD thesis, Lappeenranta University of Technology, (2017).

[4] T. Zika: Electric discharge damaging in lubricated rolling contact, PhD thesis, TU Wien, (2010).

[5] H. Tischmacher, S. Gattermann: Einflussgrößen auf Lagerströme bei umrichtergespeisten Elektromotoren, VDI-Berichte 2202, (2013), p. 45-59.

[6] H. Tischmacher: Systemanalysen zur elektrischen Belastung von Wälzlagern bei umrichtergespeisten Elektromotoren, Dissertation, Universität Hannover, (2017).

[7] B. Radnai, Y. Gemeinder, B. Sauer, A. Binder: Schädlicher Stromdurchgang, Untersuchung des Schädigungsmechanismus und der zulässigen Lagerstrombelastung von (isolierten) Wälzlagern in E-Motoren und Generatoren verursacht durch parasitäre hochfrequente Lagerströme, Forschungsvorhaben Nr. 650 I, Heft 1127, (2015).

[8] B. Radnai: Wirkmechanismen bei spannungsbeaufschlagten Wälzlagern, PhD thesis, TU Kaiserslautern, (2016).

[9] D. Bechev, T. Kiekbusch, B. Radnai, B. Sauer: Untersuchung der Auswirkungen von leitenden und nichtleitenden Schmierfetten auf die Oberflächeneigenschaften bei spannungsbeaufschlagten Wälzlagern, GfT-Tagung, Göttingen, (2017).

[10] D. Bechev, A. Gonda, R. Capan, B. Sauer: Untersuchung der Oberflächenmutationen und der Riffelbildung bei spannungsbeaufschlagten Wälzlagern, 13. VDI-Fachtagung – Gleit- und Wälzlagerungen, (2019).

[11] DIN EN 60247: Isolierflüssigkeiten – Messung der Permittivitätszahl, des dielektrischen Verlustfaktors (tan δ) und des spezifischen Gleichstrom-Widerstandes, Berlin: Beuth Verlag, (2005).

[12] DIN EN 60156: Isolierflüssigkeiten, Bestimmung der Durchschlagspannung bei Netzfrequenz, Berlin: Beuth Verlag, (1996).

[13] DIN 51412: Prüfung von Mineralölerzeugnissen – Bestimmung der elektrischen Leitfähigkeiten, Berlin: Beuth Verlag, (2013).

[14] M. Koch, M. Fischer, S. Tenbohlen: The breakdown voltage of insulation oil under the influences of humidity, acidity, particles and pressure (International Conference APTADM). Wroclaw, Poland, Sept, (2007), p. 26-28.

[15] A. Joshi, J. Blennow: Electrical characterization of bearing lubricants, Annual Report Conference on Electrical Insulation and dielectric phenomena, Chalmers University of Technology Gothenburg, Sweden, (2014).

[16] E. Taslak, O. Arikan, C. F. Kumru, O. Kalenderli: Analyses of the insulating characteristics of mineral oil at operating conditions, Electr Eng; 100:321-331, Yildiz Technical University, Istanbul, Turkey, (2018).

[17] A. Jagenbrein: Investigations of Bearing Failures due to Electric Current Passage, PhD thesis, TU Wien, (2005).

[18] R. A. El-Adly, G. M. Turky: Comparative study between prepared electrical grease and the imported one, Egyptian Journal of Petroleum 27, p. 209-213, Egypt, (2018).

[19] H. Stache, S. Petri: Vor Entladungsschäden schützen – Elektrisch leitfähiges Wälzlagerfett vermeidet Spannungsüberschlag, Der Konstrukteur – Sonderheft "Antreiben – Steuern – Bewegen", (2008), p. 106–107.

[20] K. D. Schuster: Kampf der Elektroerosion, in: Der Konstrukteur, Produkte und Anwendungen, Konstruktionselemente, (2017).

[21] D. Bechev, B. Sauer: Systematische Untersuchungen des Stromdurchgangs in Wälzlagern und der elektrischen Schmierstoffeigenschaften, GfT-Tagung, Göttingen, (2018).

[22] A. Joshi, J. Blennow: Investigation of the Static Breakdown Voltage of the Lubricating Film in a Mechanical Ball Bearing, Nordic Insulation Symposium - Nord-IS 13 - Trondheim, Norway, June 9 - 12, (2013).

[23] A. Beroual, U. Khaled, P. S. M. Noah, H. Sitorus: Comparative Study of Breakdown Voltage of Mineral, Synthetic and Natural Oils and Based Mineral Oil Mixtures under AC and DC Voltages, https://doi.org/10.3390/en10040511, Energies (2017), 10, 511.

[24] J. Foldyna, K. Chmelík, S. Mišák: Influence of electric discharges on bearings of electric machines, Advances in Electrical and Electronic Engineering, (2011).

[25] H. Baly: Reibung fettgeschmierter Wälzlager; Dissertation, Universität Hannover, (2005).